Master of Science Thesis

CFD analysis of piston cooling by use of oil spray

Achillefs Zampos

July 8, 2024

Faculty of Aerospace Engineering · Delft University of Technology

CFD analysis of piston cooling by use of oil spray

Master of Science Thesis

For obtaining the degree of Master of Science in Aerospace Engineering at Delft University of Technology

Achillefs Zampos

July 8, 2024

Faculty of Aerospace Engineering · Delft University of Technology

Delft University Of Technology
Department Of
Aerodynamics

The undersigned hereby certify that they have read and recommend to the Faculty of Aerospace Engineering for acceptance a thesis entitled **"CFD analysis of piston cooling by use of oil spray"** by **Achillefs Zampos** in partial fulfillment of the requirements for the degree of **Master of Science**.

Dated: July 8, 2024

Head of department: _____
Prof.dr.ir. S. Hickel

Supervisor: _____
Dr.ir. J. Znaien

Reader: _____
Prof.dr.ir. S.J. Hulshoff

Reader: _____
Prof.dr.ir. I. Langella

Abstract

Diesel engines find application in a large number of sectors of modern industries, such as the automotive and maritime. The wide adoption of Diesel engines, along with the rise of environmental concerns created the needs for optimization of fuel efficiency and power output as well as minimization of exhaust gas emissions. These targets must be met while retaining the reliability of Diesel engines. One technique that is used to significantly enhance the reliability of Diesel engines is piston cooling. The working fluid is engine oil which is injected in the cylinder towards the lower side of the piston. The objective of the current study is to simulate the process of cooling with the aid of CFD. The numerical methodologies that are used in the current study are the Reynolds-Averaged Navier-Stokes (RANS) equations for the continuous phase, while for the disperse phase the modelling is conducted with the Lagrangian modelling. The numerical model which is built focuses on the effect that the mesh resolution has on the results of the simulation, especially on the disperse phase of the flow. It can be inferred that there is dependence between the quality of the results and the mesh resolution. It is shown that the grid has to be fine enough to produce quality results, but if there is excessive refinement, the quality of results drops because assumptions of the Lagrangian modelling are not satisfied. Following this phase of the study, a CFD model is built to simulate the phenomenon of droplet impingement on a solid wall. In this set of simulations, the goal is to compare the impingement model that is used in the software with published experimental results of droplet impingement. The results indicate agreement between the CFD model and the experimental process. In the final stage of the thesis, there is the numerical study of heat transfer involved in the process of spray impingement on a hot wall. A CFD model is built to compare the heat transfer which is predicted by the software model and results from relevant published experimental studies. It can be concluded that there is divergence between CFD and published experimental results, stemming from the modelling assumptions of the software. The results of the present thesis can be used in future studies of the company, either as a continuation of the spray cooling topic, or for novel studies such as gallery cooling.

Acknowledgements

I would like to express my deepest gratitude to those who have supported and guided me throughout the completion of this master thesis.

First and foremost, I extend my heartfelt thanks to my academic advisor, Professor Hickel. Your invaluable guidance, insightful feedback, and constant encouragement have been instrumental in the development and completion of this thesis.

I am also grateful to my company supervisor, Dr. Jemil Znaien, at DAF. Your practical insights, professional support, and sharing of your expertise have been crucial in the completion of this thesis.

Lastly, I would like to thank my family. Your unwavering support, your endless love and encouragement have been the driving force behind this journey.

Delft, The Netherlands
July 8, 2024

Achillefs Zampos

Contents

List of Figures

List of Tables

Nomenclature

Latin Symbols

A	Characteristic surface area
A'	Surface area of fluid film
A_c	Coefficient for calculation of We_c in Bai-Gosman model
A_{cont}	Contact area of heat transfer
Bo	Bond Number
b_d	Particle heat penetration coefficient
b_w	Wall heat penetration coefficient
Ca	Capillary number
C_B	Basset force coefficient
C_D	Drag coefficient
C_{p_d}	Droplet specific heat
C_{p_w}	Wall specific heat
C_r	Courant number
C_S	Saffman lift coefficient
C_{vm}	Virtual mass coefficient
D	Particle diameter
D_0	Initial droplet diameter
D_c	Cylinder diameter
D_{eff}	Effective particle diameter
F_B	Basset force
f_b	Body force exerted on film

F_D	Particle drag force
F_d	Sum of forces exerted on a particle
F_P	Force from pressure field
F_S	Saffman lift force
F_τ	Shear stress force
F_{un}	Undisturbed flow field force
F_{vm}	Virtual mass force
g	Gravitational acceleration
H_c	Cylinder height
h_f	Thickness of fluid film
H_f	Total enthalpy of fluid film
K	Non dimensional parameter for droplet impact energy
k	Turbulent kinetic energy
L	Flow characteristic length
La	Laplace number
m_d	Particle mass
$\dot{m}$	Mass flow rate of oil
N	Number of cells
Oh	Ohnesorge number
P	Pressure
Q''	Volumetric spray flux
$\dot{Q}_{wp}$	Droplet-wall heat transfer
R_a	Surface roughness
Re	Reynolds number
S_E	Source or sink of energy per unit area
S_{ij}	Shear rate tensor
S_m	Source or sink of momentum per unit area
St	Stokes Number
S_u	Source or sink of mass per unit area
T_{boil}	Boiling point of liquid
T_{drop}	Droplet temperature
T_f	Viscous stress tensor of fluid film
T_{Leid}	Leidenfrost temperature
T_w	Wall temperature
T^*	Dimensionless wall temperature
U	Freestream velocity magnitude
u	x component of velocity vector
$\underline{u}$	Velocity vector

$\underline{u}'$	Fluctuating part of velocity vector
$\langle \underline{u} \rangle$	Ensemble average part of velocity vector
u_e	Particle velocity
u_s	Particle slip velocity
V_d	Droplet volume
V_i	Incident velocity
V_P	Particle velocity
V'	Volume of fluid film
v	y component of velocity vector
v_f	Velocity of fluid film
w	z component of velocity vector
We_c	Critical Weber number for transition to splashing
We_i	Incident Weber number

Greek Symbols

α_c	Volume Fraction of continuous phase
α_d	Volume Fraction of dispersed phase
ΔT_{wd}	Temperature difference between wall and droplets
Δt	Time step
ΔV	Total volume of both phases
ΔV_c	Volume of continuous phase
ΔV_d	Volume of dispersed phase
Δx	Grid size
δ	Wall film thickness
δ_{32}	Sauter Mean Diameter
δ_{ij}	Kronecker delta
θ_i	Angle of collision
κ_d	Thermal conductivity of droplet
κ_w	Thermal conductivity of wall
μ_c	Dynamic viscosity of continuous phase
ν_c	Kinematic viscosity of continuous phase
ν_T	Eddy viscosity
ρ_c	Density of continuous phase
ρ_d	Density of dispersed phase
ρ_f	Density of fluid film liquid
σ	Surface tension
τ_F	Characteristic time of flow field

τ_{ik}	Shear stress tensor
τ_V	Particle momentum response time
ω	Curl of the velocity field

Abbreviations

CFD	Computational Fluid Dynamics
DEM	Discrete Element Method
LES	Large Eddy Simulation
PDF	Probability distribution function
RANS	Reynolds Averaged Navier-Stokes
SMD	Sauter Mean Diameter
TDC	Top dead center

Chapter 1

Introduction

Diesel engines play an important role in the automotive industry, for maritime propulsion, and for electricity generation. Since the first concept of Diesel engine in 1893 by Rudolph Diesel, there has been ample research and effort into the analysis and improvement of this type of engine [33, 56]. There are three major goals in the development of Diesel engines: The increase of fuel efficiency, the reduction of undesired emissions in terms of noise and exhaust gases, and the optimization of performance in terms of power output.

A large number of environmental concerns has led to rather strict emission regulations that the automotive industry has to abide by. One way to increase the efficiency of a Diesel motor is to cool the pistons with engine oil. Apart from the benefit of increased efficiency when there is a piston cooling system, there is the issue of reliability of the engine. It has been supported by Thiel [52] and Izadi [22] that the solution of piston cooling decreases the thermal loads of the moving parts of the engine, thus being beneficial in this way to the reliability of the motor.

As it can be understood, the aforementioned benefits led DAF to investigate into the topic of piston cooling. In a series of studies of this process, there have been attempts to explain the complicated physical phenomena that govern. Through Computational Fluid Dynamics (CFD) simulations. An experimental approach would increase significantly the cost of the study. Furthermore, another possible limitation of the experimental procedure related to this topic is the lack of versatility. It is understandable that a greater number of configurations can be tested in CFD software rather than experimental ones. At the same time, another benefit of CFD over an experimental study of this type is that while using CFD, there exist measurements on all of the domain of the simulation. On the other hand, while conducting an experimental campaign, one would have to be limited to a specific amount of data that could be collected locally.

1.1 Problem description

The problem of piston cooling is a rather wide topic that can be divided into smaller sub-problems. In the current configuration of the pistons, the oil cooling is done primarily by

the use of a cooling gallery. The visualization of the cooling gallery is on the following figure.

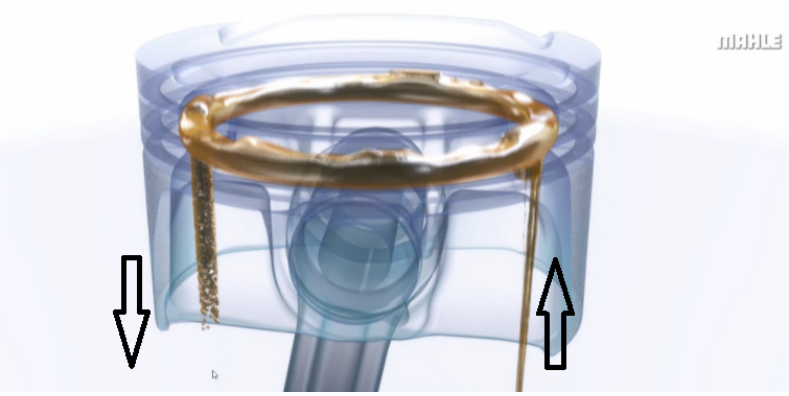

Figure 1.1: Piston gallery configuration, reprinted from [27]

As it can be seen, a jet of oil is injected from the bottom of the crankcase facing upwards. The jet is pointed towards the entrance of the gallery. After crossing the toroidal volume of the gallery, the oil exits from a second hole. The engine oil inside the gallery performs a sloshing motion, due to the reciprocation of the piston. It should be mentioned that it is not possible to have all of the jet pass through the gallery, since the phenomenon of jet break-up can occur. Thus, a portion of the jet's liquid impinges on the wall. Through the impingement on the wall, there is the phenomenon of cooling the undercrown of the piston. Jet break-up is a phenomenon of great interest on the topic of piston cooling. It dictates whether the jet will reach the piston in a continuous form or it will disintegrate into droplets and ligaments. As it can be seen on Figure 1.2, the evolution of the jet and the jet impingement cooling sub-problems have been previously investigated at DAF. On the other hand, the sub-problem of gallery cooling is still a topic to be studied. In this study, the scope includes the spray impingement cooling part of the general piston cooling problem.

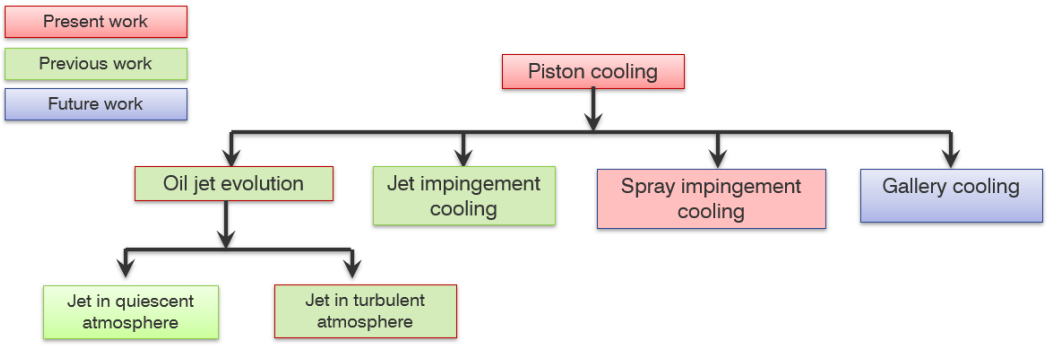

Figure 1.2: Categorization of piston cooling sub-problems

1.2 Previous work

Prior to the current study, two other theses were conducted on the general topic of piston cooling at DAF. The first of those studies was conducted by Celik [12] while the second study was conducted by Venkatesh [54].

Celik conducted simulations of an oil jet by using a multiphase LES configuration. The multiphase modelling was an Euler-Euler approach, more specifically the Volume of Fluid scheme (VOF) scheme, which proved to be stable. The purpose of those simulations were to measure numerically the flow rate efficiency of the jet. By flow rate efficiency, it is meant the ratio of the engine oil that passes through the cooling gallery, over the total amount of engine oil that is injected. A visualization of the described set-up is provided for clarification.

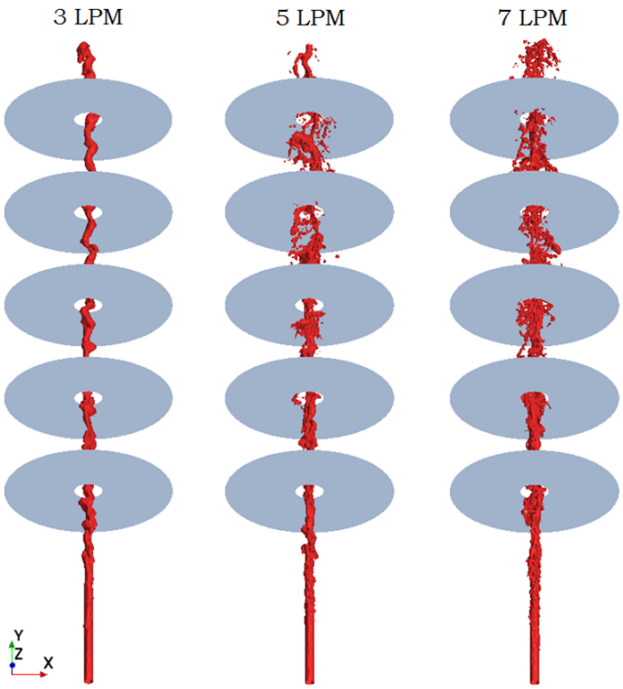

Figure 1.3: Flow rate efficiency simulations, reprinted from [12]

Furthermore, Celic conducted a series of simulations that dealt with the topic of jet impingement heat transfer. More specifically, 2D RANS models were built for this reason, while the results were compared to published analytical solutions and experimental data.

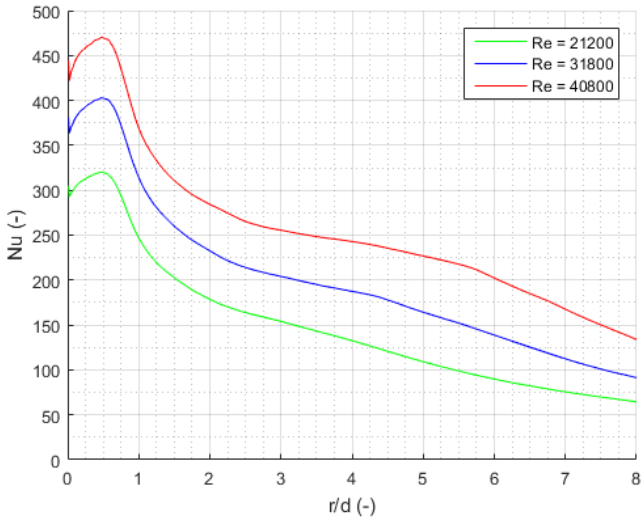

Figure 1.4: Nusselt number results at different Re, reprinted from [12]

The second thesis on the topic of piston cooling was done by Venkatesh [54]. The main topic of investigation in Venkatesh's study was the development and the disintegration of the oil jet. It was found that the most important factor that leads to primary breakup is the wall turbulence. Moreover, there was investigation of the effect of the ambient air's turbulence on the disintegration of the jet. The conclusion was that the ambient air's turbulence was not a dominant factor as far as the primary breakup is concerned. However, it was shown that the secondary breakup was affected by the turbulence of the air inside the crankcase.

One of the most important findings of Venkatesh was related to the distribution of the droplet size. Through LES simulations, the distribution of droplet sizes was found for various volumetric flow rates of oil. This is a rather important finding for the current thesis, since these distributions of droplet sizes are used as an input for the simulations of spray impingement. An example of the probability distribution function of droplet diameter that was found at TDC of the piston by Venkatesh can be seen in Figure 1.5.

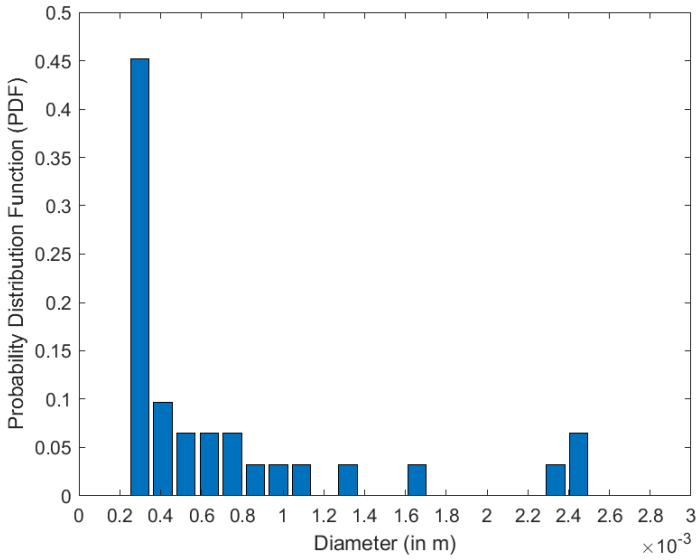

Figure 1.5: Droplet size PDF, reprinted from [54]

1.3 Research questions

This study's main concern was to answer the following research questions.

Question 1: What are the key requirements for the creation of a solid CFD RANS model including Lagrangian multiphase flow?

- Identify what is the suitable size of the grid and timestep for a stable and accurate solution.
- How is the solution affected when the mesh is refined in an excessive manner?

Question 2: Which are the dominant parameters affecting the phenomenon of droplet wall impingement?

- Identify what are the different impingement outcomes when a droplet impacts a solid wall.
- What is the outcome of droplet impingement in the specific conditions of a DAF engine?
- How is impingement modelled in the used CFD software?
- Build and validate the numerical impingement model, based on experimental data found on the literature.

Question 3: What are the key parameters affecting the heat transfer involved in droplet impingement?

- How is impingement heat transfer modelled in the used CFD software?
- Construct a CFD model that includes the calculation of heat transfer.
- Literature research on similar cases and validation of the CFD model through published experimental results.

1.4 Structure of report

Chapter 2 of the report is a literature review. In this chapter, the fundamental concepts of multiphase flows are established, along with the presentation of papers that were found to be relevant to the topic of the current study. In the subsequent chapter, there is the presentation of the simulations that were conducted aiming to investigate the sensitivity of the grid when there is Lagrangian multiphase flow modelling and the behaviour of droplets in the absence of a solid wall. Following is chapter 4, where there is the validation of the numerical model that was built to simulate the droplet impingement. In chapter 5, there is the presentation of the simulations that are conducted with aim to confirm that the correct mass flow rate of oil is introduced in the engine cylinder. The topic of impingement heat transfer is studied in chapter 6, where there is the presentation of the model that is used in the software, as well as the comparison of the numerical results with the experimental results of a relevant paper. In chapter 7 there are the conclusions of the thesis and finally in chapter 8 there are suggestions on how the current thesis can be improved and developed by a future student.

Chapter 2

Literature Review

2.1 Fundamental concepts of Multiphase Flows

Multiphase flows are flows where two or more phases coexist and interact with each other inside a flow field. In the subsequent study two phases of fluid are going to be taken into account. The first phase is air that is assumed to be ideal gas. It is going to be called the continuous phase. The liquid phase of the study is engine oil, which in the present study is also encountered as the dispersed phase.

One of the most important parameters regarding multiphase flows is the volume fraction. For the continuous phase the volume fraction is defined as [16]:

$$\alpha_c = \lim_{\Delta V \to \Delta V_{mo}} \frac{\Delta V_c}{\Delta V} \, , \tag{2.1}$$

where ΔV_{mo} is the point volume of the mixture, which is essentially a critical volume under which there may be microscopic effects that compromise the assumption of continuum.

Similarly, there is the definition of volume fraction of the dispersed phase, or the oil:

$$\alpha_d = \lim_{\Delta V \to \Delta V_{mo}} \frac{\Delta V_d}{\Delta V}. \tag{2.2}$$

From the conservation of mass it is deduced that: $\alpha_c + \alpha_d = 1$.

2.2 Dimensionless numbers

As a first investigation of the phenomenon of the impingement, it is useful to recognise the important parameters that govern the physics of this problem.

1. **Weber number**:

$$We_i = \frac{\rho_d V_i^2 D}{\sigma} \tag{2.3}$$

where V_i is the incident velocity, which is the normal part of the relative velocity of the droplet with the wall.

It is the dimensionless number expressing the ratio of the aerodynamic forces related to the dynamic pressure over forces of surface tension, as it is described by Sirignano in [47]. It can be considered as one important parameter in impingement [6], as it is frequently used to describe the conditions during the impact and it plays a pivotal role in the construction of impingement models. As an outline, when the Weber number is low, ($\mathcal{O}(1)$) then the droplet tends to retain its shape even after collision, since the surface tension forces are not negligible. On the contrary, when the Weber number is high ($We \gg 1$), then the inertia dictates the outcome of the impingement, which is splashing. In splashing, the droplet disintegrates into smaller droplets after the impact as it is discussed on paragraph 2.3.

2. **Laplace number**:

$$La = \frac{\sigma \rho_d D}{\mu_d^2} \tag{2.4}$$

The Laplace number is used to express the ratio of the surface tension forces over the viscous forces. It can be expressed alternatively as a function of Weber and Reynolds numbers:

$$La = \frac{Re^2}{We_i}$$

In essence, both Laplace and Ohnesorge numbers express the importance of viscous forces related to the surface tension forces, nevertheless they do so from different standpoints. The relation between La and Oh is:

$$La = \frac{1}{Oh^2}$$

The main manifestation of the Laplace number can be seen on the limit of splashing. For example, on the Bai-Gosman model, it is shown in [43] that as the Laplace number gets larger, the droplet transitions to splash on lower Weber numbers.

3. **Temperature ratios**: Different temperatures of a wall impingement system play a significant role on the physics of the collision. Important temperature ratios that affect the physics are the following:

$$\frac{T_w}{T_{boil}} \, , \, \frac{T_w}{T_{Leid}} \, , \, \frac{T_{drop}}{T_w} \, ,$$

where: T_w is the temperature of the wall, T_{boil} is the boiling point of the liquid, T_{drop} is the temperature of the droplet and T_{Leid} is the Leidenfrost point of the fluid. The Leidenfrost point is a characteristic point on the boiling curve (Figure 2.1). At this point, the heat flux from the hot wall towards the boiling liquid reaches a local minimum, as it progresses from transition boiling to film boiling. Heat flux is minimized due to the insulation of the vapour film that exists between the wall and the boiling liquid.

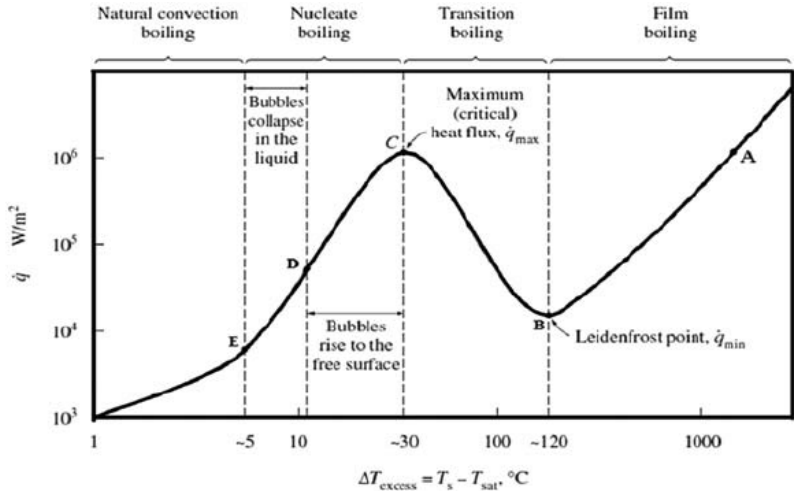

Figure 2.1: Typical boiling curve, reprinted from [1]

The manifestation of the first two temperature ratios can be seen at Figure 2.9. The outcome of the droplet impingement for the Bai-Gosman model is divided into three temperature ranges based on if the wall temperature is higher or lower than the boiling point and the Leidenfrost point.

4. **Wall film thickness ratio** $\frac{\delta}{D}$: It has been shown by a number of studies [29], [34] that the outcome of the impingement is affected significantly if the fluid film is shallow or if the fluid film is considered a deep pool compared to the droplet diameter. It is shown in [29], that the non dimensional wall film ratio changes the limits between coalescence and splashing regions.

5. **Dimensionless surface roughness** $\frac{R_a}{D}$: The effect of surface roughness is more prevalent when the wall that the droplet impinges is dry. It can alter the splashing characteristics as well the limit of the onset of the splashing region [6].

6. **Stokes Number**: Stokes number is the non-dimensional number indicative of the response time of a particle of the dispersed phase [16]:

$$St = \frac{\tau_V}{\tau_F} \tag{2.5}$$

where τ_V is the particle response time defined as:

$$\tau_V = \frac{\rho_d D^2}{18\mu_c}. \tag{2.6}$$

Physically, the particle response time represents the amount of time that is required for a non-moving particle to reach 63% of the undisturbed flow field's velocity, according to the methodology presented by Schwarzkopf et al. in [16].

On the other hand, τ_F is the characteristic time of the flow field. For a flow inside a cylinder of finite length, which is not fully developed, the characteristic time is:

$$\tau_F = \frac{L_c}{U}\ , \tag{2.7}$$

where L_c is a typical length scale and U is the velocity of the undisturbed flow field.

It can be observed that in the case of a very small Stokes number, i.e. $St \ll 1$, the particle responds very quickly to the changes that the flow field imposes. This means that the particle follows the streamlines of the flow and it behaves as if its inertia is negligible. The exact opposite happens when the Stokes number is much larger than 1, in which case the inertia of the particle dictates the path that it follows, almost independent of the flow streamlines.

2.3 Post impingement droplet behaviour

After discussing about the governing parameters of the single droplet impingement problem, it is useful to investigate the possible post-impingement behaviour of a single droplet. Bai and Gosman [6] identified that the impingement outcome could fall into 7 categories, which are mentioned on the following list. The criteria of this categorization are based on Weber number and the temperature of the wall, T_w.

1. **Stick**: When the droplet has very low kinetic energy compared to the surface tension, then the droplet sticks to the wall. This means that the droplet retains its shape after the collision and it does not suffer large deformations.

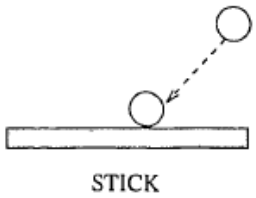

Figure 2.2: Droplet adhere regime, reprinted from [6]

2. **Bounce or rebound**: If the energy of the impact becomes larger than that of the stick regime, then during the collision a thin film of gas is trapped between the droplet and the liquid film [6]. However, the energy of the impact is not sufficient to rupture this gas film and the result is for the droplet to deform and bounce back. The latter description is valid for wetted walls (which is the set-up of interest). For dry walls, rebound occurs when wall temperature is very high (typically above the Leidenfrost point). Similarly to the wet walls, rebound occurs because the vapour film that is found between the wall and the droplet does not allow their contact.

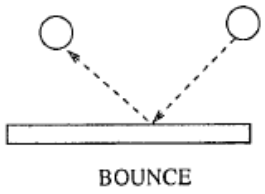

Figure 2.3: Droplet bounce regime, reprinted from [6]

3. **Spread**: When the kinetic energy of the impact is sufficient to rupture the gas film between the droplet and the liquid film, then the droplet deforms significantly and is deposited on the liquid film.

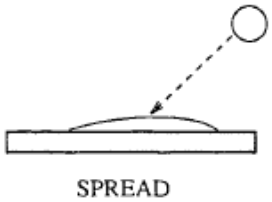

Figure 2.4: Droplet Spread regime, reprinted from [6]

4. **Break-up**: This regime of droplet impingement can be observed when the wall temperature is larger than the boiling point of the liquid but smaller than the Leidenfrost temperature. In this region, the droplet is deformed upon impingement and forms a liquid film similar to the process of Figure 2.4. Afterwards, the film disintegrates into a large number of small droplets (secondary atomization). The atomization occurs due to instabilities caused by the bubble boiling that takes place, as it is explained by Cossali et al. in [15]. More specifically, Cossali et al. [15] experimentally determined the following critical parameters:

Number	Value
We	116, 276, 514
Re	5100, 7880, 10755
La	2.27×10^5
Oh	2.11×10^{-3}

Table 2.1: Non-dimensional parameters on Cossali's experiment

It was found that for a droplet size range of $D = 1.8 - 4.6mm$, the Sauter Mean Diameter (SMD) of the droplets after impact was: $d_{32} = 0.03 - 0.05D$.

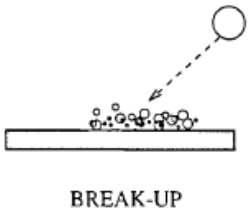

Figure 2.5: Break-up regime, reprinted from [6]

5. **Boiling-induced Break-up**:This regime is analogous to the Stick regime that was described previously. It is the regime where the Weber number is the lowest, thus the droplet impacts the wall retaining its shape. However, due to thermally induced instabilities, the droplet breaks up into smaller droplets.

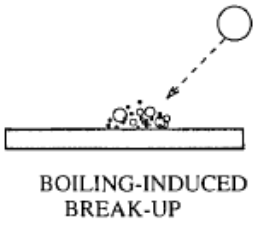

Figure 2.6: Boiling induced Break-up regime, reprinted from [6]

6. **Rebound with Break-up**: This regime occurs at wall temperatures close to the Leidenfrost limit. It is an impingement regime similar to that of the simple rebound. It is observed when the impact energy is higher than that of the rebound regime, so that the rebounding droplet becomes unstable and disintegrates into 2 or 3 smaller droplets, as it is explained by Wachters and Westerling in [55].

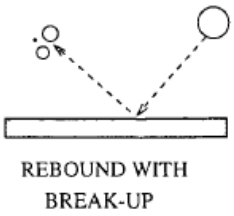

Figure 2.7: Droplet Rebound with Break-up regime, reprinted from [6]

7. **Splash**: Splash is the result of impingement when the collision energy is higher than all the 6 aforementioned states, regardless of wall temperature or wall state (dry or wetted). According to Rioboo et al. [34], splash is the breakup of a droplet, accompanied by the ejection of secondary droplets. During this process, the formation of crown may or may not be observed. It is a region where a number of studies have been conducted attempting to define criteria regarding its occurrence [6, 7, 34].

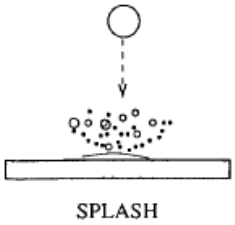

Figure 2.8: Droplet Splash regime, reprinted from [6]

2.4 Bai-Gosman model

The Bai-Gosman model was developed in 1997 and it is still being used in commercial software, such as Star CCM+. There are 6 possible outcomes for the impingement, as it can be seen on Figure 2.9.

On the x axis of the graph, there is the temperature of the wall T_w. We distinguish two limiting temperatures, called T_{boil} and T_{Leid}. These temperatures are the boiling point of the liquid and the Leidenfrost point of the liquid respectively. During the operation of the engine, the temperature of the wall (lower part of the piston) never exceeds the boiling temperature of the oil. Thus, it can be observed that we are going to operate on the left-most temperature range, or Temperature Range 1 as it is indicated on Figure 2.9.

The y axis represents the incident Weber number of the droplet. In the temperature range 1, the droplet impingement can have 4 possible results. Moving from lower to higher Weber numbers, the first possible outcome is for a droplet to adhere to the wall. This happens for We numbers lower than 2. For $2 < We \leq 20$, the model sets the droplet to rebound. For $20 < We \leq We_c$, the droplet spreads and merges with the existing fluid film of the wall. If the droplet surpasses the critical Weber number, then splash occurs. In the Bai-Gosman model, the critical Weber number does not have a fixed value, like the limits between adherence and rebound or rebound and spread, but it depends on the Laplace number of the droplet [6]. More specifically, the equation that is used to calculate We_c is:

$$We_c = A_c \cdot La^{-0.18} \tag{2.8}$$

The coefficient A_c depends on the state of the wall, meaning that there are different values of A_c between a dry and a wet wall. Moreover, there are different values of A_c for various non-dimensional surface roughness values. In the current study, the piston wall is wet, so no surface roughness is taken into consideration and the value of A_c is equal to 1320. This value of A_c occurred from the curve fitting of experimental data that were done with water droplets. This process that is described by Bai in [6] led to the criteria and the delimiters of the Bai-Gosman model. Later, this model was reviewed and the criteria changed in order to take into consideration the effect that the spray has on the outcome of the impingement, rather than investigating an isolated droplet. More specifically, for the initial Bai-Gosman model it can be seen on Figure 2.9 that the outcome of impingement

for a given temperature is defined by the Weber number of the droplet. On the subsequent review, called the Bai-Onera model, the impingement outcome depended on parameter K [43], a function of Weber and Ohnesorge number:

$$K = We\, Oh^{-0.4}\ . \tag{2.9}$$

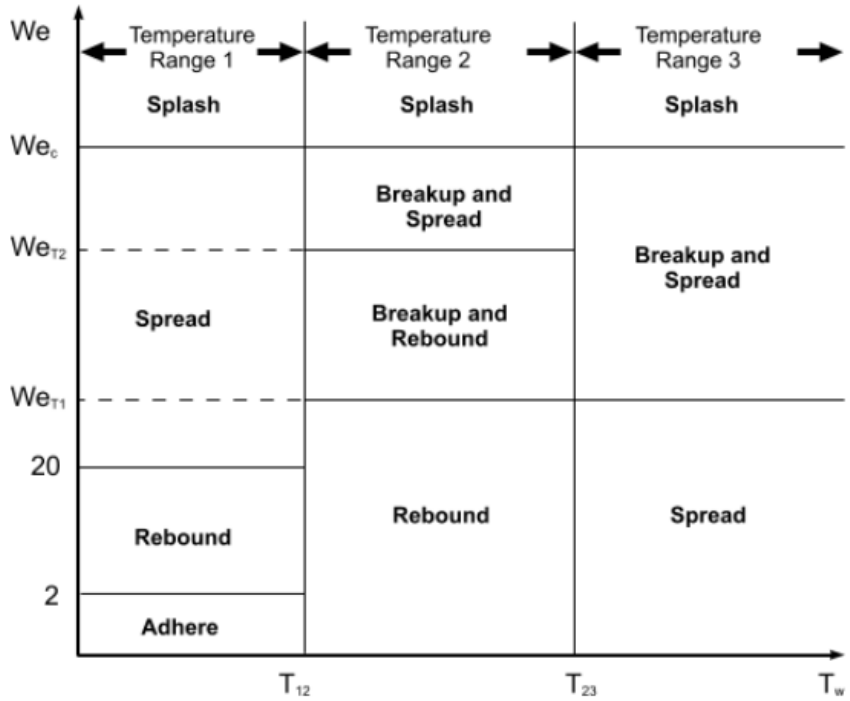

Figure 2.9: Possible outcomes of Bai-Gosman model for wet wall in Star CCM+, reprinted from [43]

2.5 Lagrangian Phase Modelling

In Star CCM+ software, the modelling of Lagrangian phase is done in accordance with the work of Crowe et al. [16]. More specifically, the motion of the particles inside the continuous phase follows the second law of Newton:

$$F_d = m\frac{du_d}{dt} \tag{2.10}$$

2.5.1 Force modelling

The total force that is exerted by the continuous phase on a particle is comprised of 6 different constituents:

1. **Undisturbed flow**: The first type of force that is exerted on a particle is the force that the undisturbed flow field would exert due to its pressure and shear stress fields.

Namely, the undisturbed force is formulated on [16] as:

$$F_{un} = F_P + F_\tau = V_i\big(- \frac{\partial P}{\partial x_i} + \frac{\partial \tau_{ik}}{\partial x_k}\big) \tag{2.11}$$

2. **Steady state drag**: The vast majority of the studies regarding the steady state drag have been conducted for particles of spherical shape. The force that is exerted on the particle can be found from the formula:

$$F_D = \frac{1}{2}\rho_c C_D A V_S^2 \tag{2.12}$$

In (2.12) the major concern is the calculation of the drag coefficient C_D. For creeping flow ($Re < 1$), the drag coefficient can be found by considering that the analytical solution for the force [3]:

$$C_D = \frac{24}{Re} \tag{2.13}$$

However, this model is restrictive in the sense that it is valid for very low Reynolds numbers. This is the reason why researchers have derived empirical relations in order to have an estimate of C_D for a wide range of Reynolds numbers. One such empirical relation that is also implemented in StarCCM+ is proposed by Schiller and Naumann [37]:

$$C_D = \frac{24}{Re}\Big(1 + 0.15Re^{0.687}\Big) \tag{2.14}$$

3. **Virtual mass**: As one particle moves inside a continuous phase, the flow field around it is distorted. In the wake of the particle, the continuous phase is following the motion of the particle. Thus, in the motion of the particle, we have to take into consideration that it "carries" some mass of the continuous phase. The force of this virtual mass is formulated as [16]:

$$F_{vm} = C_{vm}\frac{\rho_c V_d}{2}\Big(\frac{Du_i}{Dt} - \frac{dv_i}{dt}\Big)\,, \tag{2.15}$$

where: $C_{vm}$is the virtual mass coefficient in Star CCM+ is taken as equal to 0.5 for spherical particles [40], $\frac{Du_i}{Dt}$ is the acceleration of the fluid in the vicinity of the particle and $\frac{dv_i}{dt}$ is the acceleration of the particle.

Thus, from (2.15), it can be seen that the virtual mass force is linearly dependent on the relative acceleration of the adjacent fluid to the particle $\Big(\frac{Du_i}{Dt} - \frac{dv_i}{dt}\Big)$.

4. **Basset Force**: The Basset force bears some similarities to the virtual mass force, in the sense that they both refer to forces that are exerted on accelerating particles inside a continuum. The Basset force is the force that is exerted on the accelerating particle due to the changes of shear stress. The formulation of the Basset term is [16]:

$$F_B = C_B\frac{3}{2}D^2\sqrt{\pi\rho_c\mu_c}\Big[\int_0^t \frac{\frac{d}{dt'}(u_i - v_i)}{\sqrt{t - t'}}dt' + \frac{(u_i - v_i)_0}{\sqrt{t}}\Big] \tag{2.16}$$

The Basset force is not available to model in Star CCM+ when there is Lagrangian particle simulation.

5. **Saffman Lift**: This type of force is exerted on a particle when it is found on a non-uniform flow field like that of the following figure:

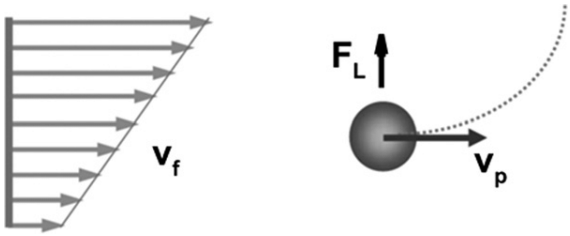

Figure 2.10: Saffman lift force

The differences in the relative velocity of the particle change the pressure field according to the Bernoulli principle. Thus, a lift force perpendicular to the velocity of the particle is going to be exerted on the particle with a resultant acceleration. The formula of the Saffman lift force that is used in Star CCM+ is [40]:

$$F_S = C_S \frac{\rho_c \pi}{8} D^3 (u_s \times \omega) \tag{2.17}$$

where: C_S is the Saffman lift coefficient. In Star CCM+, there are two options regarding the calculation of C_S [40]. The first option was proposed by Saffman [36] and the assumption that is made for this model is a very low Reynolds number ($Re \ll 1$). The second option regarding the shear lift coefficient was proposed by Sommerfeld [48]. This model is suitable for Reynolds numbers that are even larger than 40. $\mathbf{u_s}$ is the slip velocity of the particle is defined as: $\mathbf{u_s} = \mathbf{U} - \mathbf{V_P}$.

6. **Magnus Lift**: The Magnus lift is observed when a particle is rotating inside a flow field. Similarly with the Saffman lift, parts of the sphere that have higher relative velocity to the flow field are subjected to lower pressure and vice versa. As a result, there is a lift force that is applied to the particle. This type of force can be modelled only in conjunction with the DEM (Discrete Element Method) and not with the statistical Lagrangian modelling that is being used in this thesis.

2.5.2 Statistical Lagrangian modelling

During a simulation, it is common that a large number of particles are injected in the physical domain. This implies that theoretically, Newton's second law (equation 2.10) has to be solved for each particle. However, this cannot be the case for an industrial application. Solving every particle's equation of motion would greatly increase the cost of a simulation.

Instead of using the rather expensive method of solving (2.10) for every particle, another method can be implemented to reduce the cost and it is the statistical approach to the Lagrangian formulation. Computational particles, also known as parcels are used as a replacement of the physical particles [14, 51]. In essence, a parcel is a conglomerate of physical particles. The equation of motion and energy conservation is solved for each parcel instead of each physical particle. The benefit of this strategy is that by creating

conglomerates of particles, the number of equations to be solved can be significantly reduced. In the software that is used for the simulations, all of the parcels are comprised of identical physical particles. Thus, each physical particle has the same momentum and energy as with any other particle of the parcel. In this way, the complexity of the calculations is reduced.

2.6 Computational fluid dynamics

The equations that are used to describe a flow field are the Navier-Stokes equations. In essence, they describe the conservation of momentum, or Newton's second law on the context of fluids. There is abundant documentation on this set of equations, since they are the fundamental equations of fluid dynamics. They can be found for example on the textbooks of Anderson [4], Schlichting [38] and Batchelor [8]. In their 3-dimensional form, the unsteady Navier-Stokes equations are:

$$\begin{aligned}
\rho\frac{Du}{Dt} &= -\frac{\partial P}{\partial x} + \frac{\partial}{\partial x}\Big[\mu(2\frac{\partial u}{\partial x} - \frac{2}{3}div\mathbf{v})\Big] + \frac{\partial}{\partial y}\Big[\mu(\frac{\partial u}{\partial y} + \frac{\partial v}{\partial x})\Big] + \\
&\quad \frac{\partial}{\partial z}\Big[\mu(\frac{\partial w}{\partial x} + \frac{\partial u}{\partial z})\Big] + f_x \\
\rho\frac{Dv}{Dt} &= -\frac{\partial P}{\partial y} + \frac{\partial}{\partial y}\Big[\mu(2\frac{\partial v}{\partial y} - \frac{2}{3}div\mathbf{v})\Big] + \frac{\partial}{\partial z}\Big[\mu(\frac{\partial v}{\partial z} + \frac{\partial w}{\partial y})\Big] + \\
&\quad \frac{\partial}{\partial x}\Big[\mu(\frac{\partial u}{\partial y} + \frac{\partial v}{\partial x})\Big] + f_y \\
\rho\frac{Dw}{Dt} &= -\frac{\partial P}{\partial z} + \frac{\partial}{\partial z}\Big[\mu(2\frac{\partial w}{\partial z} - \frac{2}{3}div\mathbf{v})\Big] + \frac{\partial}{\partial x}\Big[\mu(\frac{\partial w}{\partial x} + \frac{\partial u}{\partial z})\Big] + \\
&\quad \frac{\partial}{\partial y}\Big[\mu(\frac{\partial v}{\partial z} + \frac{\partial w}{\partial y})\Big] + f_z.
\end{aligned} \tag{2.18}$$

In Equation 2.18, $\mathbf{v}$ is the vector of velocity, $u,\ v$ and w are the components of the velocity vector on the $x,\ y$ and z axis respectively. P is the pressure, μ is the dynamic viscosity and $f_x,\ f_y,\ f_z$ are the $x,\ y,\ z$ components of the body force vector.

Apart from the conservation of momentum, there is the conservation of mass (also known as the continuity equation) that is valid throughout the flow field:

$$\frac{\partial \rho}{\partial t} + \nabla \cdot (\rho \mathbf{v}) = 0 \tag{2.19}$$

In Computational Fluid Dynamics, the discretized Navier-Stokes equations are solved numerically in a spatial and temporal domain.

2.7 Turbulence

Turbulence is a rather complicated phenomenon that has been extensively studied by a large number of researchers. It is a state, in which the exact instantaneous flow is not

predictable but can be described with the help of statistical tools. It is highly effective in transferring momentum and energy [31]. In computational fluid dynamics, the most frequently encountered methods of handling turbulence are explained below.

1. **RANS:** The first approach to turbulence is RANS (Reynolds Averaged Navier-Stokes). In RANS simulations, the entire spectrum of turbulence is modelled. For the incompressible regime (which is the case for the current study), the Navier-Stokes equations are transformed from their dimensionless form (2.20), into the Reynolds-Averaged Navier Stokes (2.22), after splitting the solution into the ensemble average part and the fluctuating part, as shown in (2.21). A more detailed description of the process can be found in [20]:

$$\begin{aligned} \frac{\partial \underline{u}}{\partial t} + \nabla \cdot (\underline{u}\underline{u}) + \frac{1}{\rho}\nabla P - \frac{1}{Re}\nabla \cdot \nabla \underline{u} = 0 \\ \nabla \cdot \underline{u} = 0 \end{aligned} \tag{2.20}$$

$$\underline{u} = \langle \underline{u} \rangle + \underline{u}' \tag{2.21}$$

$$\begin{aligned} \frac{\partial \langle \underline{u} \rangle}{\partial t} + \nabla \cdot (\langle \underline{u} \rangle \langle \underline{u} \rangle) + \frac{1}{\rho}\nabla \langle P \rangle - \frac{1}{Re}\nabla \cdot \nabla \langle \underline{u} \rangle = -\nabla \cdot \langle \underline{u}'\underline{u}' \rangle \\ \nabla \cdot \langle \underline{u} \rangle = 0 \end{aligned} \tag{2.22}$$

The effect of turbulence in RANS equations is manifested via the term $-\nabla \cdot \langle \underline{u}'\underline{u}' \rangle$ of equation (2.22). This term, also known as the Reynolds Stress Tensor is the only one that includes the fluctuating part of the velocity vector. The rest of the terms are concerned with the mean flow. There is a number of ways to calculate the Reynolds Stress Tensor, all of which fall into 2 categories.

(a) **Eddy Viscosity Models**:
The eddy viscosity models are based on the assumption of Boussinesq [11]. This assumption states that there is a linear dependence between the turbulent shear stress and the rate of strain of the mean flow. The factor by which the shear rate is multiplied to yield the Reynolds stress tensor is called eddy viscosity [20].

$$-\langle u_i' u_j' \rangle \approx 2\nu_T S_{ij} - \frac{2}{3}\delta_{ij} k \ , \tag{2.23}$$

where: S_{ij} is the shear rate tensor and k is the turbulence kinetic energy.

(b) **Reynolds Stress Models**:
The second category of modelling turbulence in RANS simulations is the Reynolds Stress Models (RSM). Contrary to the eddy viscosity models, the Reynolds Stress Tensor in this category is calculated by solving the transport equation of the tensor. This method has a significant advantage over the Eddy

Viscosity approach. Turbulence is not considered to be isotropic, but the 6 independent components of the tensor are calculated separately. Nevertheless, the computational effort of the RSM models is in general higher than the Eddy viscosity models.

2. **DNS:** The second method of treating turbulence in CFD is Direct Numerical Simulation (DNS). It is the most expensive method, as far as the computational resources are concerned. For this reason, DNS is not widely used in industrial applications. Instead, the main use of DNS is for academic research. In the DNS approach, the Navier-Stokes equations are solved numerically without any approximations. Turbulence is resolved in all of its spectrum, from the large energy containing structures up to the smallest scales, called Kolmogorov scales. Due to this wide spectrum of turbulence scales, there is the requirement of extremely fine meshes and very small time-steps in the DNS approach [59]. More specifically, the number of cells that are required to conduct a DNS simulation scales with the Reynolds number of the flow. In the case of a three-dimensional flow, the relation between the number of cells and the scaling with the Reynolds number is the following [59]:

$$N \propto (Re)^{\frac{9}{4}} \tag{2.24}$$

Thus, due to the very high computational resources that are required, the DNS simulations are currently limited to low Reynolds number flows and academic applications.

3. **LES:** The last type of simulation based on the treatment of turbulence is Large Eddy Simulation (LES). As the name suggests, in LES the large structures of turbulence are resolved, while the smallest structures are modelled. This strategy of modelling only the least energetic turbulent structures stems from the observation that those structures are not case dependent. Instead, they present a universal behaviour [17]. Furthermore, the effect of the smallest turbulent structures is possible to be modelled. From a computational effort point of view, it is found in the middle, between the least computationally demanding RANS and the most demanding DNS. Thus, it is used for industry applications more frequently than the rather expensive DNS.

2.8 Time step and grid size

Determining the grid size and the time step of the simulation is a part of great importance. It is possible for the simulation to converge to an unrealistic solution or even diverge due to a poor quality mesh, or due to a time-step that is not suitable for the mesh. Thus, the determination of the time step is a decision that has to be taken bearing in mind the mesh size. For the correlation of the grid size and the time step, The Courant number can be used. The Courant number for a one dimensional advection problem is [23]:

$$C_r = \frac{U\Delta t}{\Delta x} \tag{2.25}$$

Having $C_r < 1$ means that during one time step, a particle travels less space in the spatial grid than the length of a cell. If an explicit scheme is used in the simulation, then it is necessary to have $C_r < 1$, otherwise the scheme is unstable [23]. During this study, the implicit unsteady solver of Star CCM+ was used, which is stable even if $C_r > 1$, however it was taken into consideration not to have $C_r > 1$ to yield high accuracy in the results.

2.9 Fluid Film modelling

Modelling of the fluid film is an essential part of the current study, since it affects the spray impingement process by changing the characteristics of the collision surface. In Star CCM+ software there is a dedicated model to simulate the flow of the fluid film. This model's main assumption is that the flow is a laminar boundary layer. The concept of boundary layer was first introduced by Ludwig Prandtl in 1904 [32] and a first solution to a two-dimensional boundary layer of flat plate was proposed by Blasius. Blasius conducted an order of magnitude analysis and simplified significantly the Navier-Stokes equations [53]. Furthermore, he proposed the similarity solution, where the velocity inside a boundary layer could be found numerically.

In order to find the solution of the boundary layer in Star CCM+, three transport equations are solved. The first is the continuity equation or conservation of mass equation [42]:

$$\frac{\partial}{\partial t}\int_{V'}\rho_f dV' + \int_{A'}\rho_f \mathbf{v_f}\cdot d\mathbf{a} = \int_{V'}\frac{S_u}{h_f}dV' \tag{2.26}$$

The second equation is the momentum equation [42]:

$$\frac{\partial}{\partial t}\int_{V'}\rho_f \mathbf{v_f} dV' + \int_{A'}\rho_f \mathbf{v_f}\otimes\mathbf{v_f}\cdot d\mathbf{a} = \int_{A'}\mathbf{T_f}\cdot d\mathbf{a} - \int_{A'}P_f d\mathbf{a} + \int_{V'}\left(\mathbf{f_b} + \frac{S_m}{h_f}\right)dV' \tag{2.27}$$

The third equation is the conservation of energy equation [42].

$$\frac{\partial}{\partial t}\int_{V'}\rho_f E_f dV' + \int_{A'}\rho_f H_f \mathbf{v_f}\cdot d\mathbf{a} = \int_{A'}\mathbf{q''_f} d\mathbf{a} + \int_{A'}\mathbf{T_f}\cdot\mathbf{v_f} d\mathbf{a} + \int_{V'}\mathbf{f_b}\mathbf{v_f} dV' + \int_{V'}\frac{S_E}{h_f}dV' \tag{2.28}$$

Those three equations are solved in a sub-domain of the mesh that is a surface which has one cell height. This type of domain is named Shell Region in Star CCM+. Since the equations are solved inside this specific domain, attention should be payed to the fact that the fluid film should not exceed the boundaries of this domain.

At this point is useful to mention that the fluid film modelling bears similarities with the regular flow field's conservation equations. However, it should be mentioned that one difference between the flow field equations and the fluid film equations is turbulence. In fluid film formulation, it is considered that there is no turbulence, while this assumption is not made in the RANS equations that are employed to solve the air flow field.

Regarding the heat transfer of the fluid film, in the current study the physics of the problem dictates that there is heat transfer between the liquid film and the hot wall of the piston. More specifically, between the fluid film model and the wall there is an

interface that allows the exchange of heat. Apart from the interface between the wall and the liquid film, there is the interface of liquid film and the surrounding air, which also allows the heat transfer between the two phases.

2.10 Parameters' space

In this section it is attempted to give estimations of the parameters that have been defined in previous paragraphs of the report. This is an important task, since a quantitative analysis of those parameters can give qualitative information on the results that are expected to occur from the subsequent numerical analyses.

2.10.1 Dimensionless numbers

- The first parameter of which there is the estimation is the Stokes number. The calculation of Stokes number gives information about the behaviour of the particles' trajectories inside the continuous phase. Following the definition of equation (2.5), the characteristic time of the particle is:

$$\tau_v = \frac{\rho_d D^2}{18\mu_c} = \frac{810.1 \cdot (0.35 \cdot 10^{-3})^2}{18 \cdot 0.02174 \cdot 10^{-3}} = 254 \cdot 10^{-3} s. \tag{2.29}$$

  It should be noted at this point that for the droplet diameter estimation, the cumulative distribution function of the droplet diameters was in accordance with the findings of the previous study that was conducted [54]. The median value of the droplet diameter distribution was $0.35 \cdot 10^{-3} m$. The density of engine oil ρ_d, is equal to $810 \frac{kg}{m^3}$. Finally, the last parameter that is needed as input for the calculation of the particle characteristic time is the dynamic viscosity of the continuous phase at $100°C$. The dynamic viscosity value was

  The characteristic time of the flow on the other hand is:

$$\tau_v = \frac{L}{U} = \frac{0.23}{8} = 28 \cdot 10^{-3} s. \tag{2.30}$$

  As far as the velocity is concerned, from CFD analyses it was found that when the flow rate of the oil was 7 lt/min, the velocity of the air in the cylinder was centred around the value of 8 m/s. The characteristic length of the flow is chosen to be equal to the length that an air particle has to cross before it impacts on the wall. This is approximately $L = 23cm$.

  Thus, an estimation of the Stokes number is:

$$St = \frac{254}{28} \approx 10. \tag{2.31}$$

  As it can be observed, Stokes number is considerably larger than unity. This means, that the liquid particles are expected to be detached from the flow and not follow the streamlines of the flow field.

- The second parameter that is covered is the Weber number. As it is shown in (2.3), Weber number depends on the density of the liquid, the velocity of the droplets, the diameter of the droplets and the surface tension of the liquid. While the density and the surface tension are properties of the liquid (oil), the droplet velocity and diameter are case dependent. To obtain an estimation of the Weber number, results of the previous study that was conducted at DAF [54] were used. More specifically, from CFD analyses it was found that when the flow rate of the oil was 7 lt/min, the velocity of the droplets was centered around the value of 10 m/s. Furthermore, for the droplet diameter estimation, the cumulative distribution function of the droplet diameters was also found in [54]. The median value of the droplet diameter distribution was $0.35 \cdot 10^{-3} m$. By substituting the above values into (2.3), it is possible to obtain a rough estimation of the Weber number of the bulk of the particles:

$$We_i = \frac{810.1 \cdot 10^2 \cdot 0.35 \cdot 10^{-3}}{0.024} = 1180. \tag{2.32}$$

  Considering the definition of the Weber number, which implies that it is the ratio of the inertial forces over the surface tension of the liquid, it can be observed that the inertial forces are significantly higher (three orders of magnitude) than the surface tension forces.

- The third parameter for which there is an estimation is the Laplace number. As it is shown in (2.4), Laplace number depends on 4 variables ($\sigma,\ \rho_d,\ D,\ \mu_d$), 3 of which are properties of the liquid. The only parameter that requires prior analysis to be obtained is the droplet diameter D. This parameter is equal to $0.35 \cdot 10^{-3} m$, as it is described in the context of discussion on Weber number (2.32). In the same manner that the median Weber number was calculated, the median Laplace number is:

$$La = \frac{0.024 \cdot 810.1 \cdot 0.35 \cdot 10^{-3}}{9.81 \cdot (9.542 \cdot 10^{-3})^2} = 7.6. \tag{2.33}$$

- Finally, as a part of the preliminary analysis of this study, the Bond number of the liquid film was calculated. The Bond number is defined as:

$$Bo = \frac{(\rho_f - \rho_c) g h_f}{\sigma}. \tag{2.34}$$

  In essence, it is the ratio of the force that is exerted to the film by the gravity over the force of the surface tension. Its importance on the study lies on the fact that if the $Bo \gg 1$, then this means that the destabilizing force of gravity is expected play a more important role compared to the surface tension. As a rough estimation of the stability of the film, it is possible to find a liquid film length for which the Bond number is equal to 1. This means that the gravitational force exerted on the film is the same as the surface tension:

$$h_f = \sqrt{\frac{\sigma Bo}{(\rho_f - \rho_c) g}} \Rightarrow h_f = \sqrt{\frac{0.024}{809 \cdot 9.81}} \Rightarrow \boxed{h_f = 1.74 \cdot 10^{-3} m.} \tag{2.35}$$

Having an estimation of the Weber number and the Laplace number, it is possible to use the Bai-Gosman model [7] in order to estimate the behaviour of a droplet whose diameter

is the median in the distribution that was found in previous study [54]. The critical Weber number is found from (2.8):

$$We_c = A_c \cdot La^{-0.18} \Rightarrow We_c = 1320 \cdot 7.6^{-0.183} \Rightarrow \boxed{We_c = 910.} \tag{2.36}$$

It can be observed that the incident Weber number that is calculated from (2.32) is greater than the critical Weber number of the Bai-Gosman model. This means that the bulk of the droplets are expected to splash upon impingement on the wall. When combined with the fact that the temperature of the wall is lower than the boiling temperature of oil, it can be inferred that the expected outcome of the impingement is on the left-most and upper-most region of the Figure 2.9.

2.10.2 Relevance of particle forces

In this part of the report, there is the estimation of the order of magnitude of the forces that are exerted on a particle from the flow field. This is achieved by taking the same particle that was considered in paragraph 2.10.1 and calculating the magnitude of the forces from the flow field.

The first force that is covered is the drag force. The drag force on a sphere is a topic that has been investigated thoroughly. A sample of studies on this field are by Schiller [37], Stokes [50] and Liu [26]. Before any further calculations, it is necessary to determine the Reynolds number of the particle:

$$Re_p = \frac{u_s \cdot D}{\nu_c} \Rightarrow Re_p = \frac{5.24 \cdot (3.5 \cdot 10^{-4})}{1.3 \cdot 10^{-5}} \Rightarrow \boxed{Re_p = 141.} \tag{2.37}$$

It should be pointed out that the velocity used in the Reynolds number is a numerical result (simulation reference) and is the average slip velocity of the particles was used.

For the drag coefficient, the Schiller-Naumann model is being used [37]. This means that for particle Reynolds number of 141, the drag coefficient is calculated from the subsequent formula:

$$C_D = \frac{24}{Re_p}\left(1 + 0.15 \cdot Re_p^{0.687}\right) \Rightarrow \boxed{C_D = 0.935.} \tag{2.38}$$

The total drag force on the particle is:

$$F_D = \frac{1}{2} C_D \rho_c A u_s^2 \Rightarrow \boxed{F_D = 1.45 \cdot 10^{-6} N.} \tag{2.39}$$

The next type of force that is covered in this paragraph is the Saffman lift force, defined in equation (2.17). An unknown of this equation is C_S, or the Saffman lift coefficient. According to the documentation of the software [40], for a particle Reynolds number of 141 C_S is found via the following formula [48]:

$$C_S = \frac{4.1126}{Re_S^{0.5}} \cdot 0.0524(0.5 Re_S)^{0.5} \Rightarrow \boxed{C_S = 0.15}\,, \tag{2.40}$$

where Re_S is the Reynolds number based on the curl of the flow field:

$$Re_S = \frac{\rho_c D^2 |\omega|}{\mu_c} \Rightarrow \boxed{Re_S = 8.5.} \tag{2.41}$$

It is important to mention that the curl of the velocity field was obtained from a numerical simulation close to the wall where droplets impinge. A representative value of the curl is found to be $\omega = 900\frac{1}{s}$.

Thus, having estimates of all the factors of equation (2.17), it is now possible to provide an estimate for the Saffman lift force on a particle close to the impingement wall:

$$\begin{aligned} F_S &= C_S \frac{\rho_c \pi}{8} D^3 (u_s \times \omega) \Rightarrow \\ F_S &= 0.15 \frac{1.18\pi}{8} (3.5 \cdot 10^{-4})^3 \cdot (4.5 \cdot 900) \Rightarrow \\ F_S &= 1.2 \cdot 10^{-8} N. \end{aligned} \tag{2.42}$$

The next particulate force that is covered in this paragraph is the virtual mass force. Following (2.15), the only unknowns are the acceleration terms of the fluid and the particle. Those terms are estimated from numerical simulation (simulation reference) and in essence they represent the average acceleration of the fluid and the particles on the last third of the cylinder before impinging on the wall. More specifically, it was found that the particles are decelerated as they travel $\frac{1}{3}$ of the cylinder downstream, from an average of $u_d = 8.9\frac{m}{s}$ to an average of $u_d = 8.4\frac{m}{s}$ in a time window of 23 ms. On the other hand, the air is accelerated from an average of $U = 4.77\frac{m}{s}$ to an average of $U = 5.29\frac{m}{s}$ travelling the same distance as the particles ($\frac{1}{3}$ of the cylinder length). Thus, the virtual mass force can be estimated:

$$\begin{aligned} F_{vm} &= 0.5 \frac{1.18 \cdot 2.24 \cdot 10^{-11}}{2} \Big(130.8 - (-216.2)\Big) \\ F_{vm} &= 2.3 \cdot 10^{-9}\ N. \end{aligned} \tag{2.43}$$

The last particulate force that is estimated is the gravitational force. This is given by Newton's second law:

$$\begin{aligned} F_g &= m_d \cdot g \Rightarrow \\ F_g &= 1.8 \cdot 10^{-8} \cdot 9.81 \Rightarrow \\ F_g &= 1.78 \cdot 10^{-7}\ N. \end{aligned} \tag{2.44}$$

One conclusion that can be drawn from this analysis of forces is that the force with the largest magnitude is drag. More specifically, the drag force is one order of magnitude larger than the gravitational force, which is the second largest. The third force by magnitude is the Saffman lift force, which was found to be two orders of magnitude smaller than drag and one order of magnitude smaller than gravity. The smallest force that is found to be

applied on a particle is the virtual mass force, which according to the analysis that was conducted was found to be 3 orders of magnitude smaller than drag.

Thus, it can be concluded that the calculations that were done on the context of the importance of the forces exerted on a particle agree with the conclusions of Yeoh [58] and Chrigui [14]. In those publications it is stated that the dominant force that is exerted on a particle is drag.

2.11 Spray heat transfer

2.11.1 Experimental validation paper

One paper that was found to be matching the needs of this study was conducted by Mudawar and Valentine [30]. It was deemed as suitable, since some parameters that affect the heat transfer (such as the droplet diameter and the spray mass flow rate) are in the same order of magnitude with the oil spray in DAF engines. In the paper of Mudawar, there is the experimental procedure that was followed in order to determine the heat transfer that is involved upon the impingement of a spray on a wall. Afterwards, there is the presentation of the heat transfer results from the procedure, which are of interest for the current study.

The experiments of Mudawar and Valentine [30] involve one heated surface, where the impingement takes place. The material of the heated surface is copper, as is the material underneath the surface. As it can be seen on Figure 2.11, the heater is insulated to prevent any heat losses from the sides of the experimental set-up. The heat is provided by electric cartridge heaters. Due to the insulation, the heat transfer is considered as one-dimensional, as it is directed from the cartridges towards the spray cooled surface. The measurement of the heat flux is conducted by monitoring the temperature gradient inside the heater. The temperature gradients are proven to be linear, thus the assumption of the author that heat transfer inside the heater is one-dimensional is confirmed.

The nozzle of the spray is located above the heater surface, facing downwards and is not depicted on Figure 2.11. Various nozzles are tested, with different spray cone angles and different nozzle pressures. In this way, the volumetric flux of the spray is controlled, and the velocity of the droplets is kept in the same order of magnitude.

One of the parameters that is used extensively for the characterization of the spray is the droplet diameter. It is elaborated on the paper that there are various diameters that can be found by using different techniques. For example, there is the Sauter mean diameter, which is defined as the diameter of a droplet that would have the same volume to surface ratio as that of the whole spray. Moreover, there is the mass median diameter. This is the diameter for which half of the spray's mass has larger droplet diameter, while the other half has smaller droplet size.

After defining the parameters that are described above, the experiments are conducted. The working fluid of the spray is water. It should be noted at this point, that water is kept at approximately constant temperature which is fluctuating between $22.5°C$ and $23.5°C$.

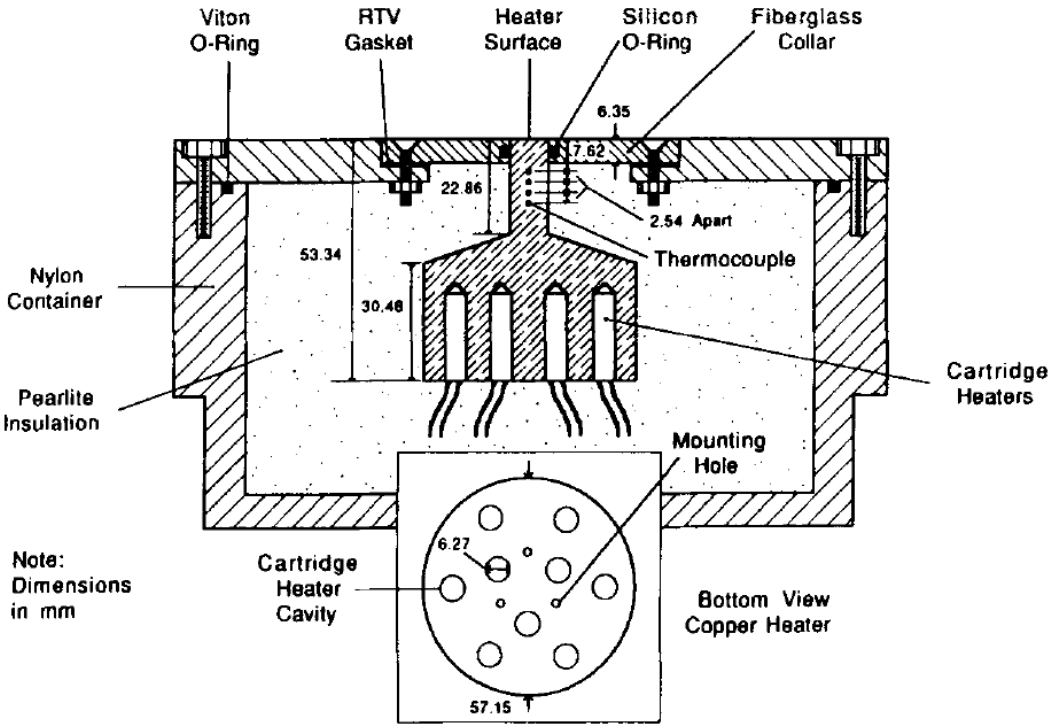

Figure 2.11: Experimental setup, reprinted from [30]

A number of experiments were conducted in order to collect data from a wide range of wall temperatures, spray volume fluxes and droplet velocities. It is important to mention that the wall temperature ranged from approximately $30°C$ up to $400°C$. Thus, this experimental campaign deals with a rather wide spectrum of the boiling curve, thus describing a number of different phenomena that take place. These include the single phase convection, nucleate boiling, transition boiling and film boiling. Out of those phenomena, the only range of interest for the current study was the single phase convection. This is because the oil coolant in an engine is below boiling temperature during the process of spraying. Thus, out of all the data that are published on this paper, there is analysis of the experiments that have low T_w. For this region of the boiling curve, the authors managed to derive correlations that linked the resultant heat transfer of the spray with flow parameters such as Re and Pr numbers. In the following graph, the curve of one of those correlations is shown.

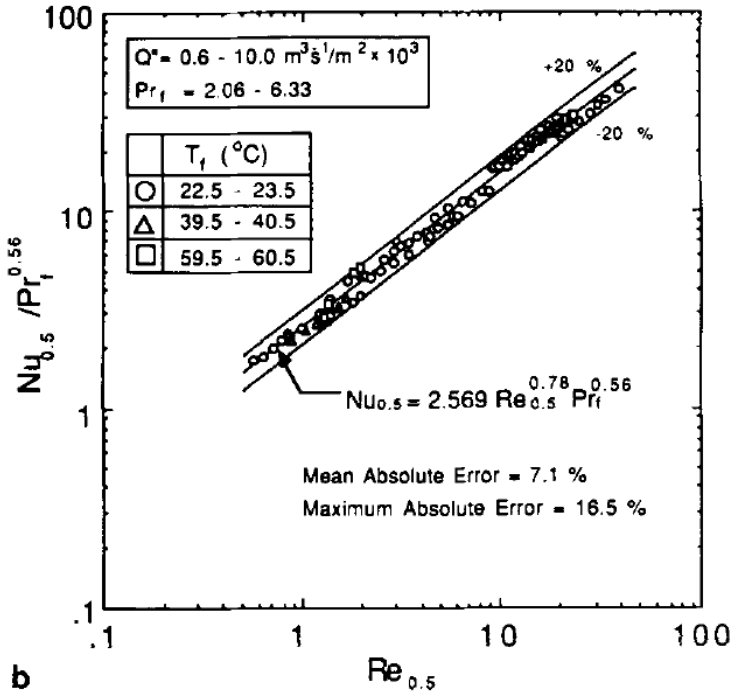

Figure 2.12: Nusselt number correlation, reprinted from [30]

At this point it is useful to clarify the correlation of Figure 2.12

The most frequent way that the Reynolds number is encountered is as

$$Re = \frac{U \cdot L}{\nu}. \tag{2.45}$$

where U is the characteristic velocity of the fluid, L is the characteristic length of the body (for a sphere it would be its diameter) and ν is the kinematic viscosity of the fluid.

However, in the case of the current paper, the spray Reynolds number is defined as:

$$Re = \frac{Q'' \cdot L}{\nu} \tag{2.46}$$

where the units of volumetric flux Q'' are: $[\frac{m^3}{m^2 s}] = [\frac{m}{s}]$.

It can be seen that there is an exponential relation of the Nusselt number with the Reynolds number. It is a positive exponent, so this means that when the Reynolds number increases, the Nusselt number (thus the heat transfer) increases as well. This qualitative observation is in agreement with the conclusion of the authors. The conclusion was that the volumetric flow rate of the spray plays a dominant role when it comes to the heat transfer between the wall and the spray.

Chapter 3

Spray verification

Until now, the literature review has taken place. At this part of this study, there is the creation of the first numerical model. The structure of this chapter is the following: At first, there is the explanation of the geometrical characteristics of the set-up, as well as the boundary conditions that are used. Afterwards, there is a presentation of the space and time discretization parameters, as the prime goal of this chapter is to obtain results that are mesh independent. Furthermore, there is the presentation of the physics that govern this particular problem. At the final stage of this chapter, there is the presentation of the numerical results and the conclusions that can be drawn from those.

3.1 Problem description

The goal of this part of the study is to investigate the behaviour of the oil droplets and the dominant parameters that affect their behaviour, as well as the effect of the mesh on the solution of the Lagrangian multiphase simulation. The delineation of the process that is followed throughout this chapter is the following: A cylindrical physical domain is created in the beginning. Afterwards, the boundary conditions are defined so that the simulation is a well posed problem.

At the bottom boundary of the cylinder (as shown at Figure 3.1) an Injector part is set up, so that particles be injected in the cylindrical domain. The particles' characteristics are defined based on the findings of the previous study conducted at DAF [54].

The last phase of this type of simulations is the post processing, a rather important stage of the study. In the post processing, there is the analysis of each solution that is obtained. Criteria are defined to determine the quality of each solution. The goal of this part of the study is to reach a mesh independent solution of the spray and the flow field, that is as computationally inexpensive as possible. It should be mentioned that in a simulation not including Lagrangian phase modelling, the user would only search for the mesh size at which further refinement would not yield more accurate results. However, in this simulation where there is Lagrangian modelling, there is the problem of

excessive refinement, which makes the process of mesh sensitivity analysis a non-trivial. This problem is addressed in paragraph 3.5.6.

3.2 Geometry and boundaries

The computational domain that is used during this set of simulations is a cylinder with diameter $D_c = 0.05m$ and height $H_c = 0.06m$. The reason of using this cylinder is that it is very close to an actual engine's cylinder dimensions, making it relevant to this study. The geometry of the cylinder as it was used in Star CCM+, can be seen on Figure 3.1. All of the three boundaries of the cylinder are set as pressure outlet. This choice is made so that the first part of the Lagrangian modelling simulations do not include wall impingement, but the focus is on the behaviour of the droplets prior to the expected impingement.

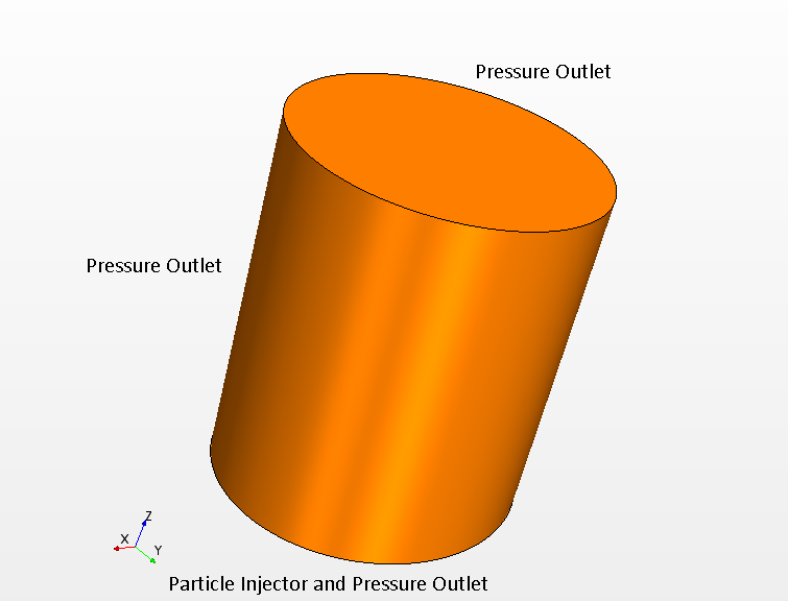

Figure 3.1: Explanation of Boundary conditions setup

3.3 Space and time discretization

The mesh type that is used throughout the study of spray is a structured mesh. In the software environment it is called trimmed mesher. The cells of the grid are hexahedral. The mesh parameters changed through the course of this set of simulations, since one of the major goals of this chapter is to examine the effect that the mesh has on the solution of the Lagrangian droplet phase, as well as on the continuous phase of air. The mesh that is created almost uniform. There is no need for refinement of a specific area, as it is frequently the case. This decision is taken based on the fact that there is no wall boundary condition, thus there is no need for refinement close to the boundaries, and also the particles are uniformly spread at the physical space, eliminating the need for any custom control of the mesh.

During the simulation campaign of this chapter, 6 different mesh sizes are used and 6 different timesteps.

Mesh	Size [m]	Cell count
1	$5 \cdot 10^{-4}$	960000
2	$7 \cdot 10^{-4}$	355000
3	$9 \cdot 10^{-4}$	170000
4	$1.1 \cdot 10^{-3}$	95000
5	$2 \cdot 10^{-3}$	16000
6	$3 \cdot 10^{-3}$	5000

Table 3.1: Mesh size and total cell number

The implicit unsteady solver of Star CCM+ is chosen, while the temporal discretization scheme used is of 2^{nd} order. The consideration behind the choice of timestep is related to the CFL number. For the accuracy of the solver it is considered good practice not to have CFL numbers much larger than unity. It is decided to follow this threshold, and to not exceed by a large margin this value, while the stability of the solver is monitored through the residuals. More specifically, it is mentioned in [20] that a CFL number smaller than 0.5 generally yields small time integration errors.

Number	timestep [s]
1	$3 \cdot 10^{-5}$
2	$5 \cdot 10^{-5}$
3	$7 \cdot 10^{-5}$
4	$9 \cdot 10^{-5}$
5	$2 \cdot 10^{-4}$
6	$3 \cdot 10^{-4}$

Table 3.2: Table of timesteps used

In total, 18 simulations of this type are conducted. The 16 first are finalized with the Design manager tool of Star CCM+, to automate the procedure of running. The mesh sizes and the time-steps of the simulations are shown on the following table:

Design number	Time-step [s]	Mesh size [m]
1	$3 \cdot 10^{-5}$	$5.0 \cdot 10^{-4}$
2	$3 \cdot 10^{-5}$	$7.0 \cdot 10^{-4}$
3	$3 \cdot 10^{-5}$	$9.0 \cdot 10^{-4}$
4	$3 \cdot 10^{-5}$	$1.1 \cdot 10^{-3}$
5	$5 \cdot 10^{-5}$	$5.0 \cdot 10^{-4}$
6	$5 \cdot 10^{-5}$	$7.0 \cdot 10^{-4}$
7	$5 \cdot 10^{-5}$	$9.0 \cdot 10^{-4}$
8	$5 \cdot 10^{-5}$	$1.1 \cdot 10^{-3}$
9	$7 \cdot 10^{-5}$	$5.0 \cdot 10^{-4}$
10	$7 \cdot 10^{-5}$	$7.0 \cdot 10^{-4}$
11	$7 \cdot 10^{-5}$	$9.0 \cdot 10^{-4}$
12	$7 \cdot 10^{-5}$	$1.1 \cdot 10^{-3}$
13	$9 \cdot 10^{-5}$	$5.0 \cdot 10^{-4}$
14	$9 \cdot 10^{-5}$	$7.0 \cdot 10^{-4}$
15	$9 \cdot 10^{-5}$	$9.0 \cdot 10^{-4}$
16	$9 \cdot 10^{-5}$	$1.1 \cdot 10^{-3}$
17	$2 \cdot 10^{-4}$	$2.0 \cdot 10^{-3}$
18	$3 \cdot 10^{-4}$	$3.0 \cdot 10^{-3}$

Table 3.3: Mesh size and time-steps of the first 18 simulations

3.4 Physics description

The initial state of the simulations is a stagnant air containing no Lagrangian phase. At $t = 0$, the injector starts spraying droplets inside the air domain. The settings of the injector are modified in such a way that they produce a spray close to that of [54]. More specifically, Venkatesh conducted an LES study, where some of the outcomes were the droplet size distribution as well as the velocity of the particles. It is important to mention that in the study of Venkatesh, the liquid phase was modelled with the Eulerian Multiphase physics and the Volume of Fluid approach. Thus, there are rather important differences with the approach of the current study. Moreover, the particle size distribution was found by using the blob detection model. As its name suggests, the blob detection model is used to identify droplets or bubbles in an Eulerian phase. Based on the detection model, it is possible to create a histogram of the particle size distribution. As one can read in [54], a number of such histograms was produced for various locations on the cylinder and various volumetric flow rates of oil. It was chosen to use the particle size distribution that corresponded to a volumetric flow rate of oil equal to $7\frac{lt}{min}$ while the location of the piston was at the Top Dead Center (TDC). The cumulative distribution function of the droplet sizes can be seen on Figure 3.2.

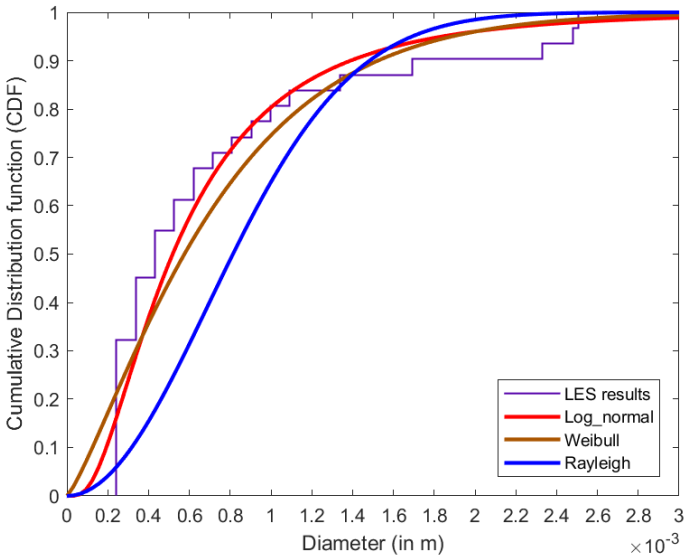

Figure 3.2: Cumulative distribution function of droplet diameter, reprinted from [54]

Injector: A significant portion of the parameters is modified based on data retrieved from the previous thesis inside DAF [54]:

- **Injector type:** In this set of simulations, the type of injector was *Surface Injector* was used. This means that all the particles entered the domain from one boundary of the domain. This boundary was the lower end of the cylinder, as it can be seen on Figure 3.1.
- **Flow rate specification:** This was a constant quantity for the study of this chapter. As it was mentioned, the volumetric flow rate of oil was $7\frac{lt}{min}$, which corresponds to a mass flow rate of $\dot{m} = 0.0945\frac{kg}{s}$.
- **Particle size specification:** For this aspect of the injector, the former study of Venkatesh was used. As an input, a table was created that corresponded to the Cumulative Distribution function of Figure 3.2.
- **Particle injection velocity:** According to the results of Venkatesh [54], the velocity of the particles was very close to being homogeneous. Thus, in the context of the injector, the particles are sprayed with a constant velocity, which is equal to $u_d = 10\frac{m}{s}$.
- **Injection Point Density:** Since the injector is a boundary surface of the physical domain, it is necessary to define the number of injection points on that surface. If the number of points is too large, then the computational cost of the simulation will increase significantly. On the other hand, if the number of injection points is small, then the number of injected parcels will be small as well. This has a negative effect on the statistical part of the Lagrangian modelling. When the number of injected parcels is low, this means that each parcel contains a large number of particles, all

having the same trajectory. Thus, there is a trade-off between the computational cost of the simulation and the accurate representation of the Lagrangian phase. In this part of the study, the density of injection points was chosen 100000 $\frac{pts}{m^2}$. The cylinder with radius $0.025m$ has cross-sectional area $A \approx 0.002m^2$, thus the resultant number of injection points on the surface is 200.

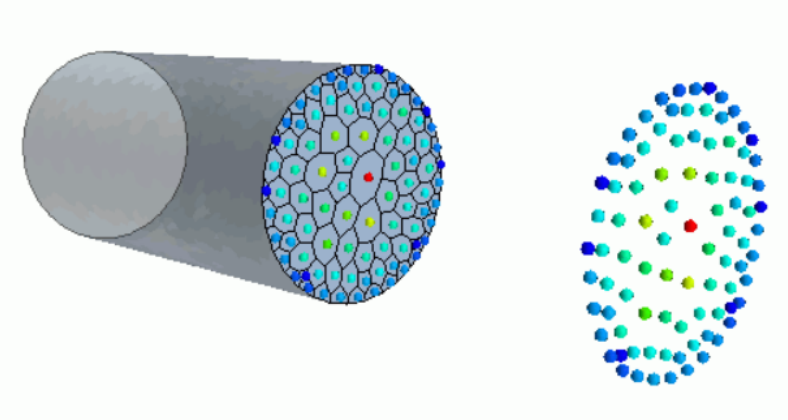

Figure 3.3: Visualization of a surface injector, reprinted from [45]

3.5 Results and discussion

3.5.1 Oil volume fraction

One of the parameters that is used to assess the mesh quality is the volume fraction of oil inside the cells. It is a parameter that can influence the results and their quality. Refining the mesh indefinitely leads to instabilities of the solver as well inaccuracy of the results, according to Senecal [39]. This phenomenon is directly related to high volume fractions of Lagrangian phase inside the mesh cells. Thus, the volume fraction of oil is a parameter that should be monitored closely.

Mesh size [m]	Max volume fraction	Average volume fraction
$5 \cdot 10^{-4}$	0.15	$6.22 \cdot 10^{-3}$
$7 \cdot 10^{-4}$	0.08	$6.22 \cdot 10^{-3}$
$9 \cdot 10^{-4}$	0.0744	$6.22 \cdot 10^{-3}$
$1.1 \cdot 10^{-3}$	0.0476	$6.22 \cdot 10^{-3}$
$2 \cdot 10^{-3}$	0.0505	$6.30 \cdot 10^{-3}$
$3 \cdot 10^{-3}$	0.0429	$6.20 \cdot 10^{-3}$

Table 3.4: Volume fraction of Lagrangian phase

The left-most column of the table that is presented above is the cell size of the 6 different meshes that were used. The middle column is the maximum value of the oil's volume fraction. This value was measured at the end of the physical time of the simulation, which

was at $t = 0.05s$. The third column is the average value of oil volume fraction. Again, it is a measurement at the end of the simulation's physical time. It should be observed that the average volume fraction remains rather insensitive to the changes of the mesh size. It is an expected result, since the average volume fraction of oil represents the volume of oil that there is in all of the physical domain, averaged by the total volume of the cylinder. Thus, it is logical that this value remains virtually constant by changing the mesh size. What is a rather sensitive parameter though is the maximum value of the volume fraction. This value is highly dependent on the cell size. As the mesh gets refined and the cells get smaller, the Lagrangian droplets occupy bigger portion of the cells' volume and the maximum volume fraction of the Lagrangian phase grows larger. This is an undesired effect, since in this way the assumption of the Lagrangian simulations that the cells are much larger than the droplets starts being invalid.

The advice of Senecal [39] related to the volume fraction of the Lagrangian phase was not to exceed volume fraction value of 0.1. It should be made clear that this limit was recommended as a "rule of thumb" rather than a hard limit that should not be crossed. The strategy that was followed in this set of simulations was to not exceed the recommendation of [39]. As it can be observed on Table 3.4, only in one mesh the volume fraction of the Lagrangian phase is greater than 0.1. As it is expected, this is the finest mesh that was used. As an extra measurement for this mesh, a threshold was created in Star CCM+. This threshold was used to indicate the cells where the volume fraction of oil exceeded 0.1. It was shown that 21 cells had volume fraction larger than 0.1. It should be reminded that the total number of cells in this simulation was 960000. This means that only 0.002% of the total cells exceeded the threshold. The simulation had no stability issues, and the results were in agreement with those of coarser meshes. After all, the solver of Star CCM+ intervenes when the volume fraction of the Lagrangian phase is greater than 0.75. Thus, the results of the finest mesh can be considered reliable in this aspect.

3.5.2 Weber number

In this part of the results, the behaviour of the particles' Weber number is presented, along with the description of the patterns that are observed on the graphs.

The process of monitoring the Weber number is as follows:

- The first step of the process is to determine the cells that participate in the monitoring of the Weber number. For this reason, Cell Sets are created in Star CCM+. As the name suggests, cell sets are clusters of cells that share a property that the user desires. In this case, the cell sets include all the cells that are in the close vicinity of the inlet of the cylinder, at 1/3 of the cylinder, at 2/3 of the cylinder and at the outlet of the domain. By vicinity, it is defined as the cells that are found within $0.7mm$ distance of the 4 aforementioned measurement cross-sections.

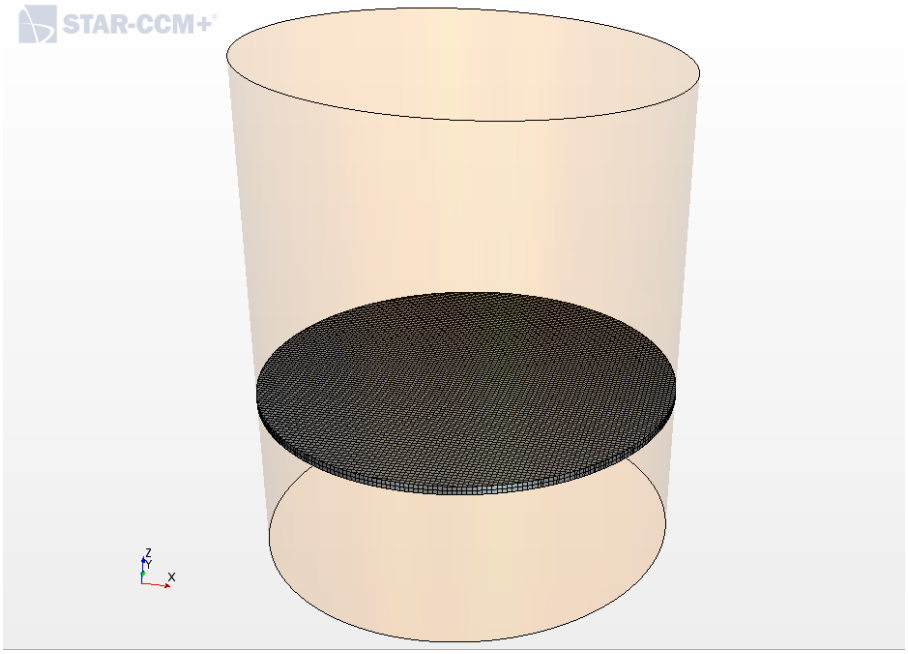

Figure 3.4: Cell set at 1/3 of the cylinder height

- Next is the creation of the field function that monitors the Weber number, as well as the creation of monitors that store at every time-step the average Weber number of the cell sets.
- For the post-processing part, it is not informative to plot the instantaneous data of the Weber number monitors. The data displayed a fluctuating behaviour as it can be expected. The solution to this is to use a moving average of the instantaneous data. The moving average is decided to take samples from the past approximately $0.015s$, so that the fluctuations be damped and there is a graph out of which conclusions can be drawn. This amount of time is decided because the initial decision was to take the moving average of 550 timesteps corresponding to the smallest time-step of $\Delta t = 3 \cdot 10^{-5} s$.

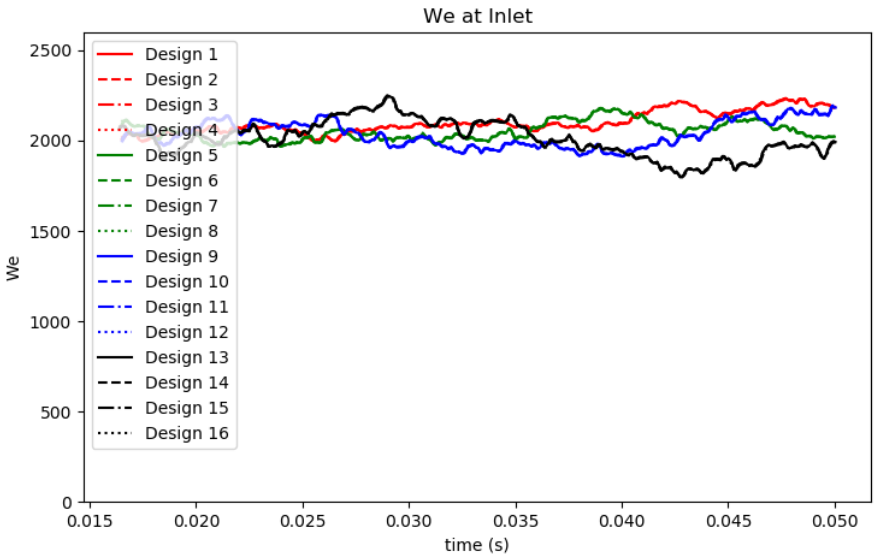

Figure 3.5: Moving average of the Weber number at inlet

At Figure 3.5 one can see the average Weber number of the particles at the inlet of the domain, where the injector is located.

There is one observation that needs to be made on this graph, which is also valid for the subsequent three Weber number graphs. Although there are 16 different curves, only 4 of them are distinguishable, the ones that have different colors. The curves that have the same color represent simulations where the time-step was held constant but the mesh size differed, according to the strategy that is presented at Table 3.3. This means that the particles have identical Weber number when the time-step remains the same, independent of the mesh size. There is an explanation behind this behavior and it lies on the Injector settings. In those settings, there is the option to randomise the injection timing as well as the injection points. It is chosen to activate those two randomizations, as this is the case in the real problem. The particles are not injected in the cylinder in an orderly manner neither in space nor in time. However, the spatial and temporal randomization in Star CCM+ is implemented based on the timestep of the simulation. Thus, when two simulations have the same timestep, the exact same particles will be injected, provided that the particle size distribution and the designated particle mass flow remain the same.

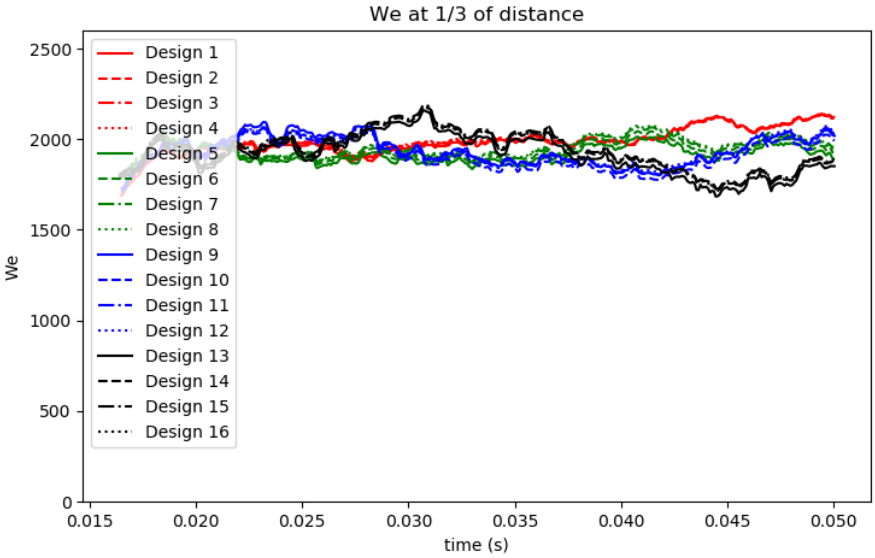

Figure 3.6: Moving average of the Weber number at 1/3 of the cylinder

Figure 3.6 shows the measurements at 1/3 of the distance between the injector and the outlet of the domain. As it is expected, the curves of the plot follow the same pattern as on the previous figure. The simulations that had the same timestep showed identical behaviour on the We number part. However there is one difference between figures 3.5 and 3.6. At Figure 3.6, the curves that have the same timestep (i.e. the same color), can now be distinguished from each other. They are spread, nevertheless it is clear that they follow the same trend.

The same patterns can be observed on the plots 3.7 and 3.8. It can be seen that as we move downstream of the inlet, there is uncertainty of the We number, which is related to the mesh size. As someone can assume, different meshes produced different flow fields. The flow field from its side determines the trajectories of the particles, so it is important to examine what is the difference between the Weber number curves.

It is believed that turbulence played an important role on the discrepancies between the graphs of the Weber numbers with the same color. For this reason, the average turbulent kinetic energy and the average turbulent dissipation rate for the 16 cases are shown in Table 3.5. There is one pattern that can be observed by comparing Table 3.5 and the figures of the Weber number. It can be seen that the curves of the same color are offset from one another. It was found that there is a strong correlation between the average turbulent kinetic energy of the simulation and the offset of the curves. More specifically, the simulations with higher turbulent kinetic energy are offset towards the lower parts of the diagrams. This can be explained if the effect of turbulence on the particles is taken into consideration. In general, turbulence in RANS simulations is modelled as a term of viscosity. Thus, the particles are expected to have a lower velocity in a case where there is more turbulence, resulting in lower Weber number.

Design #	Turbulent kin. energy [J/kg]	Turbulent dissipation rate $[m^2/s^3]$
1	$5.03 \cdot 10^{-3}$	$8.14 \cdot 10^{-1}$
2	$2.76 \cdot 10^{-3}$	$2.76 \cdot 10^{-1}$
3	$3.11 \cdot 10^{-3}$	$2.74 \cdot 10^{-1}$
4	$2.40 \cdot 10^{-3}$	$1.56 \cdot 10^{-1}$
5	$4.88 \cdot 10^{-3}$	$6.62 \cdot 10^{-1}$
6	$3.75 \cdot 10^{-3}$	$2.63 \cdot 10^{-1}$
7	$3.30 \cdot 10^{-3}$	$3.62 \cdot 10^{-1}$
8	$2.68 \cdot 10^{-3}$	$2.36 \cdot 10^{-1}$
9	$3.19 \cdot 10^{-2}$	$3.24 \cdot 10^{0}$
10	$3.89 \cdot 10^{-3}$	$2.55 \cdot 10^{-1}$
11	$3.35 \cdot 10^{-3}$	$3.76 \cdot 10^{-1}$
12	$2.35 \cdot 10^{-3}$	$1.43 \cdot 10^{-1}$
13	$5.17 \cdot 10^{-3}$	$6.56 \cdot 10^{-1}$
14	$3.72 \cdot 10^{-3}$	$1.89 \cdot 10^{-1}$
15	$3.35 \cdot 10^{-3}$	$3.33 \cdot 10^{-1}$
16	$2.35 \cdot 10^{-3}$	$1.15 \cdot 10^{-1}$

Table 3.5: Turbulent kinetic energy and turbulent dissipation rate

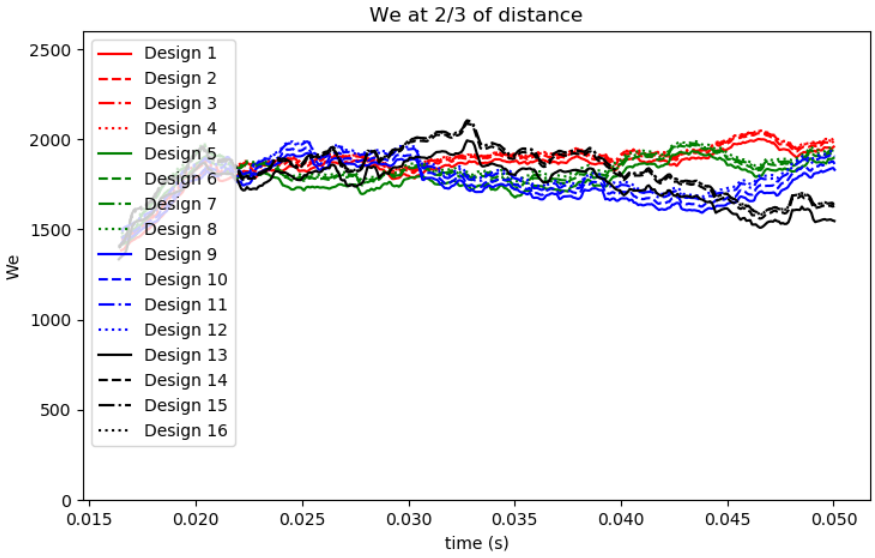

Figure 3.7: Moving average Weber number at 2/3 of the cylinder

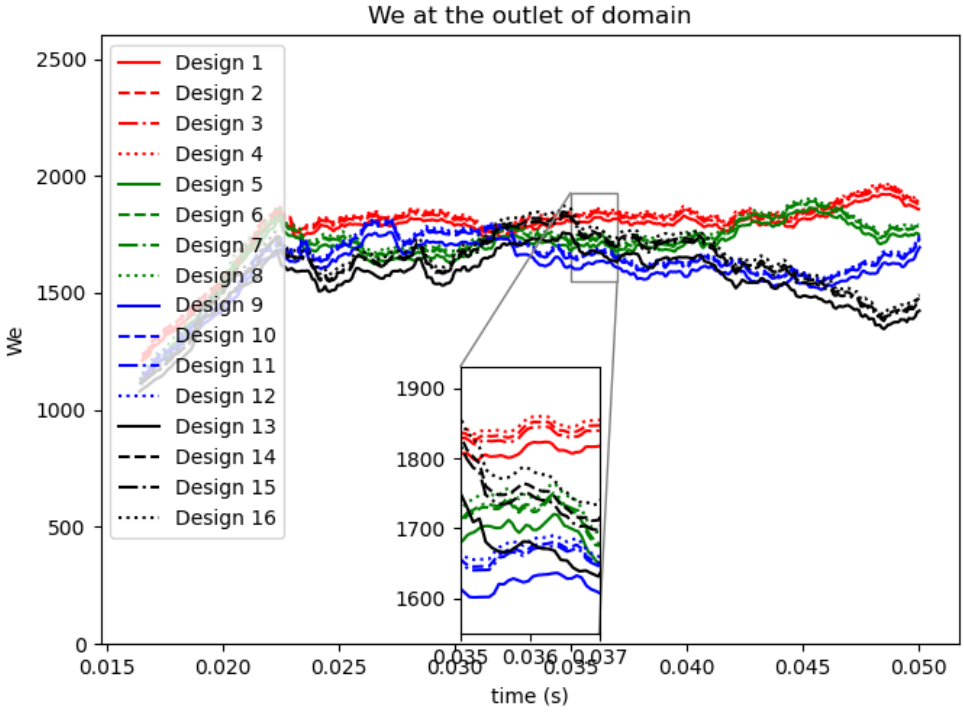

Figure 3.8: Moving average Weber number at the outlet of the domain

3.5.3 Mass flow rates

In this paragraph, there is the presentation of the behaviour of mass conservation in the physical domain, or else the mass flow rates at the boundaries of the cylinder. The four graphs depicting the mass flow rates of air are in Figures 3.9-3.12. The signs of the flow rates indicate the direction of the flow. A negative flow rate means that the flux is from the environment towards the cylinder.

It can be seen that curves of the same color are in close proximity among each other. More importantly though, it is observed that curves of the same color follow the same path with relatively small deviations. At this point, it should be reminded that the curves of the same color have common time-step. Moreover, as it is explained in paragraph 3.5.2, in simulations with common time-step, the exact same particles are injected at the exact same time. Due to two-way coupling, if the same particles are injected at the same time, then the same amount of air is expected to flow towards and out of the cylinder. This is an explanation based on the assumption that there is no source of mass flow acting in the simulation. There is no prescribed pressure difference between the inlet and outlet boundaries of the cylinder. Thus, the only known cause of air flow is the particles that are accelerating their surrounding air.

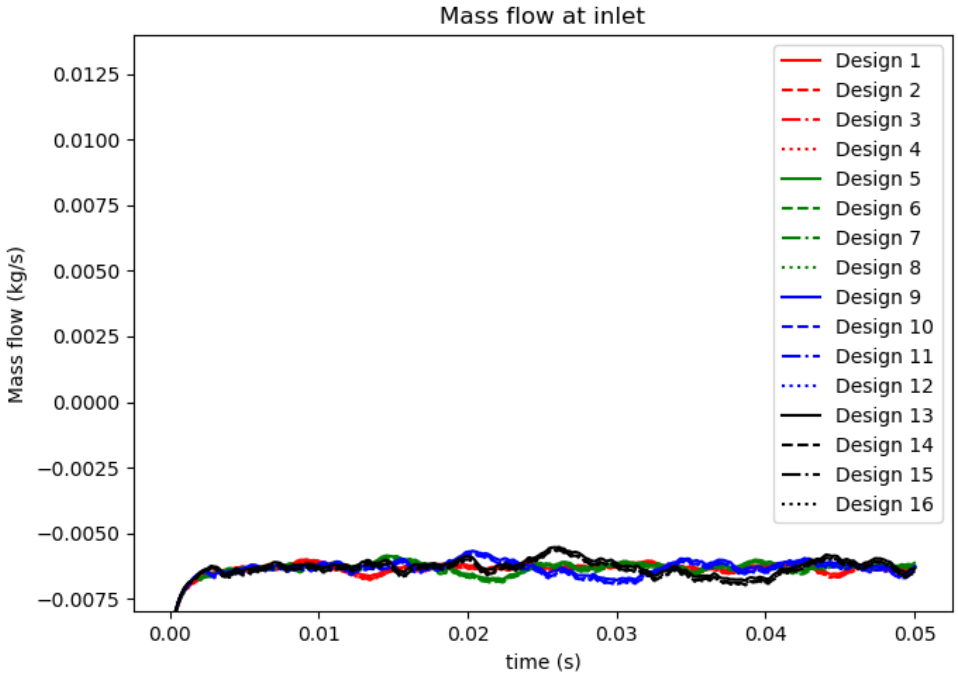

Figure 3.9: Mass flow rate, inlet of domain

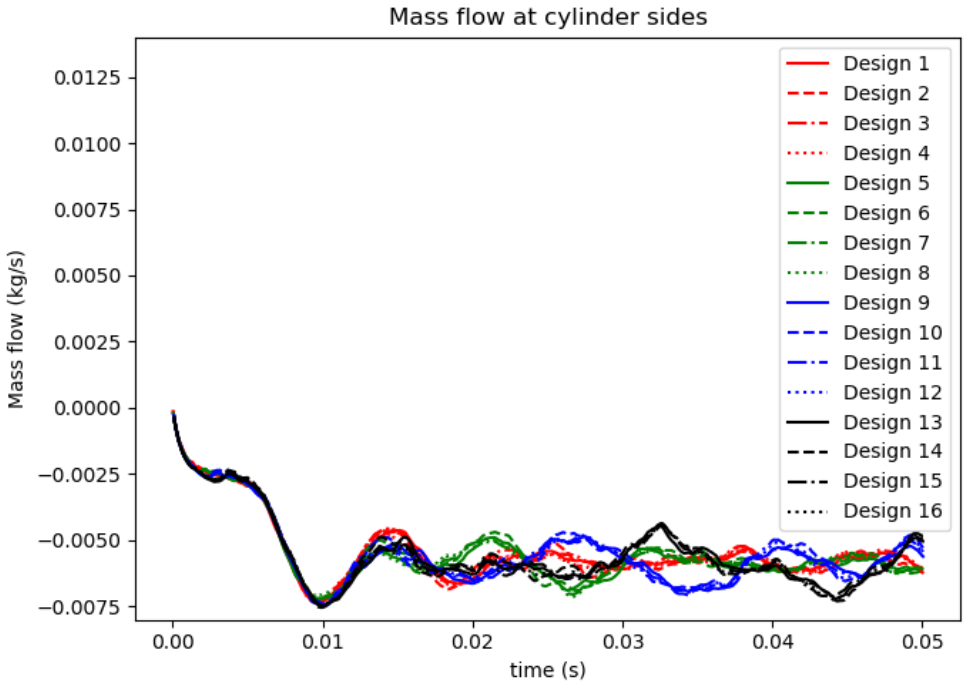

Figure 3.10: Mass flow rate, side of cylinder

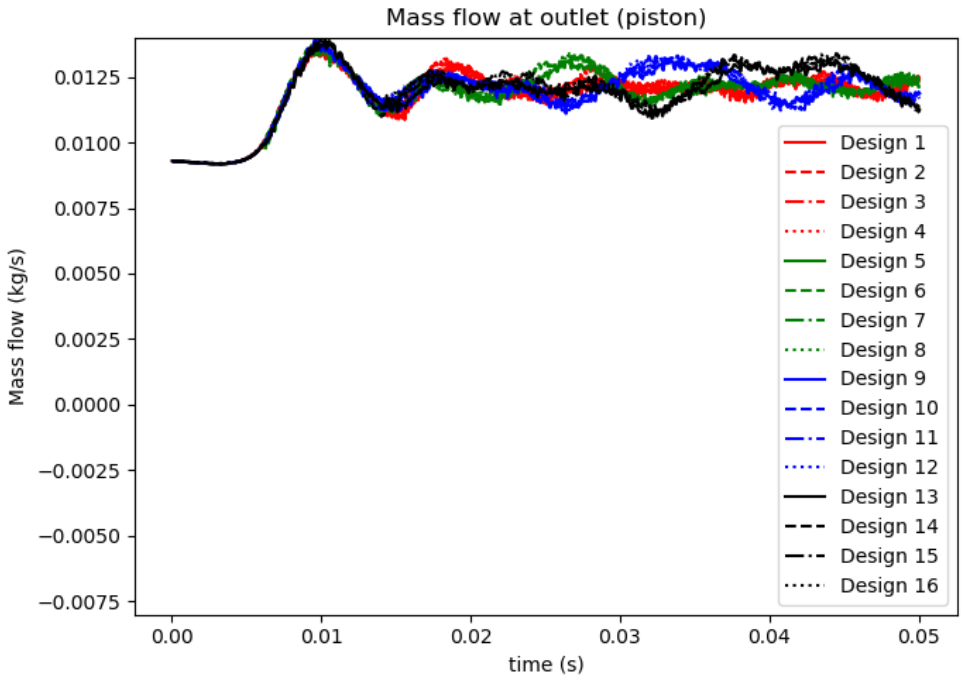

Figure 3.11: Mass flow rate, outlet of domain

As far as the total net mass flow rate of air is concerned, the behaviour of the simulation is as expected. There should be zero net flux of air towards the cylinder, since the flow is incompressible. It can be seen that there are small oscillations having amplitude in the order of $10^{-4}kg/s$. The order of magnitude of the mass flow rate at the boundaries is $10^{-2}kg/s$, two orders larger than the oscillations of the net flow in the domain. Based on visual impression, the oscillations do not follow a pattern and they can be characterized as random, having a mean value equal to 0. One can observe in Figure 3.12 that there is no significant effect of mesh resolution or time-step on the continuity of the flow field. However, what can be observed is that curves of the same color (i.e. having the same time-step) oscillate in the same phase. This is attributed to the fact that when there is the same time-step, there is injection of identical droplets, thus through the two-way coupling there is the same mass flow rate of air as it is explained above in the current paragraph.

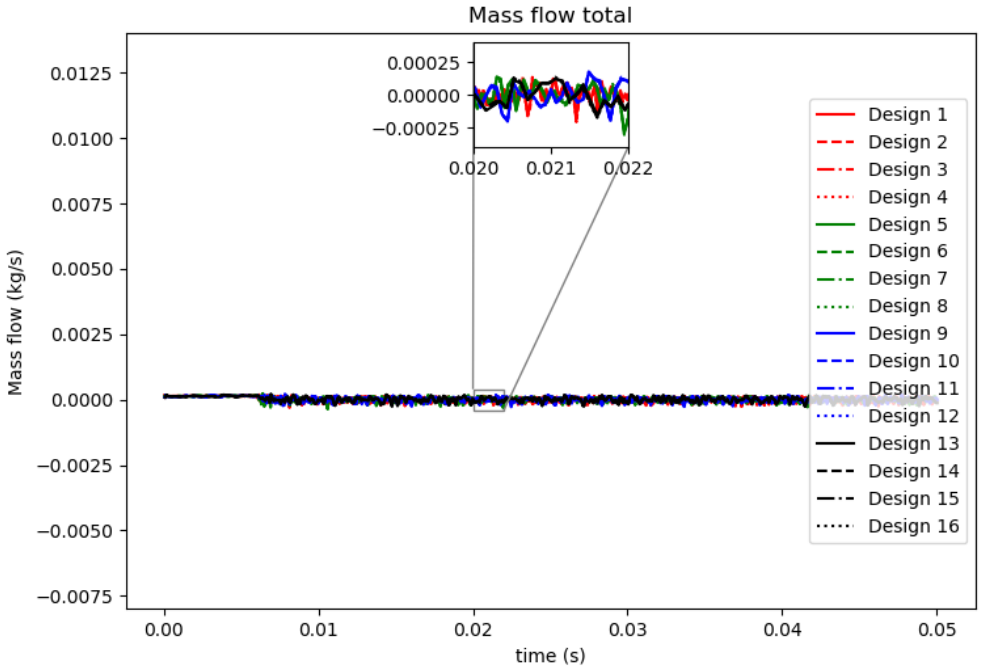

Figure 3.12: Net mass flow rate of domain

3.5.4 Streamlines

The streamlines of the flow field can be a useful tool to inspect visually the resultant flow field of the simulation. Although it is an aspect of the study that cannot be quantified, some important conclusions can be drawn by analysing them. One can see on Figure 3.13 the streamlines of the simulation with the highest mesh resolution and the smallest time-step. As the streamlines start from the inlet of the domain (the bottom of the cylinder in Figure 3.13), they consistently converge towards the center of the domain. As an implication of this fact, it means that there is acceleration of the air as one moves downstream. This is an expected behaviour, since the Lagrangian particles are accelerating particles of air through the two-way coupling. At this point it should be mentioned that all of the simulations that were conducted, produced streamlines with no perceptible differences. Consequently, not all of them are presented here for reasons of brevity. Furthermore, it should be reminded that this behaviour can be observed during the simulations that have Pressure Outlet boundary condition at all of the 3 boundaries of the cylinder. Adding a wall, or in general changing the boundary conditions of the simulation, would yield a different flow field.

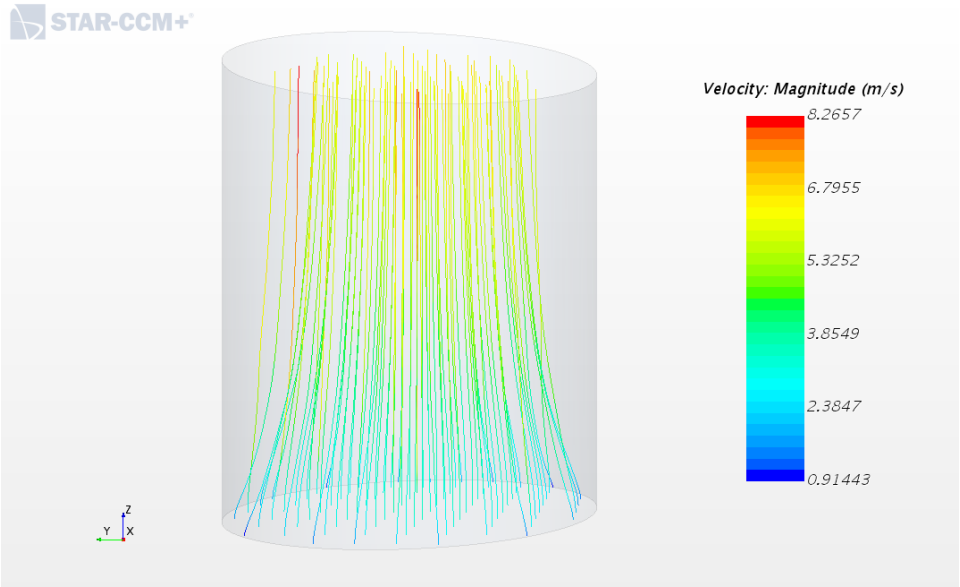

Figure 3.13: Streamlines of design 1 simulation

3.5.5 Pressure

Apart from the streamlines, the pressure field is also monitored closely through the course of this study. For this reason, it is chosen to illustrate the static pressure field on a plane. The symmetry of the flow around the z axis (as it is defined at Figure 3.14) allows to choose either a plane normal to x or to y axis without affecting the resultant graphs.

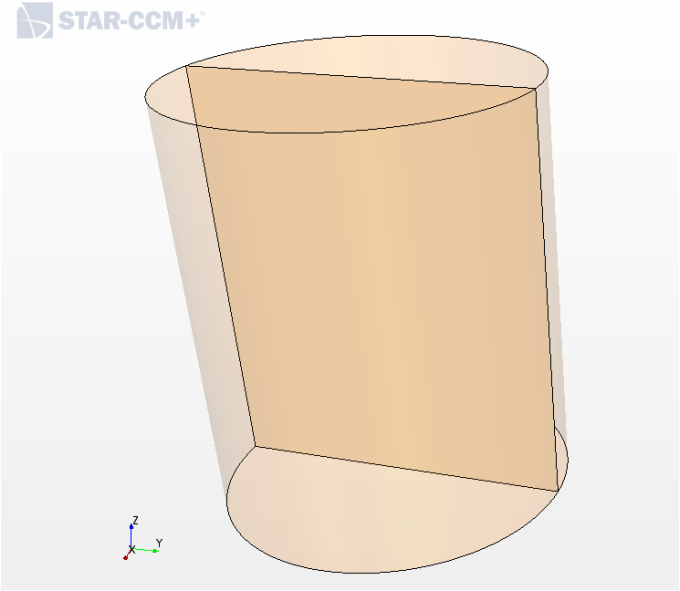

Figure 3.14: Plane section of pressure visualization

To begin with, it can be seen on Figure 3.15 that the static pressure at the inlet boundary

(bottom) is lower than atmospheric (in essence, this figure shows the pressure difference relative to the atmospheric pressure).

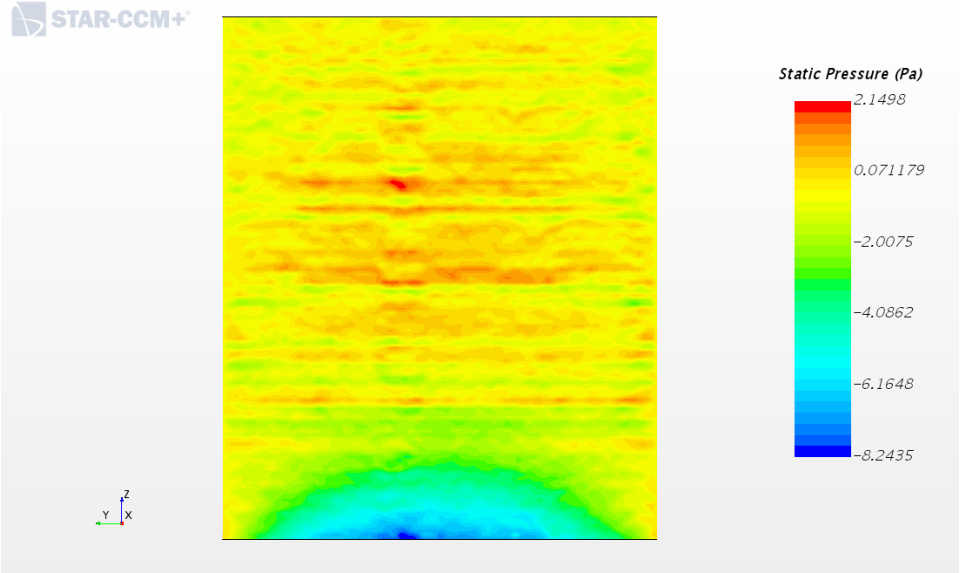

Figure 3.15: Instantaneous static pressure scene of design 1 simulation

There are some patterns that can be distinguished at the pressure field of Figure 3.15. At first, the static pressure is expected to rise upstream of a particle, while it is expected to fall downstream of a particle, according to Southard [49]. The pressure distribution around a sphere for laminar and turbulent boundary layer can be seen at Figure 3.16.

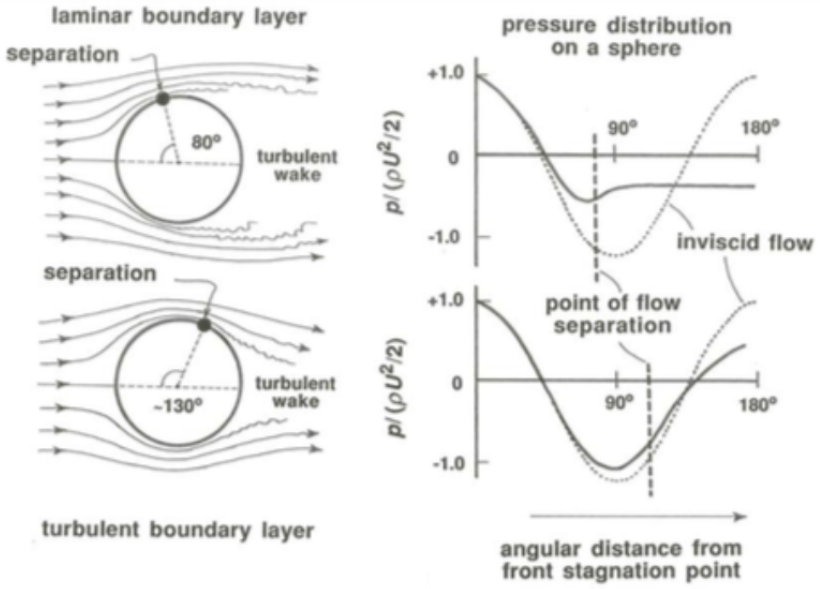

Figure 3.16: Pressure distribution around a sphere, reprinted from [49]

One particle would not create a significant difference on the pressure field, since the size of the cylinder is significantly greater than the size of an oil particle. However, in the simulations of this chapter, the particles can macroscopically affect the flow field. The cumulative effect of all the particles is to increase the static pressure as they travel towards the outlet of the domain. This pressure increase can be viewed at Figure 3.15. It is important to mention that the pressure rise is not monotonic. This happens because there can be flow from the sides of the cylinder. In the case of a cylinder with a wall side boundary, the pressure rise due to the particles would indeed be monotonic. The same patterns are observed on all of the simulations of this chapter, independent of the mesh size or the time-step.

3.5.6 Refinement limit

The topic of this section is related to an attempt to find the limit of refinement of the mesh. There is an elaborate explanation on why the mesh in the Lagrangian-Eulerian simulations cannot be refined indefinitely and it can be found on paragraph 3.5.1.

As a proof of concept, it is decided to run a simulation with an even finer mesh was used to test the limit of the results' validity. This mesh has a cell size equal to $4 \cdot 10^{-4} m$ and the total cell count is $1,870,200$. To put in in perspective with the previous meshes, the finest mesh that is presented in Table 3.4 has cell size equal to $5 \cdot 10^{-4} m$, while the total number of cells was $960,000$. The impact that this change of mesh has on the resultant volume fraction of oil is significant. It is found that 56806 cells have oil volume fraction larger than 0.1. As a percentage, 56806 cells represent the 3% of the total number of cells. As it is going to be shown, this amount of cells having high volume fraction of oil was capable of degrading the results of the simulation.

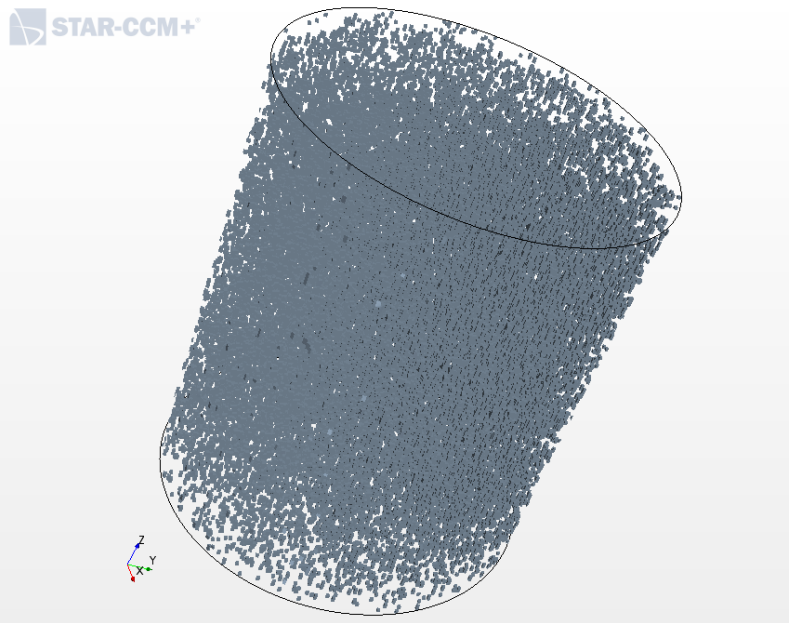

Figure 3.17: Scene of cells having oil volume fraction greater than 0.1

Weber number plots In this paragraph there is the presentation of the Weber number plots, in the same manner that they are depicted on paragraph 3.5.2. On all 4 graphs, there is no systematic discrepancy between the refined mesh and the other 4 simulations that were conducted earlier. As it was discussed earlier, the differences of the graphs at the 2/3 of the cylinder and at the outlet are attributed to different turbulence levels of each solution. Thus, over-refining the mesh does not have significant impact on the Weber number of the particles.

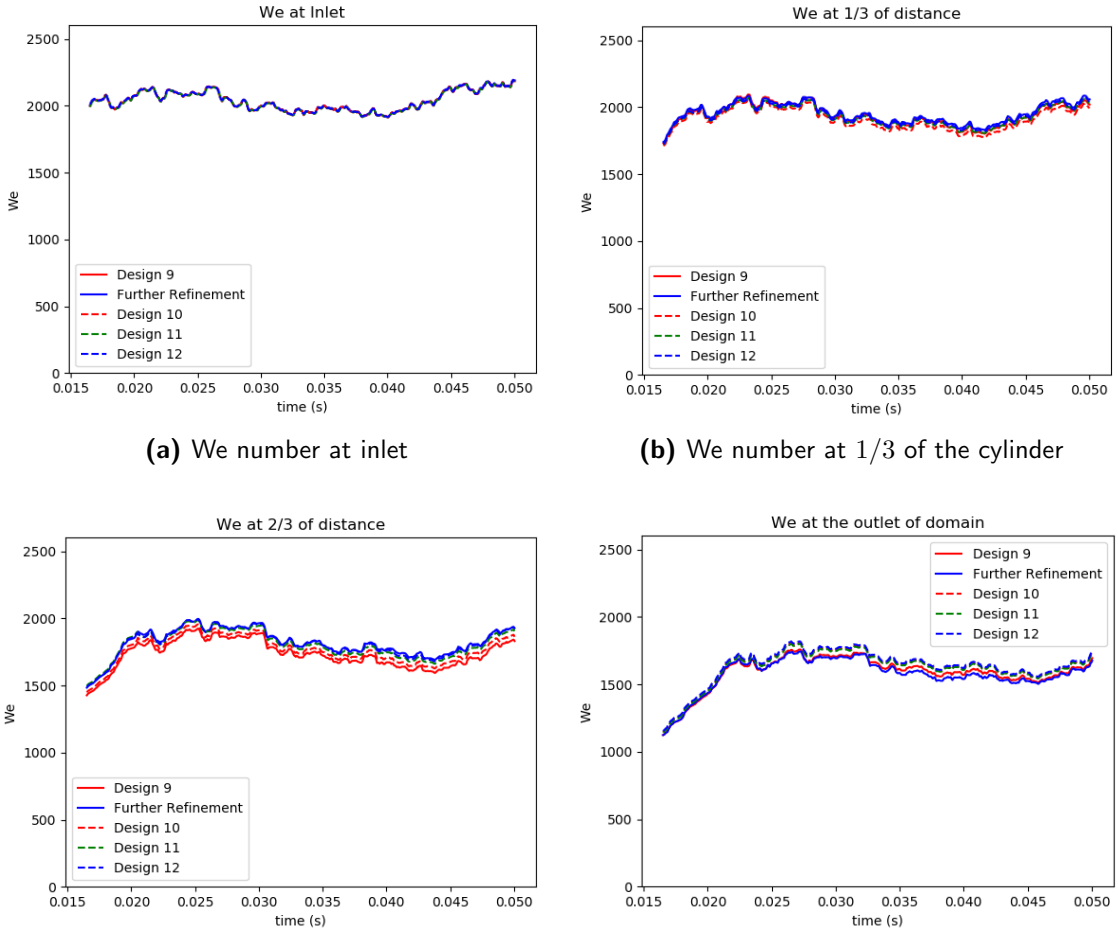

(a) We number at inlet

(b) We number at 1/3 of the cylinder

(c) We number at 2/3 of the cylinder

(d) We number at the outlet of the cylinder

Figure 3.18: Weber number plots at various locations of the cylinder

Boundary mass flow rates In this paragraph there is the presentation of the mass flow rates of air through the boundaries of the domain. Contrary to the outcome of the Weber number, the results are rather different when it comes to the mass flow rate of air. Figure 3.19 shows the mass flow rate at the boundary of the inlet. It can be seen that there is one curve that is rather distinct from the remaining curves. It is the solid blue line that represents the finest setting of the mesh. The difference of this curve and the median curve of the remaining 4 is calculated to be 12%. This is considered significant discrepancy, since the margin between the remaining 4 curves is equal to 2%. It is believed that over refining is the root cause of this discrepancy between the bulk of the lines and

the blue one. As it was explained in paragraph 4.3.2 refining beyond the point of having large volume fraction of Lagrangian phase in the cells can lead to miscalculation of the drag in the continuous phase. Thus, due to the two-way coupling between the Lagrangian and the Eulerian phase, there is discrepancy in the amount of air that the Lagrangian particles are "dragging" into the spatial domain.

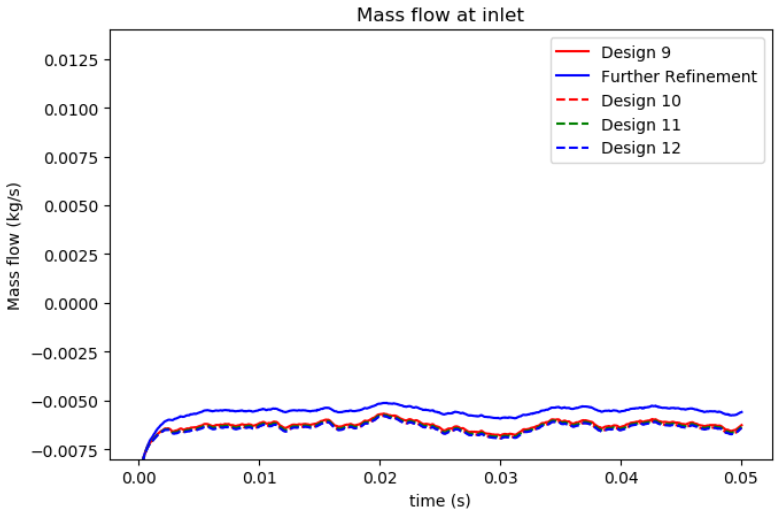

Figure 3.19: Mass flow rate at the inlet of the cylinder, comparison of simulations

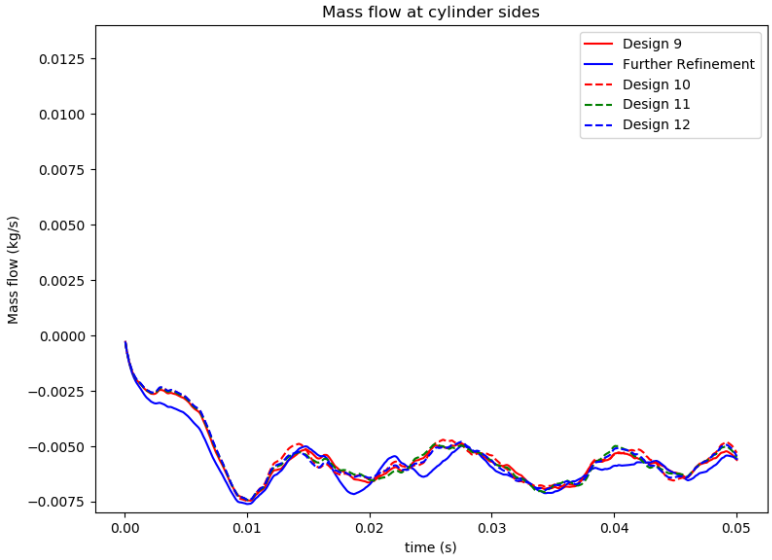

Figure 3.20: Mass flow rate at the sides of the cylinder, comparison of simulations

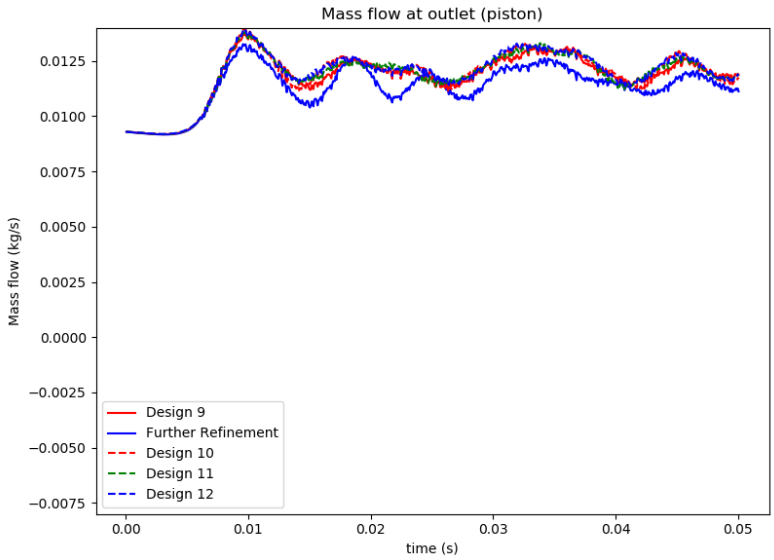

Figure 3.21: Mass flow rate at the outlet of the cylinder, comparison of simulations

In Figure 3.22, it can be observed that there is no systematic error occurring from refining the mesh. There are small oscillations that have amplitude in the order of $10^{-4}kg/s$, while the over-refined mesh does not depict diverging behaviour from the rest of the meshes. The order of magnitude of the mass flow rate at the boundaries is 10^{-2}, two orders larger than the oscillations of the total flow in the domain. Thus, it is believed that in all of the tested meshes the continuity of the flow field is respected up to the numerical precision.

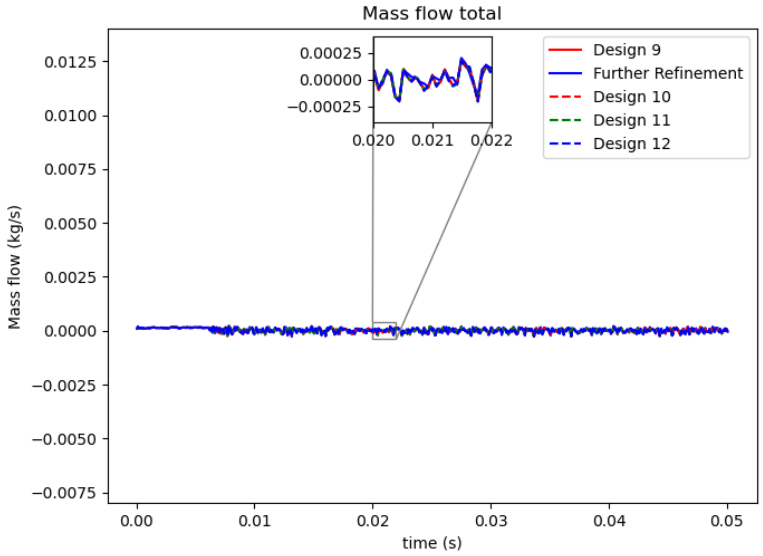

Figure 3.22: Total net mass flow rate of the cylinder's boundaries, comparison of simulations

Pressure at the boundaries Apart from the measurement of the mass flow rates at the boundaries of the domain, it was deemed useful to monitor the pressure as well. Figures 3.23, 3.24 and 3.25 depict the average static pressure of the 3 different cylinder

boundaries. It can be observed at Figure 3.23 that there is one curve that is distinct from the other 4 curves. This is the curve of the finest mesh size. It follows the same pattern as the mass flow rate graph 3.19. It was calculated that the average difference between the solid blue line and the median of the remaining 4 curves is 20%. Similarly as the mass flow graphs, the discrepancy is attributed to the excessive refinement of the mesh.

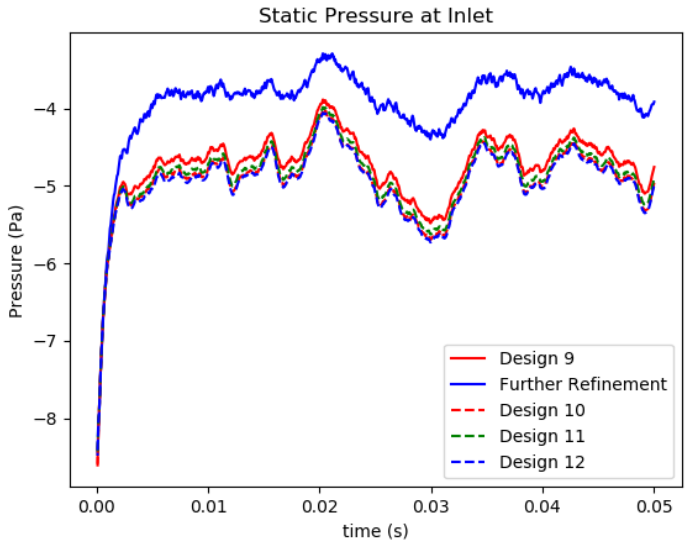

Figure 3.23: Static pressure at the inlet of the cylinder

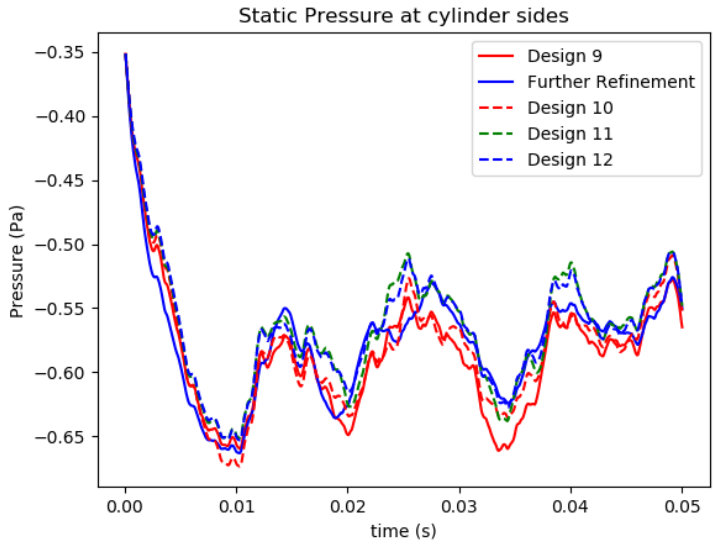

Figure 3.24: Static pressure at the sides of the cylinder

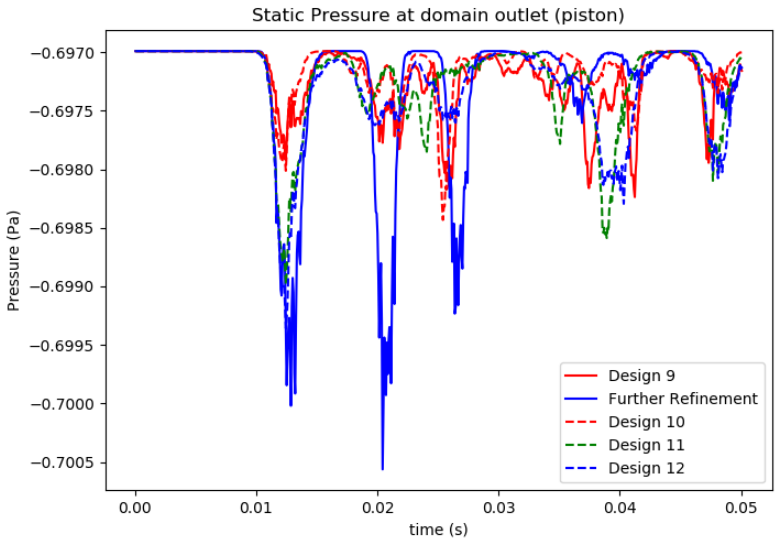

Figure 3.25: Static pressure at the outlet of the cylinder

Chapter 4

Impingement Validation

4.1 Objective of this Chapter

Before conducting simulations that are related to DAF engines' conditions, it is of great importance to validate the chosen models based on the comparison between the results of the numerical model that is built and the results of a reference experiment available in literature.

4.2 Reference experiment

The paper of Motzkus et al. [29] is used as reference to validate the numerical model that is built. The main purpose of Motzkus in this study is to analyse the post-impingement behaviour of droplets under certain conditions, which are described at the following paragraphs.

In their experimental campaign, Motzkus et al. [29] used a high speed CCD camera to visualize and analyze the process of impingement. A sketch of the experimental setup can be seen on Figure 4.1. The impingement can be characterized as a 'wet wall' impingement, since the droplets were impacting on a pool of the same liquid. The height of this fluid film was measured through the non-dimensional parameter S_f, where:

$$S_f = \frac{\delta}{D}. \tag{4.1}$$

Apart from the dimensionless fluid film thickness, the droplet diameter also changed in the course of the experiments. The range of the droplet diameters had a minimum of $1.9mm$ while the maximum value was $4.3mm$.

Another parameter that was variable through the experimental campaign was the impact velocity of the droplets. The impact velocity could be adjusted by changing the height

from which a droplet would fall. The range of impact velocities was from $1.32\frac{m}{s}$ up to $4.5\frac{m}{s}$. This range refers to the set of experiments that were validated through simulations.

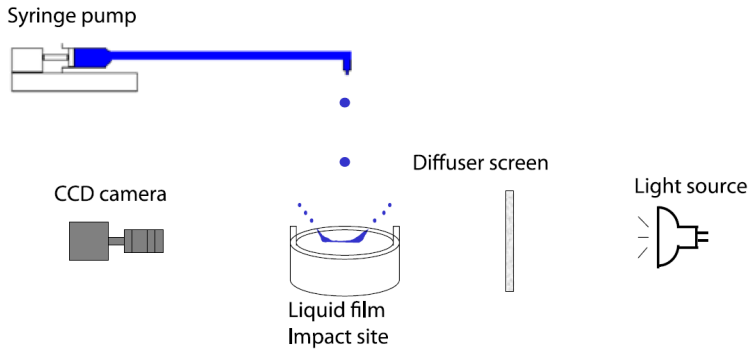

Figure 4.1: Sketch of the experimental setup, reprinted from [28]

Experiments with 3 liquids were performed: The first material was water, the second material was a 50% mixture of water and ethanol and the third liquid was a mixture of 45% water and 55% glycerol. By using different liquids, the authors of the paper could control the density, the viscosity as well as the surface tension of the working fluid. This change of the fluid properties has an impact on dimensionless numbers of the experiments, such as the Ohnesorge and Weber numbers.

4.3 Simulation set-up

4.3.1 Geometry and boundaries

The computational domain that was used to replicate the experiments that were done by Motzkus [28] was a cylinder with diameter $D_c = 0.05m$ and height $H_c = 0.06m$.

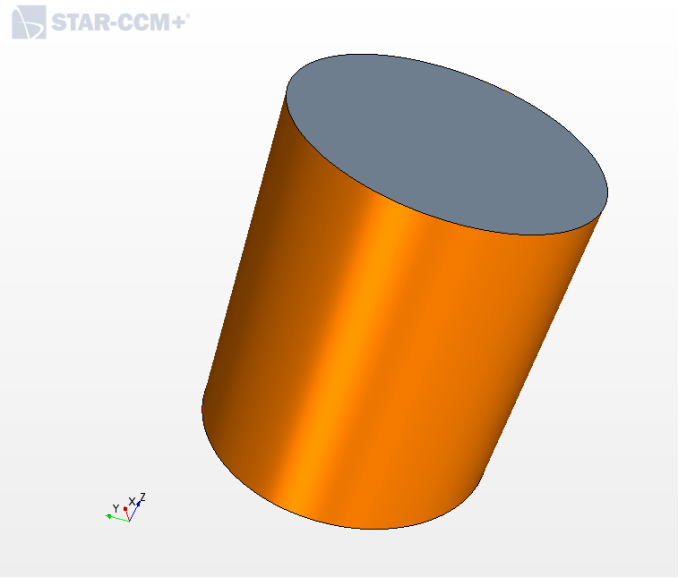

Figure 4.2: Geometrical domain of the simulation

To get insight into the model that was developed, the boundary conditions of the simulation are presented in Figure 4.3:

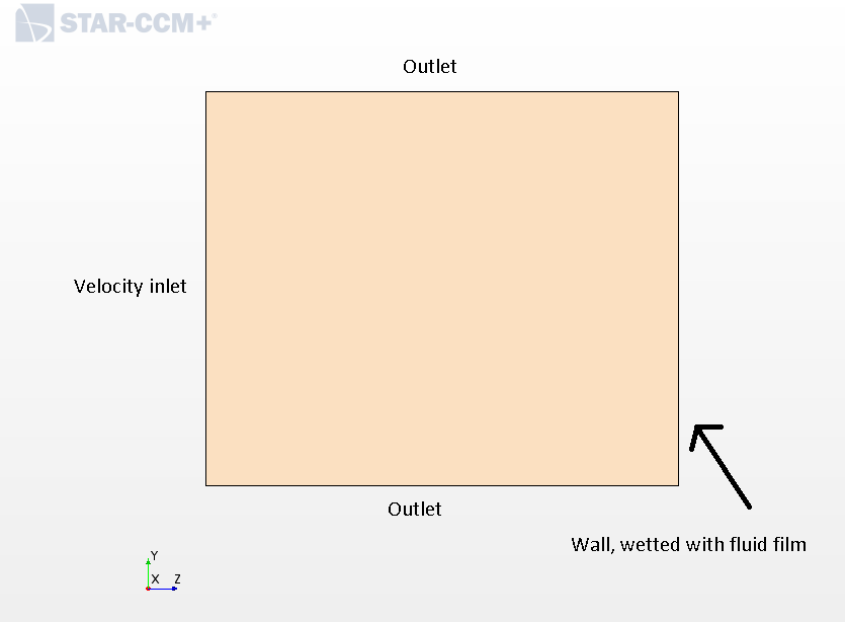

Figure 4.3: Boundary conditions of the model

On the inlet boundary, there is a particle injector at which all the parameters of the Lagrangian droplets are defined. Moreover, the velocity is prescribed at the inlet boundary, where the velocity magnitude was set equal to 0, since there is no freestream velocity in the actual experiment.

4.3.2 Space and time discretization

For the spatial discretization, the trimmed mesher of Star CCM+ was used. This means that the cells are hexahedra. Since there is a preferred flow direction in these simulations, a hexaherdal grid introduces less numerical diffusion than a polyhedral mesh [20]. Moreover, another benefit of the hexahedral mesh is the fact that there are less memory requirements than a corresponding polyhedral mesh, since one hexahedral cell has less neighbouring cells than a polyhedral cell [20].

The cell size of the mesh was determined based on the droplet diameter. Since the droplets are modelled as a Lagrangian phase, the cells cannot be much smaller than the droplets. This happens because the volume fraction of the Lagrangian phase should be relatively small when compared to the volume fraction of the continuous phase. As it is mentioned in [46], in Star CCM+ software, the volume fraction of the Lagrangian phase is automatically limited to 0.75. When a cell exceeds this value, then the software raises a warning so that the user is aware of this situation. Nevertheless, Senecal in his article [39] stated that in general, Lagrangian volume fractions that are greater than 0.1 should be avoided.

The timestep size is adjusted based on the maximum CFL number. More specifically, the simulation with the highest particle velocity had $u_d = 4.16\frac{m}{s}$ and the grid size was $\Delta x = 1.4mm$. Consequently, in order to have a CFL number less than unity, the timestep was set to $\Delta t = 2.0 \cdot 10^{-4}\ s$.

In this set of simulations, there was special treatment of the first cell that was adjacent to the wall. As it has been mentioned above, the wall where there is impingement is wetted with a liquid film of water. This is the reason why the fluid film model has been activated (see section 2.9). However, the fluid film model is valid only until the first cell height. If the liquid film grows thicker than the first cell, then the flow field is no longer calculated based on the fluid film solver. What happens though is that after the first cell height the liquid film takes the properties that are valid on the boundary of the first cell. This makes the Fluid Film model invalid on wall distances greater than the first cell height. For this reason, the prism layer mesher was used in the meshing process. In this way, the first cell height could be adjusted manually, so that it can accommodate the fluid film correctly, without having any dependence on the mesh size. More specifically, the Prism layer mesher was set to have only 1 layer, while the thickness of the layer is set according to the thickness of the fluid film, which is found on the following section.

For this reason, the prism layer mesher was used in the meshing process. In this way, the first cell height could be adjusted manually, so that it can accommodate the fluid film correctly, without having any dependence on the mesh size. More specifically, the prism layer mesher was set to have only 1 layer, while the thickness of the layer is set according to the thickness of the fluid film, which is found on the following section.

Fluid film was assigned with a maximum thickness. If the liquid film were to grow above this maximum value, then the solver automatically 'chops' the part which extends beyond the limit. Thus, it was decided to set as a maximum fluid film thickness equal to the height of the first cell. This decision was taken based on the fact that when the fluid film reaches the height of the first cell, above that it stops solving the flow field and it assigns the values that are valid on the height of the first cell. Thus, it is considered to give unreliable

results beyond the first cell.

The following figure shows the grid of the physical domain. This grid remained the same throughout all the validation simulations.

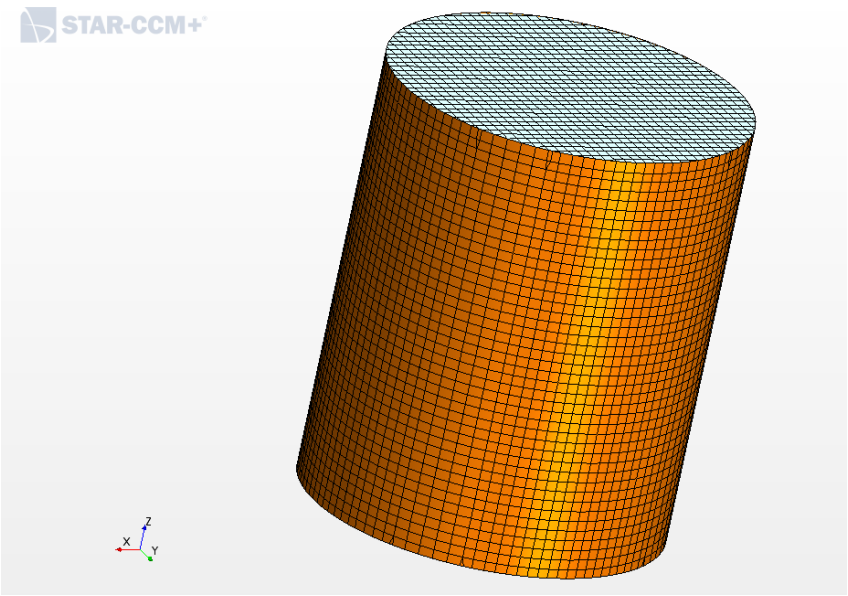

Figure 4.4: Mesh of the validation simulations

4.3.3 Set-up of the two-phase flow

In this section there is the explanation of the physical and numerical models and their implementation in Star CCM+ software. For the validation procedure, a Lagrangian multiphase simulation is used. Thus, an injector that shoots Lagrangian particles in the air domain is set up.

Injector: All the data that are related to the Lagrangian particles were provided in the reference paper [29]. In the *Injector* section of the simulation, the user can modify the parameters of the Lagrangian phase that are explained below:

- **Injector type:** The first parameter that is set in the injector entity is its type. In the current validation simulations, a *Point Injector* was used. This means that all the particles entered the domain from one specific point in space.
- **Flow rate specification:** In all the simulations of the validation model, the flow rate was measured in particles per second. For this reason, a Field Function was created, so that one particle is injected every 40 time-steps. Thus, the impingement test was conducted multiple times, confirming the repeatability of the simulation.
- **Particle size specification:** A constant diameter was selected, in accordance with the experimental procedure. More specifically, the droplet diameter of all the subsequent validation simulations is $D = 1.9\ mm$.

- **Particle impact velocity:** Changing the velocity of the particles was the only means of varying the Weber number. In the validation simulations, the range of impingement velocity was from $u_d = 1.32\frac{m}{s}$ up to $u_d = 4.16\frac{m}{s}$. More specifically, the following matrix shows the impact velocities of all the validation simulations.

Simulation	Velocity	We
1	1.32	50
2	2.28	150
3	2.32	155
4	2.35	160
5	2.39	165
6	2.43	170
7	3.22	300
8	3.72	400
9	4.16	500

Table 4.1: Test matrix of simulations

Physics modelling: In the Continua section, the physics setup of the simulation is defined. As far as the impingement wall is concerned, it is covered with a liquid film of water to make the simulation as close to the experiment as possible. Thus, the Fluid Film model was used. The initial thickness of the fluid film was $h_f = 1.14mm$. This thickness was taken from the experimental data of [29], and was extracted from the non-dimensional film thickness, that was:

$$\frac{h_f}{D} = 0.6 \Rightarrow h_f = 1.14mm. \tag{4.2}$$

Apart from initializing the fluid film, it is also necessary to specify its interaction with the droplets. For this purpose, a tool of the software called *multiphase interaction* was used. It is an interaction model, through which the user specifies that an impinging droplet on the fluid film and behave in accordance with an impingement model (in this specific case Bai-Gosman model).

The working fluid is air in this case. The turbulence model is realizable $k - \epsilon$, as it was found to yield consistent results while the simulation showed no signs of divergence.

The gravity model was chosen not to be activated. It was observed that when there is gravity in the model, the droplets were either accelerated or decelerated depending on the orientation of the injector. This acceleration posed a problem in tuning the impingement velocity correctly. There was no observed disadvantage from not activating the gravity in this set of simulations.

4.3.4 Simulated Cases

In total, there were 9 different validation simulations. As it was mentioned above in this chapter, the only difference between those simulations was the impact velocity of

the droplet. In order to automate the workflow the Design Manager tool of Star CCM+ was used. What this tool did was to assign the particle velocity as a parameter. After setting this parameter and its values, the software can run simulations in batches. Thus, it was possible to run 9 different simulations automatically, increasing the efficiency of the workflow. In Table 4.1 there are values of particle velocity that correspond to the 9 different simulated cases.

4.3.5 Results and discussion

The final stage of the validation process is the post-processing of the results and their presentation along with conclusions of this study. As a first result, it is the visualization of the experiment. On the following figure, one can view the cylinder that is the physical domain of the simulation. On the left side, there is the injector surface, where the particles are introduced inside the cylinder. On the right side of the cylinder, there is the wetted wall, where the droplets are impinging. In this specific picture, it can be seen that there are 3 particles simultaneously in the physical domain. As it was explained before, this behavior is desired, since the repeatability of the results can be checked if the test is conducted multiple times.

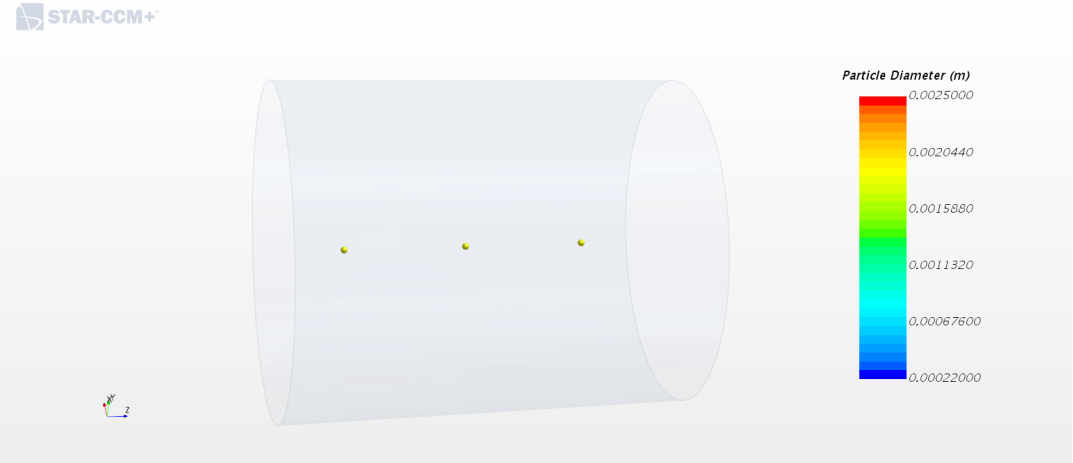

Figure 4.5: Visualization of the simulation

The outcome of the impingement was assessed visually as well as by checking the mass conservation. The visual assessment was done by using the Scenes post-processing tool of Star CCM+. More specifically, the particle diameter of all the droplets inside the domain was plotted and exported every 5 timesteps.

There were 2 distinct outcomes. If the droplet were below the splashing limit of the Bai-Gosman model, then it is spreading and its mass is added to the mass of the fluid film. Thus, when the droplet diameter scene is plotted, the user sees that the particle disappears upon the impact with the wall, as it becomes part of the liquid film.

The second possibility at this set of simulations is to have a droplet splashing. This event occurs when the Weber number is higher than the critical Weber number, as it is explained in paragraph 2.4. Upon the splashing event, the droplet disintegrates into

smaller particles that are ejected inside a conical volume [43]. Thus, splashing can be detected visually by the user, when smaller droplets appear after the impact. One such figure showing the splash of a droplet can be seen below:

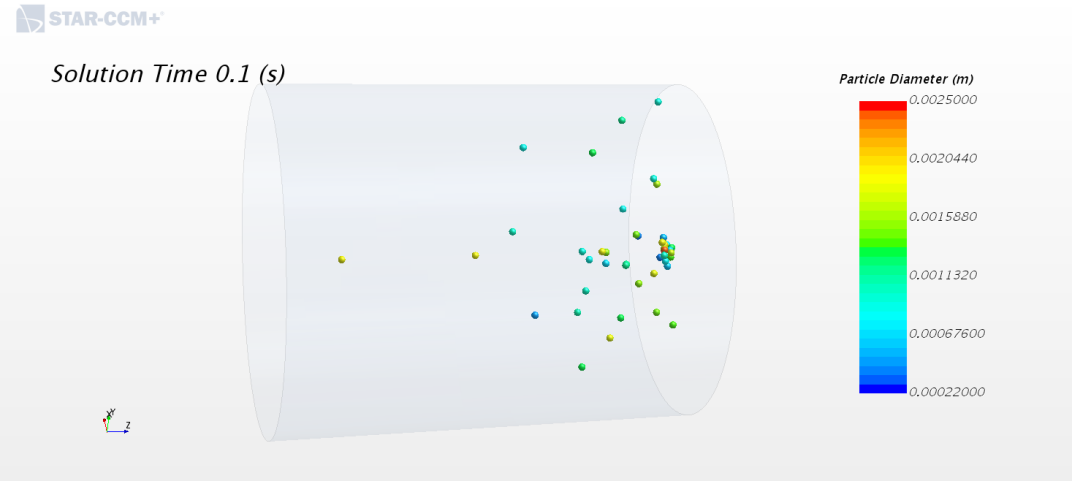

Figure 4.6: Visualization of splashing

After gathering all the simulation data, it is necessary to compare them with the corresponding experimental. In Figure 4.7, the horizontal axis is the non-dimensional fluid film thickness (S_f), while the vertical axis is the Weber number of the impinging particle.

The reader should observe in this figure that there are two horizontal lines corresponding to the limits of splashing and droplet spreading of the experimental procedure. More specifically, the limit of coalescence was found to be at $We = 154$, while the limit of splashing was found to be at $We = 205$. There was no further experimental data inside this Weber number zone that would help to narrow the limits between splashing and coalescence.

On the other hand, the Bai-Gosman model provides with a critical Weber number that sets a clear limit between spreading and splashing. In this specific set of simulations, We_c was found from (2.8) based on a Laplace number of $La = 127550$:

$$We_c = 1320 \cdot 127550^{-0.18} \Rightarrow We_c = 160. \tag{4.3}$$

The numerical results confirmed that there is agreement with the experimental data. More specifically, the simulation with We number equal to 160 was the last one where droplet spread was observed, while from the simulation with We number equal to 165 and above, all of the simulations depicted splashing behavior.

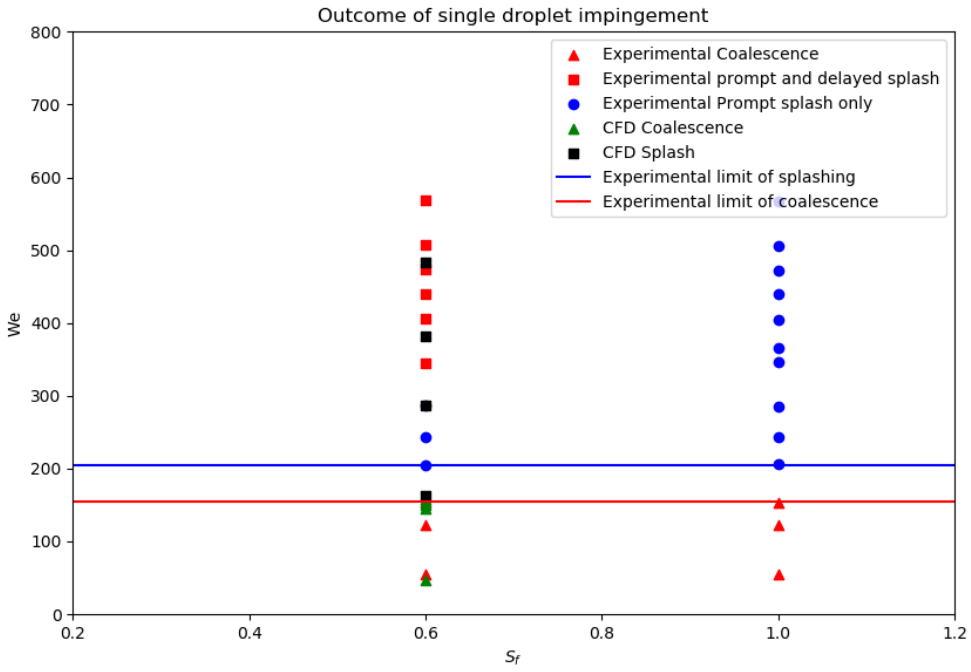

Figure 4.7: Comparison between experimental and numerical results

Chapter 5

Mass conservation simulations

5.1 Problem description

The goal of this part of the study is to investigate in the mass conservation of the liquid phase. In this type of simulations oil is injected inside a cylinder which has solid walls on its bottom and its side, while the top of the cylinder is open. One figurative way of describing this problem can be this: Initially, there is an empty cylindrical container. Then, at $t = 0$ there is a source of that injects oil from the top of the container. The mass conservation is monitored through the rate of increase of the interface between air and oil. The comparison of the rate of increase takes place based on 2 different methods that are described below. The first method is a simulation that was conducted with the use of Lagrangian multiphase model, while the second method is a theoretical linearly rising interface, where the oil flow rate is the same as that of the Lagrangian simulation.

5.2 Lagrangian multiphase flow

The first method is to inject Lagrangian particles inside the cylinder. At $t = 0$, there is a rather thin liquid film on the bottom of the cylinder (its initial thickness is equal to $1mm$) modelled as an Eulerian phase. This liquid film serves as an initialization of the "pool" that is formed. Then, the injector starts shedding particles towards the film of oil. The schematic representation of this is shown on Figure 5.1. It can be seen that the particles are injected with velocity equal to $10\frac{m}{s}$. As soon as a particle contacts the Eulerian phase, it is modelled to merge with the oil film and transform into Eulerian phase. In this way, the Eulerian phase of oil starts to form a rising pool of liquid.

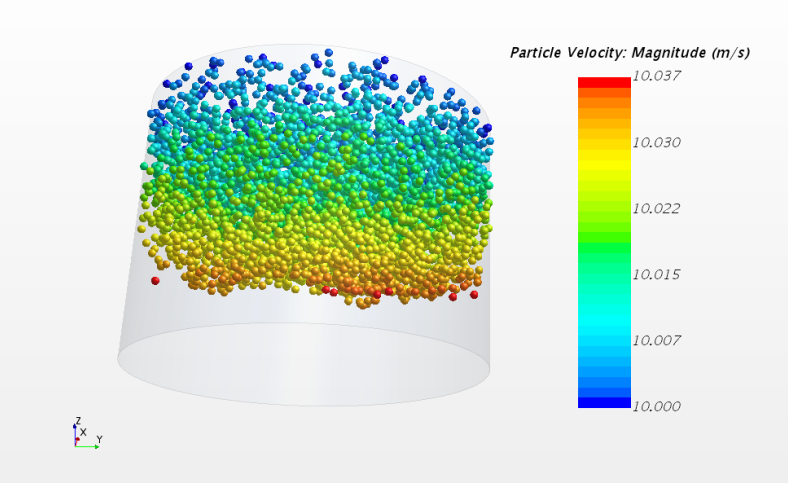

Figure 5.1: Mass conservation model with Lagrangian multiphase physics

The monitoring of the rise is conducted with measuring probes inside the cylinder. The probes are shown as a vertical black line on Figure 5.2. It is shown as a continuous line, since there are 100 probes on this direction. The probes measure the volume fraction of oil and its temporal evolution. As it can be seen on Figure 5.2, the interface between oil and air is not absolutely sharp. At first, at the lower part of the cylinder (non-blue) there is a significant amount of area that is covered in yellow color, meaning that the volume fraction is close to 0.7. The explanation of this phenomenon is that there are some trapped air bubbles inside the oil pool, of which the interface has not been captured. Thus, they are manifested as a decrease of the oil volume fraction. Moreover, the oil-air interface depicted in the middle of Figure 5.2 is not sharp either. Consequently, for the temporal evolution of the interface rise, it was decided that if the oil volume fraction is more than 0.5, then the fluid belongs to the pool of oil, otherwise it belongs to the Eulerian phase of air.

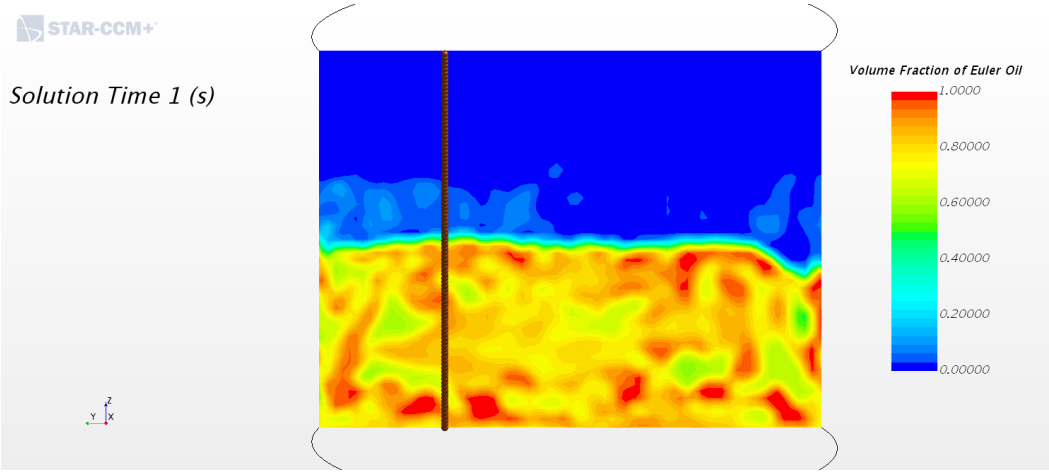

Figure 5.2: Oil volume fraction scene, Lagrangian model at $t = 1s$

As it can be seen on Figure 5.3, there is satisfactory agreement of the two methods. The

result of the simulation is to follow the trend of the linear increase of the interface. The error that occurs is measured to be on average 27%. The discrepancy between the linear approximation and the simulation can be attributed to the bubbles of air that are trapped during the simulation. Since not all of the volume is filled uniformly with oil during the simulation, it is logical that the interface is found to be higher than the corresponding linear interface.

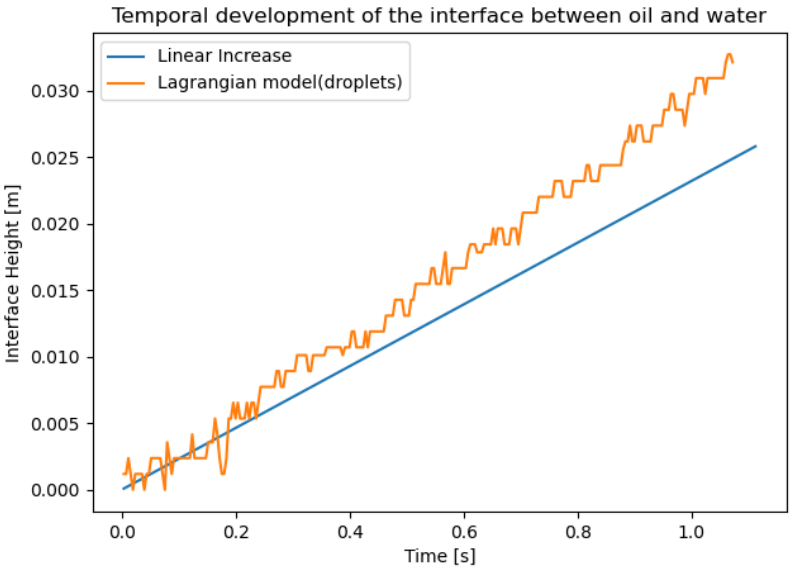

Figure 5.3: Temporal development of oil and air interface

Chapter 6

Spray heat transfer

Up until now, the focus of the study has been on the flow field of the spray. There has been a grid convergence study of the spray, as well as a validation of the Bai-Gosman model. However, none of the previous chapters refer to the topic of heat transfer, which is of great importance for DAF. Thus, at this part of the thesis, the subject of spray heat transfer is investigated on the geometry of a cylinder.

This section has the following structure: At first there is the presentation of the paper that is used as reference for the validation of the numerical model that is built. Furthermore, there is the explanation of the geometry and the boundary conditions of the problem. Afterwards, the heat transfer model that is implemented on Star CCM+ is presented. At the last part of this chapter, there are the results of the simulations and the conclusions that stem from the outcome of the simulations.

6.1 Problem description

The problem of spray heat transfer can be described as a rather complicated one. There is the creation of a liquid film when the wall is cold (below the Leidenfrost point). Moreover, there is the interaction between the spray and the film as well as the interaction of the wall and the liquid film. In a real world engine, the heat transfer between the oil spray and the piston becomes an even more complicated problem, since there is the reciprocating motion of the piston and the existing flow field of air inside the crankcase. Thus, there have been some simplifications regarding the approach of the problem of spray heat transfer. Those simplifications are discussed in the subsequent paragraphs, along with the development of the numerical model which describes the physics of impingement heat transfer.

6.2 Experimental reference data

During the literature research, two papers have been identified to be the most suitable for the purposes of this study: Mudawar and Valentine [30] and Rybicki and Mudawar

[35] describe the experiments that the authors conducted in order to calculate the heat transfer between a spray and a wall. These two studies were selected due to the proximity with the current study. At first, the droplet diameters of the experimental spray studies were within the range of diameters predicted by Venkatesh [54]. Even if the volumetric fluxes of the experiments were not inside the range of the previous study, they were in the same order of magnitude as of the DAF piston case. Thus, it was concluded that the aforementioned studies were suitable for the validation of the numerical simulations to follow.

6.3 CFD validation

Out of studies [30] and [35], the one or Mudawar and Valentine [30] is chosen because the working fluid of the experiments in [30] is water, a material that is well-documented and exists on the database of Star CCM+ software. On the other hand, Rybicki and Mudawar [35] used the more exotic coolant PF-5052 as working fluid which does not exist in the database of the simulation software.

The validation of the numerical model is conducted by utilizing the experimental data that is provided through the boiling curves of Figure 6.1.

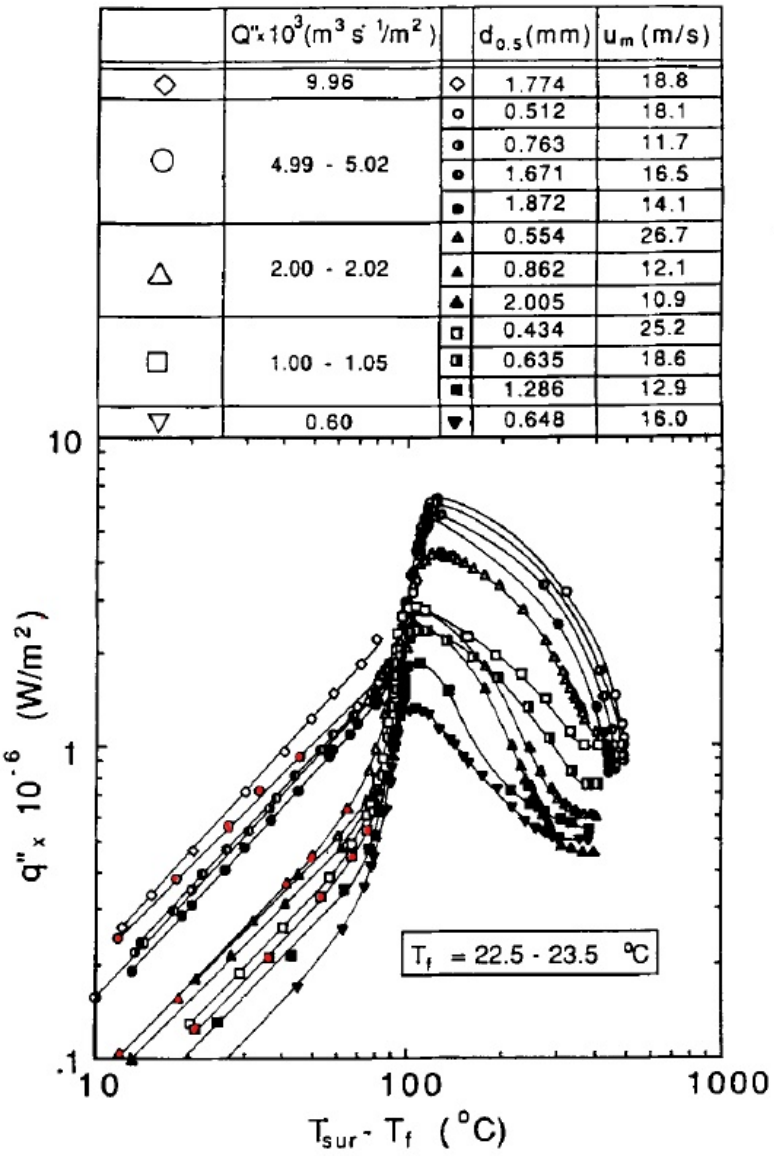

Figure 6.1: Experimental data of boiling curve, reprinted from [30]

6.3.1 Geometry and boundaries

The geometry of the simulation are close as possible to the experimental setup Figure 6.2. There are two domains, a solid domain made of copper on the bottom part of the figure (gray) and a fluid domain of air on top of it where the spraying process takes place. Both domains have the same diameter ($D_c = 0.004m$), corresponding to the $0.5cm^2$ impingement area of the experiments. The length of the air domain is equal to $10D_c$. Since there was no information relative to the injector-plate distance for the experiments, this length was decided based on the thought that the impingement area and the injector should be far enough such that they don't interact with each other. The following boundary conditions are chosen:

Solid domain:

- **Bottom boundary:** At the bottom of the cylinder, the boundary condition is a prescribed heat flux (units in $\left[\frac{W}{m^2}\right]$). It is essentially the numerical counterpart of the electrical heaters that exist in the experiment [30].
- **Side boundary:** The cylinder side is insulated in the simulation, as it is on the experiment. This is because it is desired not to have heat transfer other than the cooling of the spray impingement.
- **Top boundary:** At the top of the grey cylinder, there is conjugate heat transfer between the solid cylinder and the fluid film.

Fluid domain:

- **Bottom boundary:** At the bottom of the fluid cylinder, the boundary condition is a wall where there exists a fluid film, interacting with the solid wall on the side of heat transfer.
- **Side boundary:** The cylinder side is prescribed as a pressure outlet. It was chosen because the air and the Lagrangian particles need to escape from the simulation domain after the impingement.
- **Top boundary:** At the top of the orange cylinder, there is the injector of the Lagrangian phase. Moreover, for the continuous phase of air, it is set as pressure outlet. Although it is expected to act as an inlet of air due to the two-way coupling, the velocity and the flow rate of the air are not known, that is why it is chosen to set this boundary as a pressure outlet.

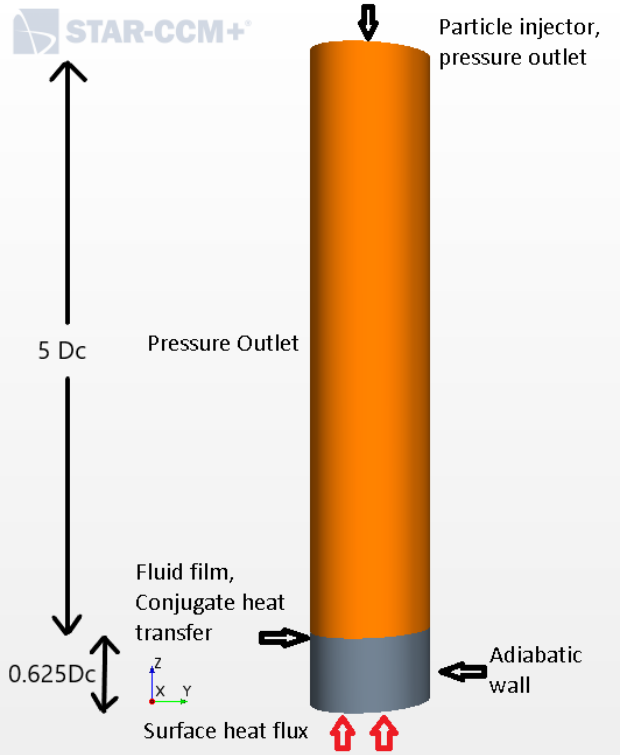

Figure 6.2: Geometrical setup of simulation

6.4 Space and time discretization

Hexahedral mesh is used throughout the thermal study of spray, an option called *trimmed mesher* in the software. The mesh that was created was almost uniform. There is no refinement at a specific area of the domain. Although there is one wall at the fluid mesh, it should be reminded that the wall is wetted with a fluid film. This fluid film can span only up to the first cell height, otherwise the model does not give reliable results. Thus, it is not possible to refine the mesh locally at the wall of the fluid domain. At the other two boundaries it is considered that there is no need for refinement, as they are not areas where further accuracy is required. For those reasons, it is considered that there is no need for local refinements at the current mesh.

The mesh size for this set of simulations was equal to:

$$\Delta x = 4 \cdot 10^{-4} m. \tag{6.1}$$

This was a choice that was based on the reasoning that was developed in section 4.3.2. Briefly explained, the cells of the mesh, should not be arbitrarily small, because in this way, the volume fraction of the Lagrangian phase increases. The consequence of Lagrangian phase's increased volume fraction in cells is the possible miscalculation of the forces that are exerted on a particle. On the other hand, the grid size should not be excessively large, on the ground of the accuracy of the results. Figure 6.3 shows a cross section of the air domain that passes from the centreline of the cylinder. The quantity that is depicted is

the volume fraction of the Lagrangian phase. It can be seen that the volume fraction is consistently below 0.1, which is the threshold that is suggested by [39]. The maximum Lagrangian volume fraction of the whole mesh was found to be equal to $4 \cdot 10^{-3}$. The result from this process is a mesh that has 33000 cells on the part of the air cylinder, while the solid cylinder contains 4600 cells due to its smaller size.

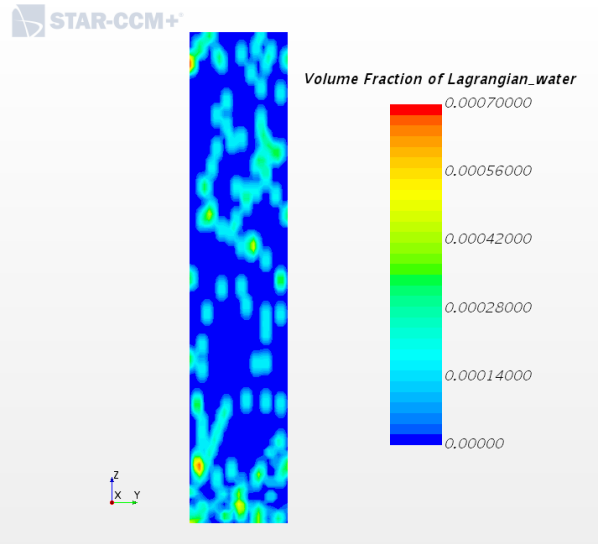

Figure 6.3: Lagrangian phase volume fraction scene

Since it is a transient simulation, it is necessary to determine the timestep. It was decided to do so according to the CFL number. The CFL number was kept below 1 at all times. More precisely, the maximum CFL number that was recorded was equal to 0.41. The same mesh parameters were used for the mesh of the solid domain, so that the contact between the two meshes is a conformal interface. The final meshes are shown in the following figure.

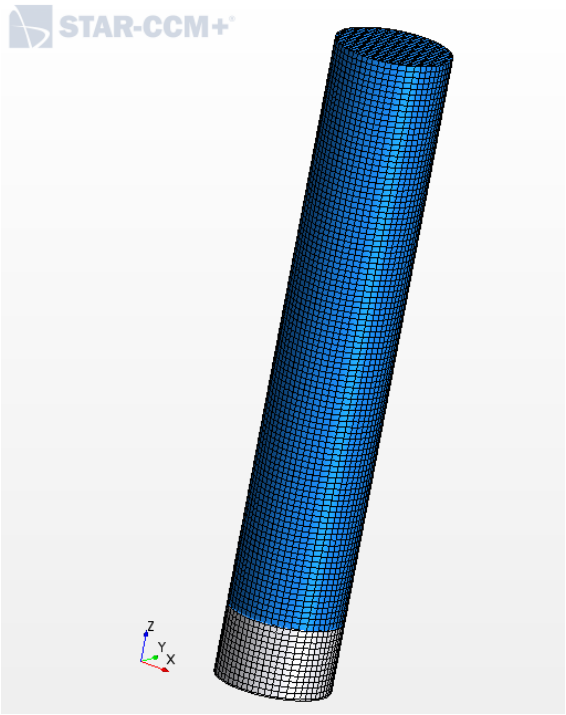

Figure 6.4: Mesh scene

6.5 Physics modelling

In this section there is the explanation of the Physics models and their implementation in Star CCM+ software.

The current type of simulations is RANS. Turbulence was modelled according to the Realizable $k-\epsilon$ formulation with two-layer all y^+ treatment. The latter model (two-layer all y^+ treatment) refers to the turbulence modelling in the vicinity of the wall. The y^+ non-dimensional distance of the first cell is calculated in the software. If y^+ is small (≈ 1) then the first cell is located in the viscous sublayer of the boundary layer [17] and the modelling is based on the assumption that the flow is laminar at that specific region [44]. On the contrary, if the centroid of the first cell has high y^+ (> 30), then the modelling is conducted based on the assumptions of the log-law region [17].

The working fluid of the simulation is air of constant density. The solver which was used was the segregated solver. This choice is made based on the recommendation of Star CCM+ documentation [41].

Gravity was taken into consideration, and it acted in the $-z$ direction, according to the reference frame of Figure 6.4. This means that gravity acts in the same direction as the particle injection.

For the validation procedure, a Lagrangian multiphase simulation is used. Thus, an injector that shoots Lagrangian particles in the air domain is set up. The properties of the Injector part are shown on the following matrix.

Parameter	Quantity	Units
Flow rate	$5.1 \cdot 10^{-5}$	$\frac{kg}{s}$
Particle size	$6.35 \cdot 10^{-4}$	m
Particle velocity	18.6	$\frac{m}{s}$

Table 6.1: Main properties of Injector part

6.5.1 Impingement Heat Transfer Model

When activating the Lagrangian Multiphase model, it is possible to model the heat transfer that takes place due to the impingement of the Lagrangian droplets on a wall. The modelling of impingement heat transfer that is implemented on Star CCM+ is presented by Birkhold et al. [10], while the model itself was developed based on the assumptions of Wruck [57].

At first, the impingement heat transfer model is based on the map that is shown in Figure 6.5. This map is developed in [24] and in essence determines the outcome of spray impingement, based on two parameters, namely T^* and K. T^* is the non-dimensional temperature of the wall and it is defined as:

$$T^* = \frac{T_w}{T_{boil}}. \tag{6.2}$$

The second parameter on which the impingement depends is called K:

$$K = Ca^{5/4} La^{3/4} \, . \tag{6.3}$$

This parameter is used to express the kinetic energy of the droplet impact. It can be concluded that the higher the impact energy, the higher number K grows.

In order for the Impingement Heat Transfer model to be valid, the wall needs to be hot. Quantitatively, this means that according to Figure 6.5, T^* needs to be greater than 1.1. In the case of a cold wall ($T^* < 1.1$), the software does not have specific formulation for the heat transfer. The physics is rather different during a cold wall impingement. One significant difference between the cold and hot wall impingement is the formation of fluid film. On a hot wall, liquid film cannot be formed on the wall. Instead, all of the droplets that impinge on the wall, either bounce back away from the wall, or they evaporate.

Another assumption of the impingement heat transfer model is the fact that the droplets and the solid wall are considered to be semi-infinite bodies [9].

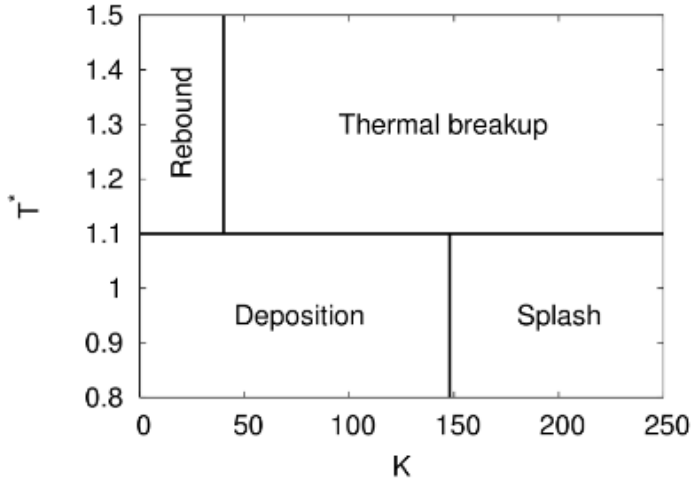

Figure 6.5: Spray interaction map, reprinted from [10]

More specifically, the algorithm that is implemented on Star CCM+ for the Impingement Heat Transfer model is described on the following paragraph:

The first parameter that is calculated on the context of this algorithm is called D_{eff}, or the effective diameter of the droplet. In essence, it is the diameter that should be taken into consideration on the calculations of the heat transfer. The effective diameter is given from the following formula:

$$D_{eff} = 0.61 D_0 We_i^{0.38}. \tag{6.4}$$

Knowing the effective diameter for heat transfer, the corresponding contact area of heat transfer is calculated:

$$A_{cont} = \pi \frac{D_{eff}^2}{4}. \tag{6.5}$$

Afterwards, the contact time of the heat transfer is calculated. This calculation is done based on the interaction map of Figure 6.5. Two regimes are recognised by the software: They are $K > 40$ and $K < 40$, confirming the fact that the model takes into consideration the hot wall case ($T^* > 1.1$). The two different contact times can be attributed to the fact that there are two different phenomena involved in the heat transfer of the droplets, namely the rebound and the thermal breakup. The contact times are given by the following formulas:

$$t_{cont} = \begin{cases} \frac{\pi}{4}\sqrt{\frac{\rho_d D_0^3}{\sigma}}, & K < 40 \\ \sqrt{\frac{\pi}{2}}\left(\frac{\rho_d D_0^5}{\sigma V_i^2}\right)^{0.25}, & K \geq 40 \end{cases} \tag{6.6}$$

The last parameter definitions for this specific model of heat transfer are the heat penetration coefficients of the wall and of the particle, b_w and b_d respectively. Those factors

indicate if the temperature at the interface of the two bodies is closer to the wall ($b_w > b_d$) or close to the droplet ($b_w < b_d$) [9]

$$b_w = \sqrt{\kappa_w \rho_w C_{p_w}} \qquad , \qquad b_d = \sqrt{\kappa_d \rho_d C_{p_d}}. \tag{6.7}$$

Having defined the all the necessary parameters, it is possible to introduce the formula that gives the heat transfer between a particle and the wall, due to impingement:

$$\dot{Q}_{wp} = A_{cont} \frac{2\sqrt{t_{cont}}}{\sqrt{\pi}\Delta t_P} \frac{b_w b_d}{b_w + b_d} \Big(T_w - T_{drop} \Big). \tag{6.8}$$

6.5.2 Effect of spray orientation

During the course of this set of simulations, a challenge occurred related to the orientation of the simulation. During the operation of the engine, the spray nozzle is found below the piston. This means that engine oil is injected upwards, against the force of gravity. Due to this configuration, several challenges occurred during the initial models that were built.

At the initial simulations, the gravity force was set to act against the direction of particle injection, as it is expected to happen in the engine environment. Consequently, the fluid film that is formed on the wall, is essentially "hanging" from the piston, as it can be seen for the configuration in Figure 6.6.

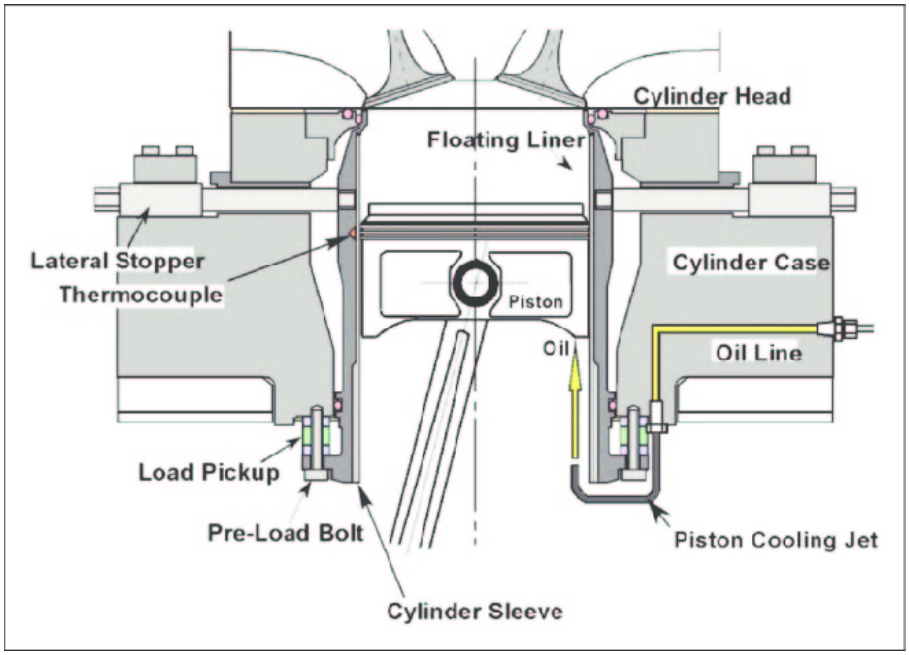

Figure 6.6: Demonstration of piston-oil jet configuration, reprinted from [25]

The fact that the fluid film is hanging from the wall poses a number of problems in the simulations. Those problems can be traced in the use of Fluid Film model. As it

is expected, the oil film's thickness would reach a steady state value, if the motion of the piston is not taken into consideration. Liquid droplets detach from the wall if the thickness grows larger than a certain point. However, in the implementation of Fluid Film model, the detachment of liquid oil can not be predicted. Instead, the observed behaviour of the fluid film in Star CCM+ is the following: An instability grows at a random point at the fluid film and a ligament starts to grow indefinitely. The expected behaviour is for droplets to detach from the main ligament as it grows. Thus, this non-physical behaviour of the fluid film renders the simulations which include a "hanging" fluid film unreliable.

Instead of recreating the actual condition of the engine, where the oil is sprayed upwards, another methodology is implemented. According to the findings of Rybicki and Mudawar [35], the heat flux which occurs from the impingement of droplets on a solid wall is independent of the orientation of the spray. The condition to have independence is not to have liquid accumulation on the wall. If a pool of liquid is formed during the spray process, then the heat flux is expected to be affected significantly. Thus, the observation of independence of orientation for the heat flux allows the change of spraying direction to a direction which would alleviate the aforementioned problems of upwards spraying. More specifically, the spray direction which is adopted for the set of the following simulations is along the direction of gravity, i.e. the spray emanates from the top of the cylinder, while the impact wall is found at the bottom of the cylinder as it can be seen at Figure 6.2.

The benefit of this configuration is the fact that the behaviour of the wall's liquid film is no longer erratic. The ligaments which pose a problem in the simulations no longer exist, and the maximum film thickness reaches reasonable values. Further analysis of the wall liquid film can be found at paragraph 6.6.1.

6.6 Results and discussion

In order to reproduce numerically the boiling curve of the validation paper, it was necessary to define the heat flux on the bottom boundary and measure what would be the resultant temperature on the surface where the spray impingement takes place. From the large volume of data that was provided from the boiling curves of Figure 6.1, the 15 points that are marked in red have been simulated, see Table 6.2.

Case #	$d_{0,5}$ (mm)	u_e (m/s)	T_w ($^\circ C$)	$Q^{''}$ ($\cdot 10^{-3}\, m^3 s^{-1}/m^2$)
1	0.635	18.6	43.5	1.02
2	0.635	18.6	58	1.02
3	0.635	18.6	74	1.02
4	0.635	18.6	91	1.02
5	0.635	18.6	96	1.02
6	0.512	18.1	34	5.0
7	0.512	18.1	41	5.0
8	0.512	18.1	50	5.0
9	0.512	18.1	55	5.0
10	0.512	18.1	69	5.0
11	0.554	26.7	35	2.01
12	0.554	26.7	42	2.01
13	0.554	26.7	62.5	2.01
14	0.554	26.7	71	2.01
15	0.554	26.7	84	2.01

Table 6.2: Parameters of simulated cases

The choice of the points is done carefully, taking into consideration the physics that governs various regions of the boiling curves. It is decided that the points which are more relevant to the current study are found on the left-most part of the boiling curves. This part is the called the single phase regime [30]. It is called this way because it is the only region where water is in liquid phase during the experiment. On the rest of the regimes, such as nucleate boiling or film boiling, there is the involvement of water in gas phase, either in the form of bubbles (nucleate boiling), or in the form of vapour film (film boiling). In the current study, the working fluid of interest (engine oil) is constantly at a temperature below its boiling point, thus the physics governing the heat transfer remains the same as that of the validation experiments.

Figure 6.7 depicts one of the key results of the simulation, which is the temperature distribution of the solid cylinder. At first sight, it can be seen that the temperature inside the cylinder drops linearly as we move from the heated boundary towards the spray cooled surface. This is an expected result which is in agreement with the findings of [30].

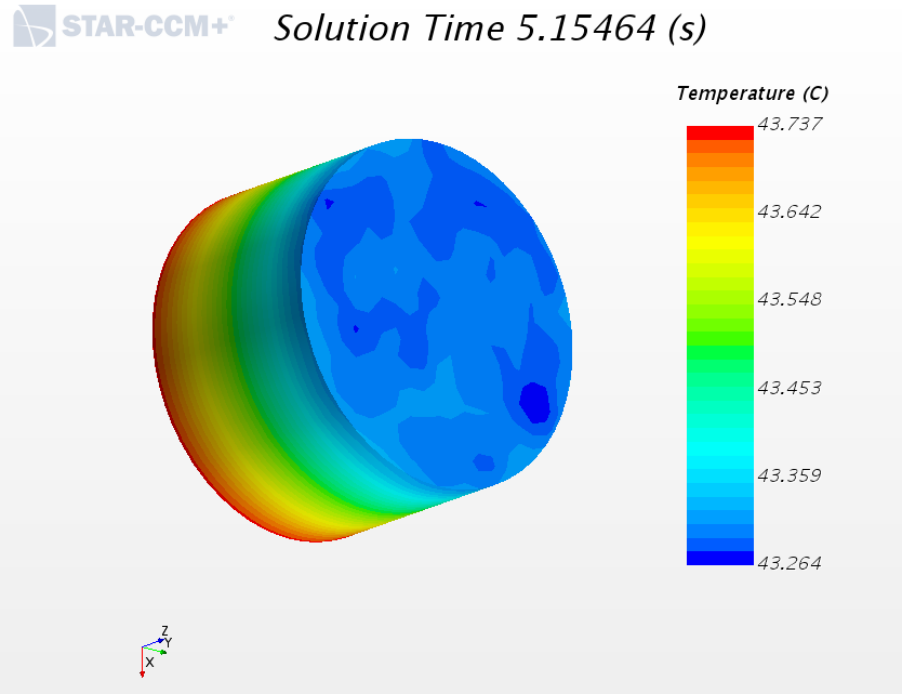

Figure 6.7: Temperature profile of solid cylinder, case 1

Apart from the quantitative presentation of the temperature profile, it it necessary to quantify the results. On Figure 6.8 there is the temporal development of the average temperature at the wall where impingement takes place. Since the wall heat flux has a constant value, the experiment is validated by observing the resultant wall temperature. It is clear that the convergence of the wall temperature is highly dependent on the initial conditions. If the user imposes initial conditions that are close to the steady-state result, then the simulation can converge quickly. At this point, it should be mentioned that the wall temperature converges to a steady state after $t \approx 0.1s$. The simulation ran for a longer period of physical time in order to ensure the stability of the solution, meaning that no irregular behaviour shall appear after the seemingly converged solution.

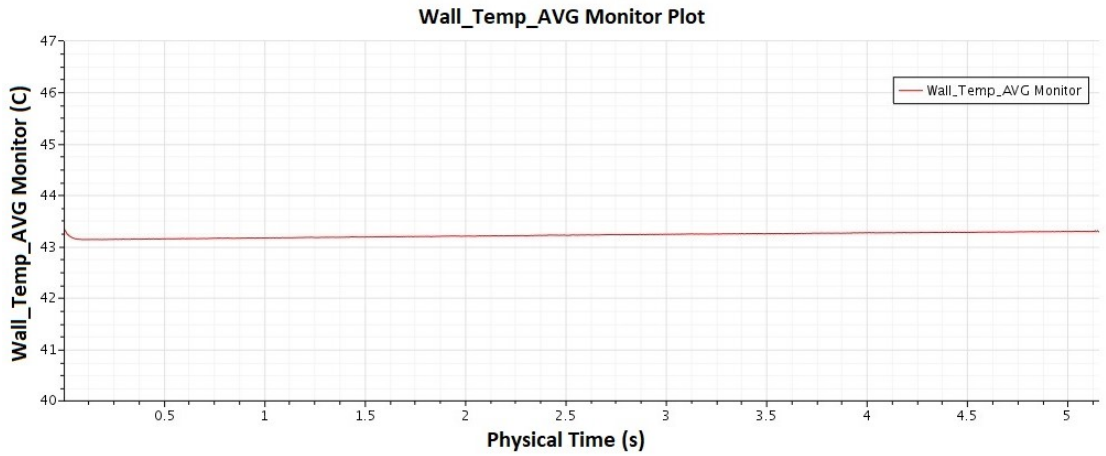

Figure 6.8: Temperature development at the cooled wall, case 1

Another criterion for the convergence of the solution is the heat flux from the boundary of the impingement wall. While the instantaneous heat flux on the bottom of the cylinder is constant and is set as a boundary condition, the instantaneous heat flux on the boundary of impingement is dependent on the instantaneous heat transfer among the droplets, the fluid film and the solid wall. This fluctuating behaviour can be seen on Figure 6.9. The range of fluctuations is from $\dot{Q}_{wp} = 32000\frac{W}{m^2}$ up to $\dot{Q}_{wp} = 38000\frac{W}{m^2}$. Another observation that can be made on this graph is that the fluctuations are consistently around an average value. The average of the data of wall heat flux is $\dot{Q}_{wp} = 34700\frac{W}{m^2}$. At the same time, the wall heat flux that is set at the bottom boundary is equal to $\dot{Q}_{wp} = 35200\frac{W}{m^2}$. This means that the simulation has not converged analytically to the input value of the heater, but it has converged within accuracy of 1.4%.

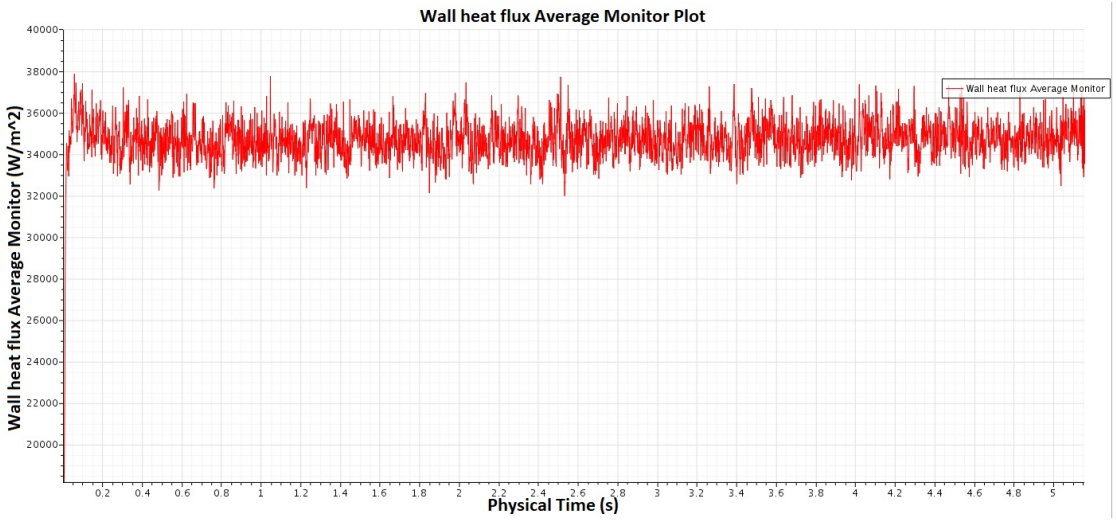

Figure 6.9: Wall heat flux temporal development, case 1

Parameter	Quantity	Units
Bottom heater input	35200	$\frac{W}{m^2}$
Impingement wall heat flux (average)	34700	$\frac{W}{m^2}$
Min wall heat flux	32000	$\frac{W}{m^2}$
Max wall heat flux	38000	$\frac{W}{m^2}$

Table 6.3: Output of simulation's heat fluxes, case 1

As far as the qualitative aspect of the wall heat transfer of particles, Figure 6.10 can provide with some information. To begin with, it can be noticed that at the side of the cylinder, the heat flux is analytically 0, which is in accordance with the adiabatic boundary condition that is chosen for this simulation. On to the wall where particle impingement takes place, the heat flux is varying. It can be seen that there are numerous "islands", where there is a spike of the heat flux, and others where heat flux is lower than the average value. This can be explained if the physics of the problem are taken into consideration. In the close vicinity of impingement of a droplet, the instantaneous heat flux is expected to be significantly higher than a corresponding area where there is no impingement. This behaviour of locally enhanced heat flux on the vicinity of the impingement is also supported by the fact that the fluid film is relatively shallow (compared to the diameter of the droplets), thus the heat transfer is expected to be different locally.

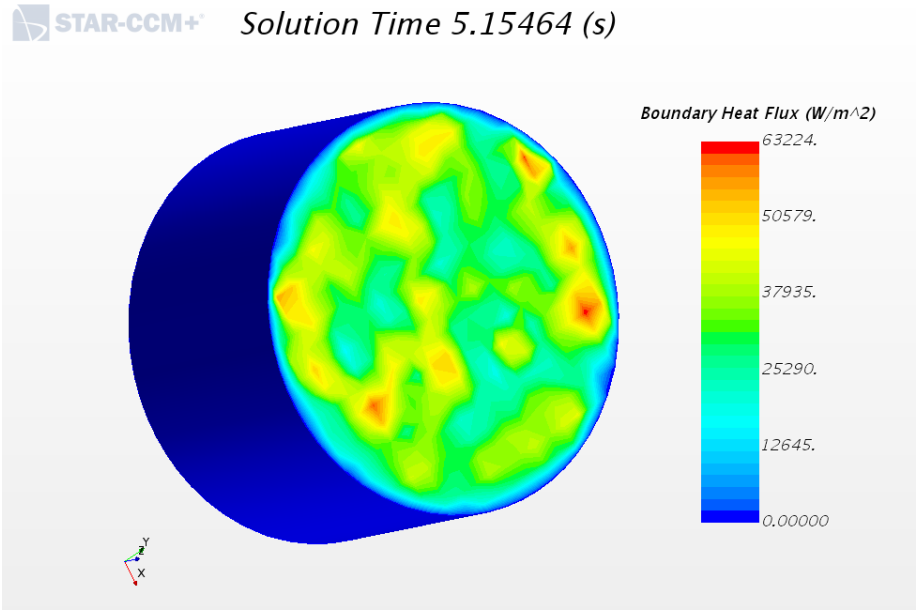

Figure 6.10: Wall heat flux scene, case 1

Comparison between the impingement heat transfer model and the model of fluid film: On the context of comparing the two heat transfer approaches that the software uses, a model is built to utilize the impingement heat transfer model. It should be mentioned that the fluid film model is not used in the simulation of impingement

heat transfer, due to lack of compatibility between these two models. The comparison between the two models can be seen on Figure 6.11. The comparison refers to a case which belongs to the curve described by squares in Figure 6.1. More specifically, it corresponds to the second from left case where the wall heat flux is equal to $q'' = 205000 W/m^2$, while the temperature difference between the wall and the water is equal to $58°C$. It can be seen that on Figure 6.11 there are discrepancies among the three cases that are compared. The lowest curve, (in green color) presents the result of the methodology that is described in paragraph 6.3.1. This means that the droplets of water impinge on a fluid film that is attached to the wall. The average resultant heat transfer is 70% lower than the experimental one.

It should be stated that information related to the modelling of droplet impingement heat transfer on a fluid film is rather scarce for Star CCM+ software. Thus, the root cause for the observed discrepancies between the experimental and numerical results is yet to be found.

The resultant heat flux of the second numerical method that is used can be seen as the red curve in middle curve of Figure 6.11. The methodology that is used during this simulation is explained in paragraph 6.5.1. The heat transfer modelling that is described in this paragraph cannot be used in conjunction with the fluid film model due to the physics of the model. More specifically, the range of wall temperatures where this model is valid is $\frac{T_w}{T_b oil} > 1.1$. This means that the wall is supposed to be hot on the context of this model. However, during nominal operation of the DAF engines, the wall of the piston is not hot. Although the model described in 6.5.1 is suitable for a temperature range different from that of DAF engines, there is great potential in this model for a future study. The implementation of this model in Star CCM+ is customizable to a great extent. As a consequence, in a future study the user can implement different models of impingement heat transfer. More specifically, it is possible to cancel the effect of the equations in section 6.5.1 and apply models that can be found in the open literature. One suggestion that can be possibly applied is found in the paper of Mudawar [30]. The correlation that is found to be suitable for the temperature range of natural convection is:

$$Nu_{0.5} = 2.569\, Re_{0.5}^{0.78}\, Pr^{0.56} \tag{6.9}$$

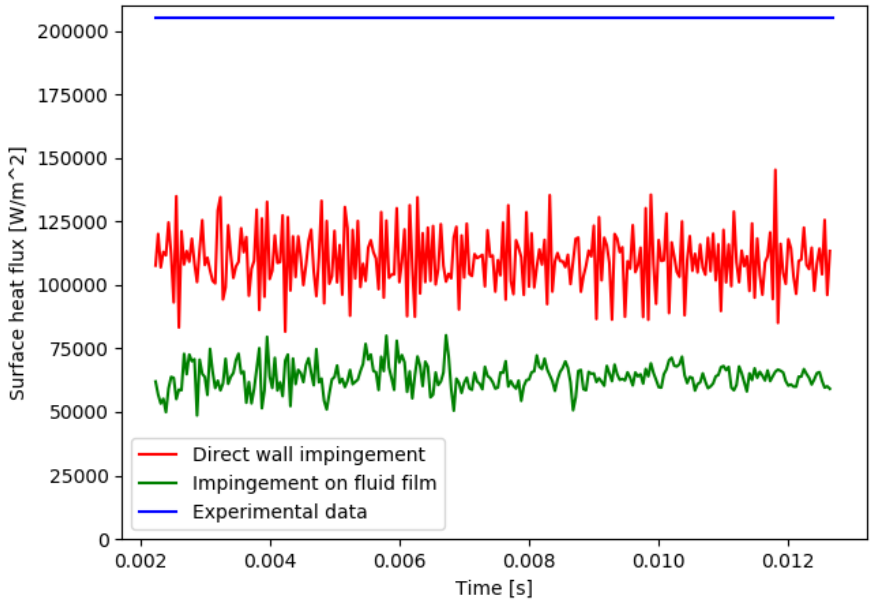

Figure 6.11: Heat flux comparison

Comparison between Fluid Film heat transfer model and experimental results: For the purpose of validating the numerical model which includes wall heat transfer via fluid film, a number of test runs are conducted. The runs can be seen on Figure 6.1 as red dots. Those experiments are chosen because they are in close proximity with the condition of the actual spray of the DAF engines. This similarity is in terms of the mass flow rate of the working fluid, the droplet diameter distribution as well as the wall temperature. On Figure 6.12 there is the presentation of the resultant wall heat flux of the numerical model, compared with the heat flux of the experimental process. At first sight, it can be seen that there is satisfactory agreement between the two methods as far as the slope of the curves is concerned. Nevertheless, there is rather constant offset of the CFD resultant heat flux from the experimental results. To be more specific, on average the CFD wall heat flux is 70% lower than the experimental one. The root cause for the observed discrepancies between the experimental and numerical results is yet to be found. Furthermore, it can be observed that on the red curve of the experimental results, the right-most point starts to diverge from the linear behaviour that the rest of the points exhibit. It is believed that this occurs due to the relatively high wall temperature. At $96°C$, the wall approaches the boiling point of the working fluid (water). It means that this particular point is close to the transition from the natural convection regime and the nucleate boiling regime of heat transfer.

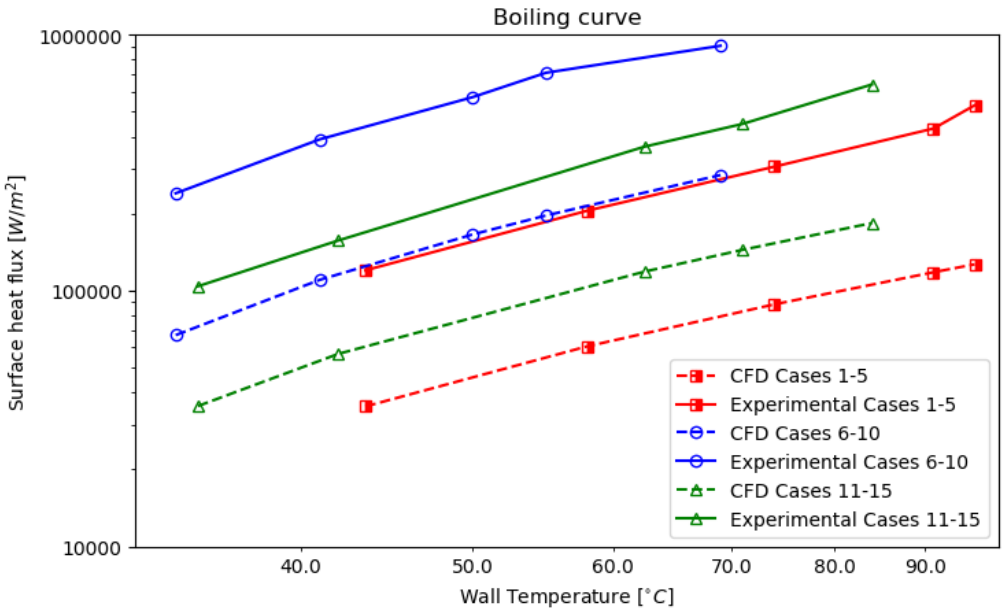

Figure 6.12: Boiling curves CFD plot

To demonstrate the constant discrepancy between the numerical model and the experiment, there is Figure 6.13. It can be seen that when the wall heat flux of the simulation increases by 70%, the experimental and the numerical results are in rather satisfactory agreement.

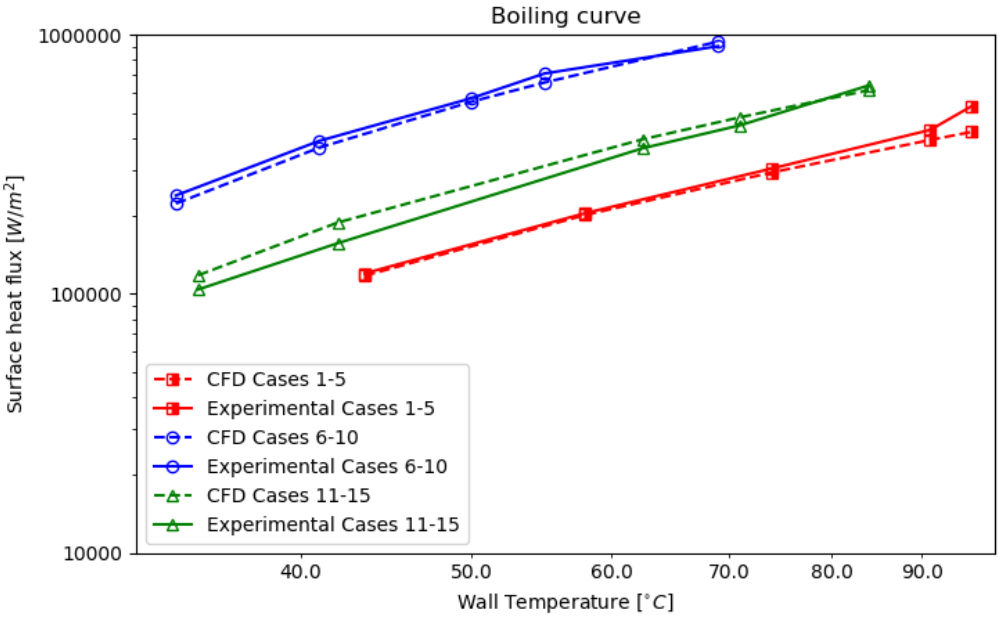

Figure 6.13: Boiling curves CFD plot, adjusted by 70%

6.6.1 Fluid film

The final parameter that is measured during this set of simulations is the fluid film on the wall. A visualization of the fluid film thickness is shown on Figure 6.14 for case 1. There are some patterns that can be discussed on that photo.

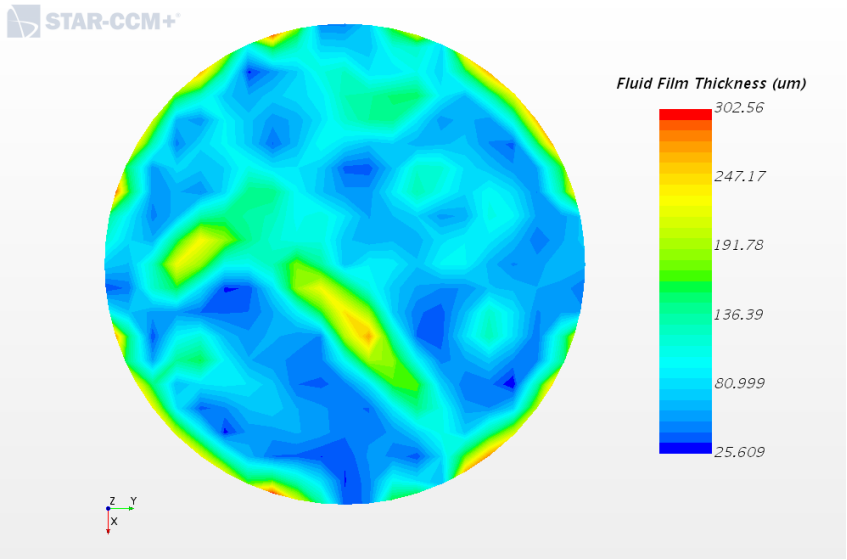

Figure 6.14: Fluid film thickness, case 1

At first, it can be seen that the fluid film is certainly not uniform, but there is a number of peaks and valleys. This behaviour can be explained if the impingement of the droplets are taken into consideration. When a droplet impinges on the fluid film, it is expected to create a crater, where liquid is displaced.

This set of simulations is transient. It means that the initial conditions need to be defined before running the simulation. It is decided that a reasonable initial thickness for the fluid film can be equal to $200\mu m$. The initial thickness of the fluid film does not affect the results at later stages of the simulation. After a number of times that this simulation ran, it was decided that an initial thickness of $200\mu m$ would aid to reach steady state more swiftly. The initial thickness can be seen on the red curve of Figure 6.15, at $t = 0$.

After a very short amount of time (approximately $t = 0.1$), the average fluid film thickness reduces to $90\mu m$. It should be mentioned that it is a spatial averaged fluid film. After this initial reduction the average fluid film thickness reaches a steady state at this value of thickness, although there are perceptible oscillations that have amplitude equal to $5\mu m$.

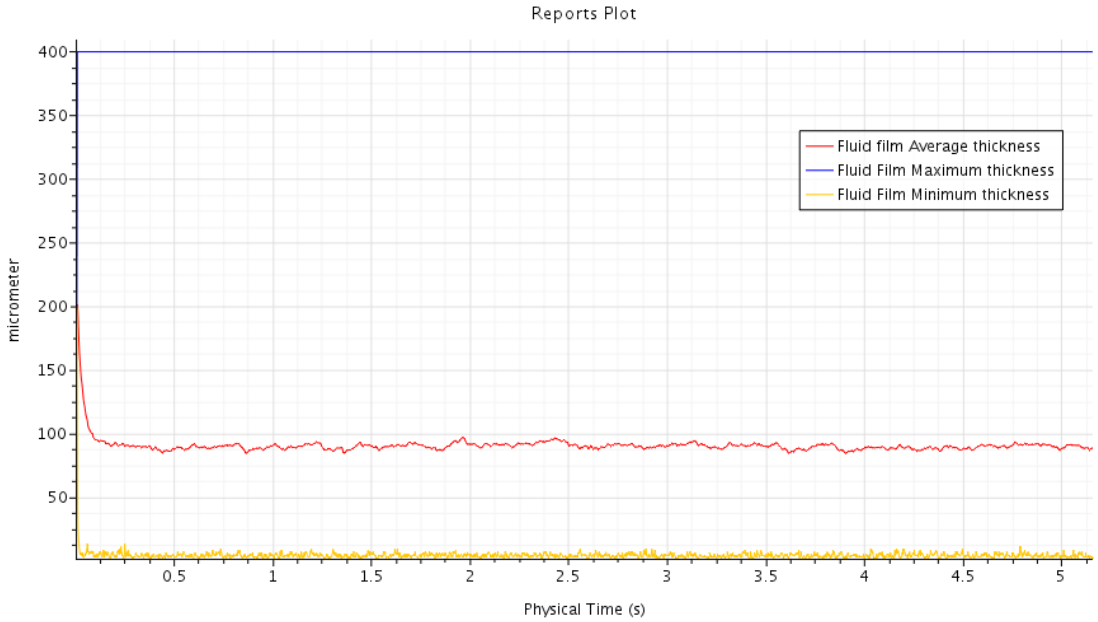

Figure 6.15: Fluid film temporal development

Chapter 7

Conclusions

The broader topic of this thesis is the simulation of piston cooling in internal combustion engines. This general topic can be divided into 4 different sub-topics, listed below.

- Oil jet evolution and breakup
- Jet impingement cooling
- Spray cooling
- Gallery cooling

The current study focuses on the third sub-problem, spray cooling, as the first two topics were thoroughly investigated during two earlier thesis projects of DAF. The sub-topic of spray cooling is on its own a rather broad subject, so it is also split into 3 different sub-projects explained below.

7.1 Grid sensitivity analysis

In all of the simulations that were conducted, the RANS modelling was used for approaching turbulence. For the multiphase part of the simulations, the Lagrangian formulation is used. During the first phase of the thesis, there was a grid sensitivity analysis. Due to the Lagrangian approach of this multiphase flow, this proved to be a non-trivial task. Following the common sense, one would expect that the further the mesh is refined, the higher quality would be yielded for the solution. However, this is not the case in a simulation with Lagrangian multiphase flow. It was found that the diameter of the droplets played a rather important role for the choice of the grid size. More specifically, when there was refinement beyond a certain point, the simulations proved to yield low quality results. The root cause behind the low quality results of the simulations with very fine meshes lies on the fact that the Lagrangian droplets occupy a large part of the cell's volume. When

this happens, the Lagrangian droplets can rapidly bring up to their speed the continuous phase, resulting in a drag force that is significantly underestimated. These observations were in accordance with the findings of a number of papers [5, 39]. Along with the issue of drag calculation, there are reports [2, 5, 39, 46], stating that divergence of the simulation is highly likely when the Lagrangian droplets are large compared to the cell size, however this behaviour was not observed during the simulations.

7.2 Validation of impingement model

The second phase of the thesis was related to the validation of the impingement model that is implemented on Star CCM+. The most suitable paper that was found for this case was published by Motzkus [29]. In this paper, the liquid of the droplets was water. Contrarily to the paper, the liquid that is used for the process of piston cooling is engine oil, however the literature on the topic of droplet impingement of engine oil is rather scarce.

A test case simulation was built for the validation of the impingement model of Star CCM+. The simulation that was built yielded results in excellent agreement with those of the experimental process. In the aforementioned paper, the authors gave a range of uncertainty between the transition from droplet deposition to droplet splashing phenomenon. The Bai-Gosman model that is implemented on Star CCM+ accurately predicted this transition within the same range of droplet We number. Each droplet impact test was conducted multiple times in each simulation. Thus, the repeatability of the results is an indication of the robustness of the model that was built.

7.3 Impingement heat transfer

The last chapter of the thesis was dedicated to the heat transfer that takes place during the process of spray impingement. A validation procedure took place for the purpose of investigating the impingement heat transfer between a hot wall and liquid droplets. The paper that was chosen for the purpose of validation was published by Mudawar [30]. It was chosen due to the similarities that it bore with a number of parameters of the DAF piston cooling problem. Some of these parameters are: Droplet size, spray volumetric flux and wall temperature.

Although all of the aforementioned parameters of the experiment are in the same order of magnitude as the DAF piston cooling problem, the working fluid is not the same. In the experiment, water is used for the creation of spray, while in the DAF pistons, the working fluid is engine oil. Given the scarcity of literature on the topic of engine oil impingement, this was considered as a rather suitable alternative. Two impingement heat transfer models of Star CCM+ were tested against the experimental results. The first model that is tested is a conjugate heat transfer model. There was an accurate representation of the experimental configuration, since in the simulations there is the inclusion of the fluid film that is formed during the spraying process. Furthermore, there is the modelling of the heat transfer between the droplets and the fluid film, as well as the conjugate heat transfer between the fluid film and the wall, which is the desired result. The outcome

of the validation simulations had some positive aspects, as well as some negative ones. In the variety of experimental test cases that were simulated, it can be observed that there is high precision but low accuracy. In all of the 15 validation simulations that were conducted, there was a consistent underestimation of the experimental wall heat transfer by 70%. This consistency suggests that there might be some systematic root cause that makes the model under-predict the wall heat flux.

The second model that was implemented, is called Impingement Heat Transfer model. This model was not used as extensively as the previous one. Although it was found to be applicable on different regimes of impingement heat transfer, there is great potential for further investigation of this model, since it can be customised to replicate the desired conditions of impingement.

Chapter 8

Future work

There is some significant scope on the general topic of piston cooling. This study has focused on the spray cooling part of the general problem, however there are some aspects that need to be investigated further, while other aspects of piston cooling are to be studied from the beginning.

The current study can be improved in a number of ways. Some of those are described:

- One way that the future student can improve the current study is the investigation of the actual geometry of a DAF piston. In the current study, there is a number of models, regarding the droplet impingement behaviour and the heat transfer that takes place. However, all of those models have been created on a cylindrical domain that bears similarities with the actual cylinder, however it is far from being identical. Thus, it would be rather interesting to investigate the pistons of the DAF engines as compelling conclusions and observations are expected to arise from such a study.
- Another area where there can be improvement is the heat transfer modelling. In the current study, there is the comparison of the existing model of Star CCM+ for impingement heat transfer between the droplets and the wall. However, on the latest update of the software, the user is able to customize the model and use their own field functions. This fact gives the user significant freedom to validate numerically various experimental papers that are found on the open literature.
- Moreover, another topic that the future student may further explore in this thesis is a number of parametric studies. Through changing some of the dominant parameters, the user is expected to yield some interesting results. For example, by changing the viscosity of the liquid or the temperature of the wall and the working fluid is likely to improve the understanding of the complex physics behind the impingement phenomenon.

Apart from the improvements of the current thesis, there are some unexplored territories of the general piston cooling problem. One of these can be considered the gallery cooling

topic. In previous theses, the topics of jet cooling and jet break-up have been thoroughly investigated, while on the current project, the spray cooling is studied. The remainder chapter that is rather significant to the broader topic is the analysis of gallery cooling. Since the only type of pistons that DAF currently uses are cooled through a gallery, the reader can understand the importance of such a project. The sloshing motion that the engine oil performs inside the gallery is offered for a number of numerical experiments. Furthermore sloshing motion is a field that has been thoroughly studied [21, 18, 19, 13], so the future student is expected to have a solid topic of study.

As a closing remark, the subject of the current thesis has the element of novelty for DAF. In previous theses the topic of piston cooling was studied from the oil jet point of view, while in the current thesis the topic is studied from the oil spray point of view. Thus, this study gave the company insight into a wider window of operation for the cooling of the internal combustion engines. Given the cost and the difficulties of implementation that a possible experimental study would pose to the company, the numerical study has been a very effective way of expanding the knowledge of DAF.

References

[1] Muhammad Aamir, Liao Qiang, Zhu Xun, Hong Wang, and Ramzan Ullah. Study on ultra-fast cooling behaviors of water spray cooled stainless steel plates. *Experimental Heat Transfer*, 29(3):299–321, 2016.

[2] John Abraham. What is adequate resolution in the numerical computations of transient jets? *SAE transactions*, pages 141–155, 1997.

[3] Jaber Almedeij. Drag coefficient of flow around a sphere: Matching asymptotically the wide trend. *Powder Technology*, 186(3):218–223, 2008.

[4] John David Anderson Jr. *Fundamentals of aerodynamics*. Tata McGraw-Hill Education, 2010.

[5] SV Apte, K Mahesh, and T Lundgren. A eulerlan-lagrangian model to simulate two-phase/particulate flows. Technical report, MINNESOTA UNIV MINNEAPOLIS, 2003.

[6] Chengxin Bai. *Modelling of spray impingement processes*. PhD thesis, Imperial College London, 1996.

[7] CX Bai, H Rusche, and AD Gosman. Modeling of gasoline spray impingement. *Atomization and Sprays*, 12(1-3), 2002.

[8] Cx K Batchelor and GK Batchelor. *An introduction to fluid dynamics*. Cambridge university press, 2000.

[9] Theodore L Bergman, Frank P Incropera, David P DeWitt, and Adrienne S Lavine. *Fundamentals of heat and mass transfer*. John Wiley & Sons, 2011.

[10] Felix Birkhold, Ulrich Meingast, Peter Wassermann, and Olaf Deutschmann. Analysis of the injection of urea-water-solution for automotive scr denox-systems: modeling of two-phase flow and spray/wall-interaction. *SAE Transactions*, pages 252–262, 2006.

[11] J Boussinesq. Theorie de l'ecoulement tourbillant. *Mem. Acad. Sci.*, 23:46, 1877.

[12] Halil Çelik. Cfd analysis of piston cooling jets. Master's thesis, TU Delft, 2018.

[13] Bang-Fuh Chen and Roger Nokes. Time-independent finite difference analysis of fully non-linear and viscous fluid sloshing in a rectangular tank. *Journal of Computational Physics*, 209(1):47–81, 2005.

[14] Mouldi Chrigui. *Eulerian-Lagrangian approach for modeling and simulations of turbulent reactive multi-phase flows under gas turbine combustor conditions.* PhD thesis, Technische Universität Darmstadt, 2005.

[15] G.E Cossali, M Marengo, and M Santini. Thermally induced secondary drop atomisation by single drop impact onto heated surfaces. *International Journal of Heat and Fluid Flow*, 29(1):167–177, 2008.

[16] Clayton T. Crowe, John D Schwarzkopf, Martin Sommerfeld, and Yutaka Tsuji. *Multiphase flows with droplets and particles.* CRC press, 2011.

[17] Dr. Steven Hulshoff Dr. S. Hickel. Lecture notes cfd 3, large eddy simulation, 2017.

[18] Odd Magnus Faltinsen and Alexander N Timokha. *Sloshing*, volume 577. Cambridge university press Cambridge, 2009.

[19] Florian Fleissner, Alexandra Lehnart, and Peter Eberhard. Dynamic simulation of sloshing fluid and granular cargo in transport vehicles. *Vehicle system dynamics*, 48(1):3–15, 2010.

[20] Dr. S. Hickel. Lecture notes of cfd for aerospace engineers, 2017.

[21] Raouf A Ibrahim. *Liquid sloshing dynamics: theory and applications.* Cambridge University Press, 2005.

[22] Mohamad Izadi, Seyed Vahid Hosseini, Seyed Shahab Alaviyoun, and Seyed Mostafa Agha Mirsalim. Experimental and numerical analysis of the piston cooling jets performance. In *Engineering Systems Design and Analysis*, volume 49170, pages 287–293, 2010.

[23] Nikolaos D. Katopodes. Finite-difference methods for advection. In Nikolaos D. Katopodes, editor, *Free-Surface Flow*, pages 118 – 197. Butterworth-Heinemann, 2019.

[24] Dominik Kuhnke. *Modelling of spray impingement processes.* Technischen Universitat Darmstadt, 2004.

[25] Kai Liao, Yang Liu, Dallwoo Kim, Paulo Urzua, and Tian Tian. Practical challenges in determining piston ring friction. *Proceedings of the Institution of Mechanical Engineers, Part J: Journal of Engineering Tribology*, 227(2):112–125, 2013.

[26] Alex B Liu, Daniel Mather, and Rolf D Reitz. Modeling the effects of drop drag and breakup on fuel sprays. *SAE Transactions*, pages 83–95, 1993.

[27] Mahle MPULSE magazine. Piston cooling needs. https://www.mpulse.mahle.com/en/do-and-get/8064.jsp.

[28] C Motzkus, E Géhin, and F Gensdarmes. Study of airborne particles produced by normal impact of millimetric droplets onto a liquid film. *Experiments in Fluids*, 45(5):797, 2008.

[29] C Motzkus, F Gensdarmes, and E Géhin. Study of the coalescence/splash threshold of droplet impact on liquid films and its relevance in assessing airborne particle release. *Journal of Colloid and Interface science*, 362(2):540–552, 2011.

[30] I Mudawar and WS Valentine. Determination of the local quench curve for spray-cooled metallic surfaces. *Journal of Heat Treating*, 7(2):107–121, 1989.

[31] Stephen B Pope. *Turbulent flows*. Cambridge University Press, 2001.

[32] L. PRANDTL. Ueber flussigkeitsbewegung bei sehr kleiner reibung. *Verhandl. , Heidelberg, Leipzig*, III, 1904.

[33] Constantine D Rakopoulos and Evangelos G Giakoumis. *Diesel engine transient operation: principles of operation and simulation analysis*. Springer Science & Business Media, 2009.

[34] R Rioboo, C Bauthier, J Conti, M Voue, and J De Coninck. Experimental investigation of splash and crown formation during single drop impact on wetted surfaces. *Experiments in Fluids*, 35(6):648–652, 2003.

[35] Jon R Rybicki and Issam Mudawar. Single-phase and two-phase cooling characteristics of upward-facing and downward-facing sprays. *International Journal of Heat and Mass Transfer*, 49(1-2):5–16, 2006.

[36] P.G.T. Saffman. The lift on a small sphere in a slow shear flow. *Journal of Fluid mechanics*, 22(2):385–400, 1965.

[37] L Schiller. Über die grundlegenden berechnungen bei der schwerkraftaufbereitung. *Z. Vereines Deutscher Inge.*, 77:318–321, 1933.

[38] Hermann Schlichting and Klaus Gersten. *Boundary-layer theory*. Springer, 2016.

[39] PK Senecal, E Pomraning, KJ Richards, and S Som. Grid-convergent spray models for internal combustion engine cfd simulations. In *Internal Combustion Engine Division Fall Technical Conference*, volume 55096, pages 697–710. American Society of Mechanical Engineers, 2012.

[40] Star CCM+ online documentation Siemens. Particle equations of motion. https://documentation.thesteveportal.plm.automation.siemens.com/starccmplus_latest_en/index.html#page/STARCCMP/GUID-1CAF3A65-9203-4AFF-8316-70CBEA981BDB.html#wwID0EDCAFD.

[41] Star CCM+ online documentation Siemens. Segregated flow solver. https://docs.sw.siemens.com/documentation/external/PL20200805113346338/en-US/userManual/userguide/html/index.html?#page/STARCCMP%2FGUID-B9AF428F-9BDF-41EA-9814-AA4487B9992E.html%23.

[42] Star CCM+ online documentation Siemens. Theory of fluid film. https://documentation.thesteveportal.plm.automation.siemens.com/starccmplus_latest_en/index.html#page/STARCCMP/GUID-853860C9-6C1F-4AEF-979F-732B55913167.html.

[43] Star CCM+ online documentation Siemens. Theory of wall impingement. https://documentation.thesteveportal.plm.automation.siemens.com/starccmplus_latest_en/index.html#page/STARCCMP/GUID-F9632039-1AEC-4C90-A5D0-134059196918.html#wwID0E1S2FD.

[44] Star CCM+ online documentation Siemens. Turbulence wall treatment. https://docs.sw.siemens.com/documentation/external/PL20200805113346338/en-US/userManual/userguide/html/index.html#page/STARCCMP%2FGUID-478651F1-9901-41B6-8193-3052E3CCE9DB.html%23.

[45] Star CCM+ online documentation Siemens. Understanding injector types. https://documentation.thesteveportal.plm.automation.siemens.com/starccmplus_latest_en/index.html#page/STARCCMP/GUID-98BBBB36-0E2F-4FBE-879E-C3AF479F01E1.html.

[46] Star CCM+ online documentation Siemens. What does the message: Volume fraction of lagrangian phases limited to 0.75 in x cells of region x mean? *Steve Portal*.

[47] William A. Sirignano. *Fluid dynamics and transport of droplets and sprays*. Cambridge university press, 2010.

[48] M Sommerfeld. Theoretical and experimental modelling of particulate flows. *Lecture series*, 6:3–7, 2000.

[49] John Southard. *Introduction to Fluid Motions, Sediment Transport and Current-Generated Sedimentary Structures*. MIT OpenCourseware, 2006.

[50] George Gabriel Stokes et al. *On the effect of the internal friction of fluids on the motion of pendulums*, volume 9. Pitt Press Cambridge, 1851.

[51] Shankar Subramaniam. Lagrangian–eulerian methods for multiphase flows. *Progress in Energy and Combustion Science*, 39(2-3):215–245, 2013.

[52] Norman Thiel, Hans-Joachim Weimar, Hartmut Kamp, and Herbert Windisch. Advanced piston cooling efficiency: a comparison of different new gallery cooling concepts. *SAE Transactions*, pages 978–992, 2007.

[53] Dr.ir. B.W. van Oudheusden. Lecture notes in viscous flows, 2017.

[54] Vishal Venkatesh. Cfd study of piston cooling using oil jets. Master's thesis, TU Delft, 2019.

[55] LHJ Wachters and NAJ Westerling. The heat transfer from a hot wall to impinging water drops in the spheroidal state. *Chemical Engineering Science*, 21(11):1047–1056, 1966.

[56] Anthony John Wharton and Anthony John Wharton. *Diesel engines*. Butterworth-Heinemann, 1991.

[57] Norbert Wruck. *Transientes Sieden von Tropfen beim Wandaufprall*. Shaker, 1999.

[58] Guan Heng Yeoh and Jiyuan Tu. *Computational techniques for multiphase flows*. Butterworth-Heinemann, 2019.

[59] Lixing Zhou. *Theory and modeling of dispersed multiphase turbulent reacting flows*. Butterworth-Heinemann, 2018.

Appendix A

Properties of engine oil liquid 10-W30

Temperature	Kinematic Viscosity	Density	Dynamic Viscosity	Specific Heat		Thermal Conductivity	Thermal Diffusivity
				per unit mass	per unit volume		
°C	mm^2/s = cSt	kg/m^3	mPa.s = cP	kJ/kg.K	$kJ/m^3.K$	W/m.K	mm^2/s
0	789.8	877.1	692.7	1.81	1584.8	0.1355	0.085
5	547.1	873.7	478.0	1.83	1594.9	0.1351	0.085
10	389.0	870.4	338.6	1.84	1604.4	0.1348	0.084
15	283.2	867.0	245.6	1.86	1614.2	0.1344	0.083
20	210.7	863.7	182.0	1.88	1623.5	0.1340	0.083
25	159.9	860.3	137.6	1.90	1633.1	0.1337	0.082
30	123.6	857.0	105.9	1.92	1642.1	0.1333	0.081
35	97.09	853.6	82.88	1.93	1651.4	0.1329	0.080
40	75.00	850.3	65.85	1.95	1660.3	0.1326	0.080
45	62.65	846.9	53.06	1.97	1669.3	0.1322	0.079
50	51.34	843.6	43.30	1.99	1677.9	0.1318	0.079
55	42.56	840.2	35.76	2.01	1686.7	0.1315	0.078
60	35.67	836.9	29.85	2.03	1695.0	0.1311	0.077
65	30.20	833.5	25.17	2.04	1703.6	0.1307	0.077
70	25.81	830.2	21.43	2.06	1711.7	0.1304	0.076
75	22.24	826.8	18.39	2.08	1720.0	0.1300	0.076
80	19.32	823.5	15.91	2.10	1727.9	0.1296	0.075
85	16.91	820.1	13.87	2.12	1736.0	0.1293	0.074
90	14.90	816.8	12.17	2.13	1743.6	0.1289	0.074
95	13.21	813.4	10.74	2.15	1751.4	0.1285	0.073
100	11.70	810.1	9.542	2.17	1758.8	0.1282	0.073
105	10.56	806.7	8.522	2.19	1766.3	0.1278	0.072
110	9.521	803.4	7.649	2.21	1773.5	0.1274	0.072
115	8.622	800.0	6.898	2.23	1780.8	0.1271	0.071
120	7.843	796.7	6.248	2.24	1787.7	0.1267	0.071
125	7.164	793.3	5.683	2.26	1794.8	0.1263	0.070
130	6.569	790.0	5.189	2.28	1801.4	0.1260	0.070
135	6.046	786.6	4.755	2.30	1808.3	0.1256	0.069
140	5.583	783.3	4.373	2.32	1814.7	0.1252	0.069
145	5.172	779.9	4.034	2.34	1821.3	0.1249	0.069
150	4.806	776.6	3.732	2.35	1827.4	0.1245	0.068

Appendix B

Impingement validation results

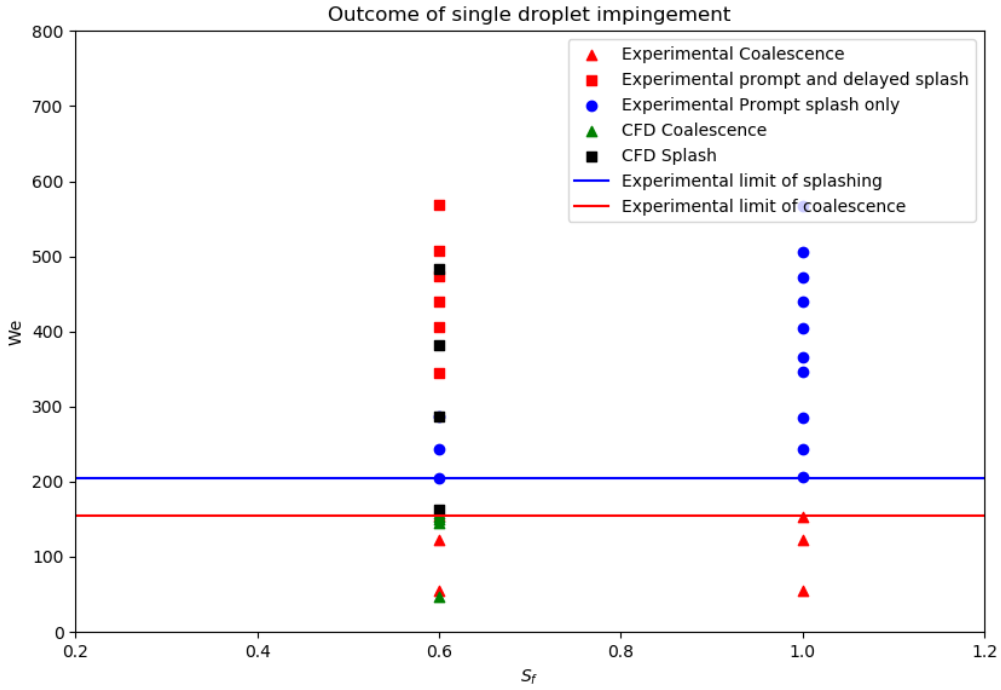

Test #	Velocity [m/s]	We []	Droplet size [mm]	Outcome
1	1.32	50	1.9	Coalescence
2	2.28	150	1.9	Coalescence
3	2.32	155	1.9	Coalescence
4	2.35	160	1.9	Coalescence
5	2.39	165	1.9	Splash
6	2.43	170	1.9	Splash
7	3.22	300	1.9	Splash
8	3.72	400	1.9	Splash
9	4.16	500	1.9	Splash

Table B.1: Matrix of numerical validation results

Appendix C

Heat transfer results

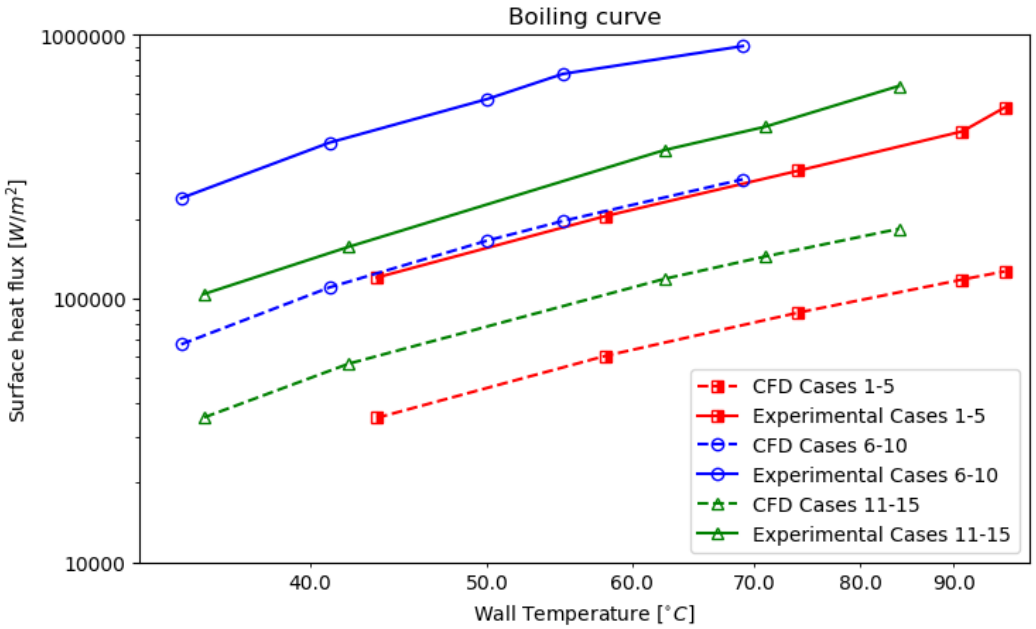

Test #	ΔT_{wd} [°C]	D [mm]	u_d [m/s]	Paper $\dot{Q}_{wp}$ [W/m^2]	CFD $\dot{Q}_{wp}$ [W/m^2]
1	43.5	0.635	18.6	120000	32500
2	58	0.635	18.6	205000	60500
3	74	0.635	18.6	305000	88300
4	91	0.635	18.6	430000	118000
5	96	0.635	18.6	530000	126000

Table C.1: Comparison of experimental and CFD cases 1-5

Test #	ΔT_{wd} [$^{\circ}C$]	D [mm]	u_d [m/s]	Paper $\dot{Q}_{wp}$ [W/m^2]	CFD $\dot{Q}_{wp}$ [W/m^2]
6	34	0.512	18.1	240000	67000
7	41	0.512	18.1	390000	110100
8	50	0.512	18.1	570000	165700
9	55	0.512	18.1	710000	196500
10	69	0.512	18.1	905000	282900

Table C.2: Comparison of experimental and CFD cases 6-10

Test #	ΔT_{wd} [$^{\circ}C$]	D [mm]	u_d [m/s]	Paper $\dot{Q}_{wp}$ [W/m^2]	CFD $\dot{Q}_{wp}$ [W/m^2]
11	35	0.554	26.7	104000	35400
12	42	0.554	26.7	157000	56600
13	62.5	0.554	26.7	365000	118600
14	71	0.554	26.7	448000	144300
15	84	0.554	26.7	639000	183600

Table C.3: Comparison of experimental and CFD cases 11-15